POLITECNICO
MILANO 1863

SCUOLA DI INGEGNERIA INDUSTRIALE
E DELL'INFORMAZIONE

Mathematical and numerical coupled models for aortic hemodynamics and cardiac perfusion

Tesi di Laurea Magistrale in
Mathematical Engineering - Ingegneria Matematica

Author: **Luca Crugnola**

Student ID: 920942
Advisor: Prof. Christian Vergara
Co-advisors: Marco Fedele
Academic Year: 2021-22

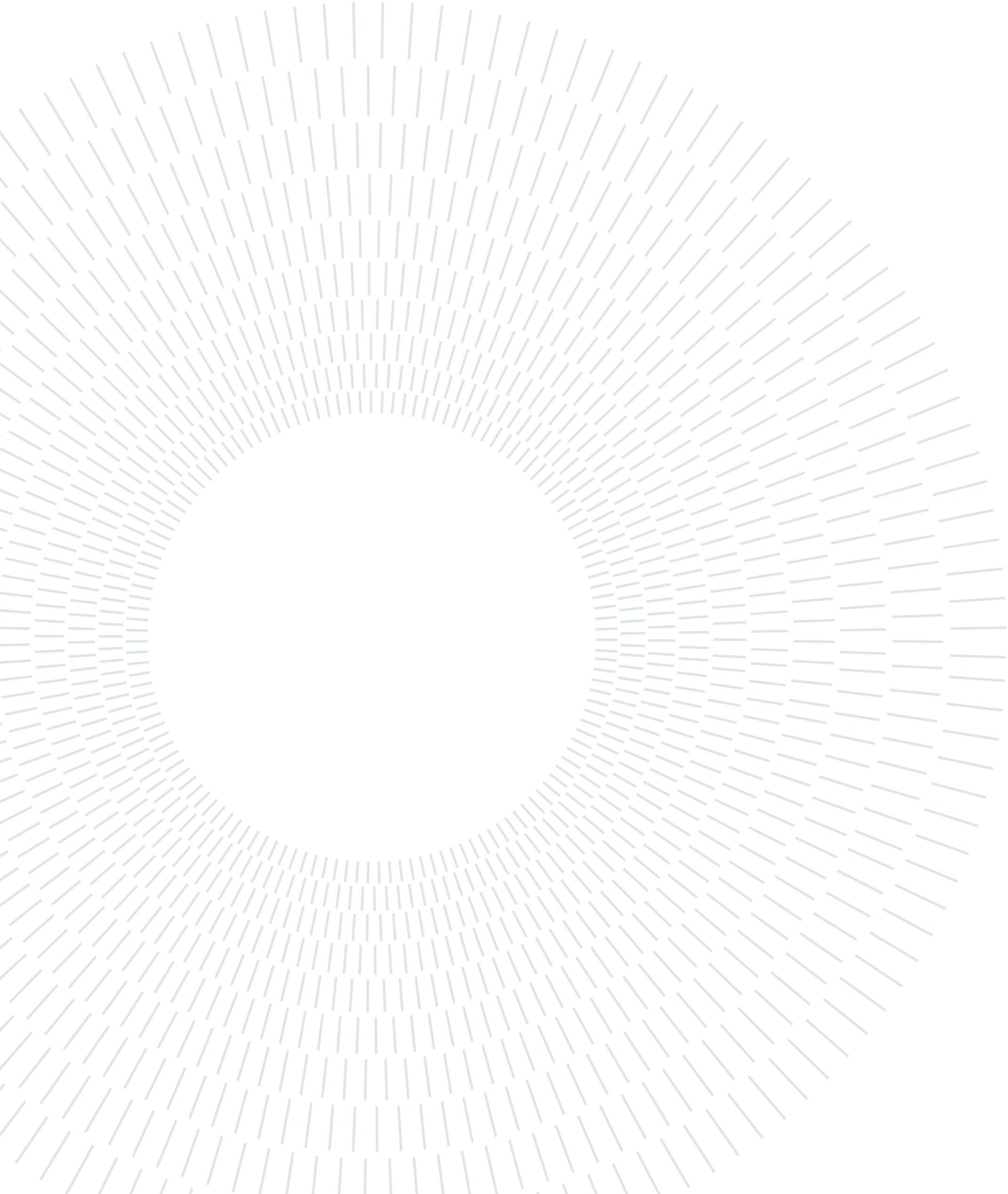

Abstract

Myocardial perfusion is a complex phenomenon which involves several physics related to the cardiac function, such as ventricular ejection, blood dynamics in large vessels and microvasculature, myocardial contraction or electrical signal propagation. Therefore, a mathematical and numerical model able to provide a comprehensive description of this process is yet to be achieved. Indeed, authors mainly focused on the modeling of single physical processes or a coupling of few of them.

The aim of this work is to increase the upstream capabilities of an existing computational model for myocardial perfusion by including the aortic root inside the computational domain where the model is numerically solved. In particular, the new modelling framework provides a complete 3D dimensional description of blood dynamics from the aortic root to the cardiac capillaries, where blood supplies oxygen and nutrients to the heart's tissue, by coupling 3D Navier-Stokes (NS) equations with a multi-compartment Darcy model for the myocardium.

To this purpose, patient-specific anatomical geometries of the aortic root are reconstructed from coronary computed tomography angiography (cCTA) images and computational meshes are generated accounting for the different length scales of the coronary circulation and the level of accuracy needed in the different regions of the domain.

Moreover, a numerical method, based on the Lagrange multipliers, is implemented on the Finite Element library $life^x$ in order to prescribe suitable NS boundary conditions on the artificial boundaries of the aortic root, such as defective flow rate conditions.

Exploiting the newly generated computational meshes and the implemented numerical method, a mathematical and numerical model for hemodynamics inside the aortic root and epicardial coronary arteries is introduced and applied to real geometries, providing physiologically consistent numerical results, both in terms of blood flow and pressure. Thus, validating the reconstruction of anatomical geometries and the modeling approach.

Finally, blood dynamics in large vessels are coupled with a porous media modeling of the myocardium in order to numerically simulate myocardial perfusion. Numerical results are able to describe physiological features of the perfusion process, such as the loss of pulsatility in the microvasculature, retrograde flow and appropriate pressure gradients.

Moreover, after an estimation of the model parameters, based on cCTA images and accounting for stress conditions, the coupled model is able to provide an overall good level of agreement in terms of in-space averaged myocardial blood flow (MBF) with respect to patient-specific clinical data, such as MBF maps. Whereas, for an accurate spatial description of MBF a further optimization of the parameters, exploiting clinical MBF maps, is needed. These results demonstrate that our model is able to accurately estimate MBF maps as long as an appropriate characterization of the myocardium is performed.
The inclusion of the aorta represents a necessary step toward the coupling of the cardiac perfusion process with ventricular dynamics, which involve ventricular ejection and electro-mechanics. Therefore, this work moves in the direction of a more comprehensive computational description of myocardial perfusion.

Keywords: Myocardial perfusion; Aortic root; Multi-physics computational coupled model; cCTA images segmentation; Patient-specific clinical data; Myocardial blood flow (MBF).

Abstract in lingua italiana

La perfusione cardiaca è un fenomeno complesso che coinvolge svariate fisiche associate alla funzione cardiaca, come l'eiezione ventricolare, la dinamica del sangue all'interno di grandi vasi e microvascolatura, la contrazione del miocardio o la propagazione del segnale elettrico. Pertanto, non è ancora stato realizzato un modello matematico e numerico in grado di fornire un descrizione completa di questo processo. Infatti, gli autori si sono principalmente concentrati sulla modellazione di singole fisiche o sull'accoppiamento di alcune di esse.

L'obiettivo di questo lavoro è di estendere un modello computazionale esistente per la perfusione cardiaca includendo l'aorta all'interno del dominio computazionale dove il modello viene risolto numericamente. In particolare, il nuovo approccio modellistico fornisce una descrizione 3D dell'emodinamica dalla radice aortica ai capillari cardiaci, dove il sangue scambia ossigeno e sostanze nutritive con il miocardio, accoppiando le equazioni di Navier-Stokes (NS) con un modello Darcy multi-compartimentale per il miocardio.

A tal scopo, geometrie anatomiche paziente specifiche della radice aortica sono ricostruite a partire da immagini di angiografia coronarica con tomografia computerizzata (cCTA) e mesh computazionali vengono generate tenendo conto delle diverse lunghezze caratteristiche nella circolazione coronarica e del livello di accuratezza necessario nelle diverse regioni del dominio.

Inoltre, un metodo numerico, basato sui moltiplicatori di Lagrange, è implementato all'interno della libreria $life^x$ per prescrivere condizioni al bordo idonee sulle frontiere artificiali della radice aortica, come condizioni di portata deficitarie.

Sfruttando le mesh computazionali appena generate ed il metodo numerico implementato, un modello matematico e numerico per l'emodinamica all'interno della radice aortica e delle arterie coronarie epicardiali viene introdotto e applicato a geometrie reali, fornendo risultati numerici fisiologicamente coerenti, sia in termini di flusso sanguigno che di pressione. Quindi, convalidando la ricostruzione delle geometrie anatomiche e l'approccio modellistico.

Infine, la dinamica del sangue nei grandi vasi è accoppiata con un mezzo poroso che modella il miocardio al fine di simulare numericamente la perfusione cardiaca. I risultati numerici sono in grado di descrivere alcune caratteristiche fisiologiche del processo di perfusione, come la perdita di pulsatilità nel microcircolo, il flusso retrogrado e appropriati gradienti di pressione. Inoltre, dopo una stima dei parametri, basata su immagini cCTA e tenendo conto delle condizioni di stress, il modello accoppiato è in grado di fornire un buon livello di concordanza in termini di flusso sanguigno nel micardio (MBF) medio rispetto a dati clinici paziente-specifici, come mappe MBF. Mentre, per un'accurata descrizione spaziale del flusso sanguigno nel miocardio, è necessaria un'ulteriore ottimizzazione dei parametri, sfruttando le mappe MBF cliniche. Questi risultati dimostrano che il nostro modello è in grado di stimare accuratamente le mappe MBF purché venga eseguita un'adeguata caratterizzazione del miocardio.

L'inclusione dell'aorta rappresenta un primo passo necessario verso l'accoppiamento del processo di perfusione cardiaca con la dinamica ventricolare, che comprende l'eiezione ventricolare e l'elettromeccanica. Pertanto, questo lavoro si muove nella direzione di una descrizione computazionale più completa della perfusione cardiaca.

Parole chiave: Perfusione cardiaca; Radice aortica; Modello multi-fisico computazionale accoppiato; Segmentazione di immaigini cCTA; Dati clinici paziente specifici; Flusso sanguigno nel miocardio.

Contents

Abstract i

Abstract in lingua italiana iii

Contents v

1 Introduction 1
- 1.1 Anatomy and physiology of the heart . . . 1
- 1.2 Myocardial perfusion . . . 5
  - 1.2.1 Coronary Circulation . . . 5
  - 1.2.2 Coronary Blood Flow . . . 6
- 1.3 Modeling the cardiovascular system . . . 7
  - 1.3.1 About blood behavior . . . 8
- 1.4 State of the art on computational methods for myocardial perfusion . . . 9
  - 1.4.1 Complexity reduction approaches . . . 10
  - 1.4.2 3D blood dynamics . . . 11
  - 1.4.3 Porous media modeling . . . 12
  - 1.4.4 Geometric multi-scale coupled models . . . 14
  - 1.4.5 Coupled 3D descriptions of large and small coronary arteries . . . 15
- 1.5 Aims of the thesis . . . 16

2 From clinical image to computational domain 19
- 2.1 State of the art on image segmentation in cardiovascular applications . . . 20
  - 2.1.1 Thresholding . . . 21
  - 2.1.2 Fast Marching . . . 22
  - 2.1.3 Colliding Fronts . . . 23
  - 2.1.4 Level set method . . . 24
- 2.2 Available clinical data . . . 26
- 2.3 Anatomical Geometry reconstruction . . . 27

2.3.1 Available reconstructed geometries 27
2.3.2 Newly reconstructed geometry: aortic root 30
2.4 Building of the complete computational domain 32
2.4.1 Pre-processing on separated structures 32
2.4.2 Connection of the structures 35
2.4.3 Superficial and volumetric mesh for the connected structure 37
2.5 Results 39

3 Computational hemodynamics in aortic root and epicardial coronary arteries 41
3.1 Navier-Stokes equations 42
3.2 Lagrange multipliers method for defective flow rate boundary condition . . 44
3.3 Numerical approximation 46
3.3.1 Temporal discretization and linearization 47
3.3.2 Spatial discretization 48
3.3.3 Algebraic counterpart 49
3.4 Implementation 51
3.5 Numerical results on an idealized geometry 53
3.6 Application to a patient-specific geometry 58
3.6.1 Base scenario: physiological consistency 61
3.6.2 Alternative scenario: different pressure conditions for left and right heart 65
3.7 Final remarks 66

4 Computational multi-physics coupled model for myocardial perfusion 69
4.1 Hemodynamics in the intramural coronary vessels 70
4.1.1 Multi-compartment Darcy model 71
4.1.2 Weak formulation 73
4.1.3 Numerical approximation 73
4.2 Multi-physics coupled mathematical model 75
4.2.1 Coupling conditions 75
4.2.2 Coupled mathematical model 77
4.2.3 Model's parameters estimate 77
4.3 Numerical approximation of the coupled model 79
4.3.1 Temporal discretization and iterative splitting 80
4.3.2 Spatial discretization and algebraic counterpart 81

5 Application of the coupled model to patient-specific cases 85

5.1 Myocardial blood flow maps 86
5.2 Model adjustment in stress conditions 89
5.2.1 Stress *a priori* parameters adjustment 90
5.2.2 Patient-specific parameter optimization 91
5.3 Numerical results in different scenarios 91
5.3.1 Comparison between implicit and explicit splitting strategies 93
5.3.2 Analysis of parameters impacting the pressure fields 97
5.3.3 Cardiac output change: rest vs stress conditions 99
5.4 Consistency test on the numerical results: MBF maps 100
5.4.1 Computation of MBF maps after stress *a priori* parameter adjustment 102
5.4.2 Computation of MBF maps after patient-specific optimization . . . 105
5.5 Final Remarks 108

6 Conclusions **111**

Bibliography **115**

List of Figures **125**

List of Tables **129**

List of Abbreviations **131**

Ringraziamenti **133**

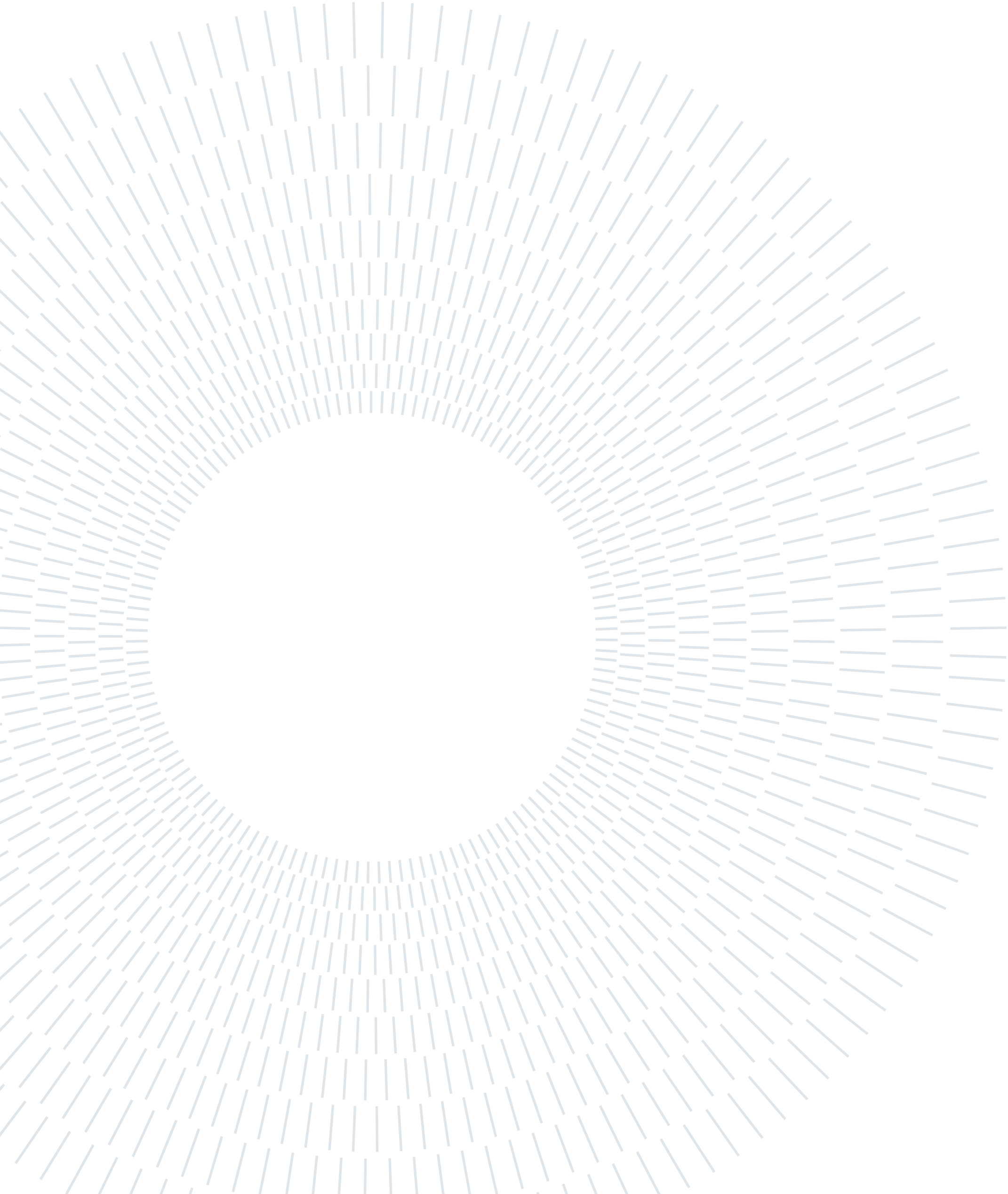

1 | Introduction

Each muscle of the human body needs an oxygen supply in order to function properly and the cardiac muscle, or *myocardium*, makes no exception. The oxygenated blood travels throughout the cardiovascular system and exchanges oxygen with the tissues when it reaches the microvasculature. In the heart's case, the blood flow reaching the muscular tissue is called *myocardial perfusion* and is provided by a very specialized vascular structure, the *coronary circulation*. An obstruction in a coronary vessel can lead to the development of an ischemic tissue downstream the occlusion, which can become necrotic, if not treated, reducing the efficiency of the heart functionalities.

Myocardial perfusion is a complex phenomenon, involving different physical processes related to the cardiac function, which makes it difficult to analyze it in all its features. In recent years computational models are more and more involved in the study of the cardiac perfusion both in physiological and pathological conditions, representing a non-invasive, practical and flexible approach to tackle the complexities of this process.

In this chapter we provide an overview of the anatomy and physiology of the heart (Sect. 1.1). Then, in Section 1.2 the myocardial perfusion is detailed, along with the coronary circulation (Sect. 1.2.1) and the coronary blood flow (Sect. 1.2.2). The modeling of the cardiovascular system is described in Section 1.3, with a particular focus on blood dynamics 1.3.1. In Section 1.4 we present the state of the art on myocardial perfusion modeling. Finally, the aims of the thesis are discussed in Section 1.5.

1.1. Anatomy and physiology of the heart

The cardiovascular system is a closed system that carries oxygenated blood to all the tissues of the human body. It is composed by three compartments:

- the heart;
- the systemic and pulmonary circulation;
- the microvasculature.

In this work we are particularly interested in the heart and its functionalities.

Located between the lungs in the middle of the chest and encased within a membranous fibroserous sac, called *pericardium*, the heart is a muscular organ which pumps oxygenated blood throughout the cardiovascular system . It is made of three layers:

- *epicardium*: thin outer layer of connective tissue;
- *myocardium*: thick muscle layer that enables heart contraction, made of *cardiomyocytes*;
- *endocardium*: thin inner layer of endothelial cells and connective tissue.

The heart can be divided in two sides, left and right, both working as a pump. The right heart takes deoxygenated blood from the systemic veins and pumps it into the pulmonary circulation, while the left heart takes oxygenated blood from the pulmonary veins and pumps it into the systemic circulation. In each side of the heart there are an atrium and a ventricle, blood can travel from the atria to the ventricles through atrio-ventricular (A-V) valves, which allow the blood to flow only in one direction. The *left atrium* and *left ventricle* are connected by the *mitral valve*, whereas the *tricuspid valve* connects the *right atrium* and the *right ventricle.* There are also semilunar valves that ensure one way blood flow from the ventricles to the corresponding circulation: the valves regulating blood ejection from the *left ventricle* to the *aorta* and from the *right ventricle* to the *pulmonary artery* are called *aortic valve* and *pulmonary valve*, respectively. Finally, the left and right sides of the heart are separated by *interatrial* and *interventricular septa* which avoid the mixture of oxygenated and deoxygenated blood. A representation of the whole heart is given in Figure 1.1.

The main driver of the cardiac function is the contraction of the cardiac muscle (*myocardium*), that happens due to the excitability of its cells, the *cardiomyocytes.* Indeed, these cells are able to produce a variation in membrane voltage when suitably stimulated. The electric signal starts from the heart natural pacemaker, the *sinoatrial node*, which consists of autorhythmic cells located in the superior posterolateral wall of right atrium. Then it propagates rapidly from cell to cell throughout the whole atria. The wave front will eventually reach the *atrioventricular node*, that slows down the transmission of the signal to allow the atria to complete their contraction and to empty their blood into the ventricles before ventricular contraction begins.

Let us now briefly present the cardiac cycle, which consists of alternate periods of cardiac muscle contraction and relaxation, the *systole* and the *diastole*, respectively. For its description, we consider the left heart and we start from the situation when the left

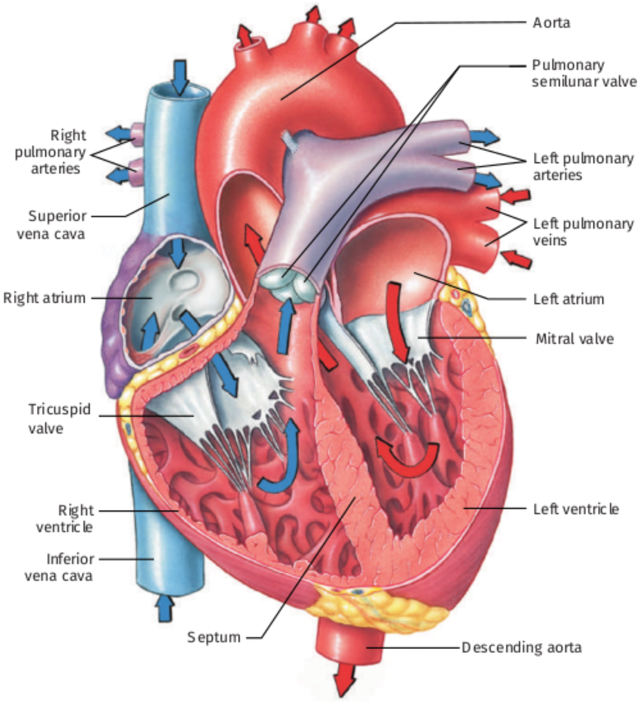

Figure 1.1: Representation of the human heart [1].

atrium is filled with oxygenated blood coming from the pulmonary veins, the mitral valve is closed and the left ventricle has reached the maximum contraction. An analogous description can be provided for the right heart, just accounting for different values of the pressures. The cardiac cycle comprises four phases:

- *Ventricular filling.* As soon as the pressure in the atrium exceeds the ventricular pressure ($\sim 10\ mmHg$) due to the continuous blood inflation, the mitral valve opens. So that, blood starts filling the ventricle, while it relaxes. We have a first passive sub-phase characterized by a fast inflation of blood in the ventricle caused by the pressure gradient between atrium and ventricle (phase 1a in Fig. 1.2). Then, the atrium actively contracts producing a slow ventricular inflation of the remaining blood (phase 1b in Fig. 1.2).

- *Isovolumic contraction.* After the contraction of the atrium, *atrial systole*, the ventricular active contraction starts. This produces an increase in ventricular pressure causing retrograde flow that accordingly closes the mitral valve. The ventricle is now contracting while both the mitral and aortic valves are closed, therefore there is a continuous and fast increase in ventricular pressure without any change of blood volume thanks to blood incompressibility (phase 2 in Fig. 1.2).

- *Ventricular ejection.* Due to the fast increase during the previous phase, the ventricular pressure will eventually exceed the aortic one ($\sim 70\ mmHg$) causing the aortic valve to open and allowing the oxygenated blood to be expelled into the aorta, reaching the systemic circulation. At a first stage the ventricular contraction carries on, so that the ventricular pressure continues to increase. Accordingly, also the aortic pressure increases, maintaining a pressure gradient between ventricle and aorta which accelerates the blood (phase 3a in Fig. 1.2). As soon as the active contraction of the ventricle stops this pressure difference start decreasing and after a short period it becomes zero, allowing the flow rate to reach its maximum value (phase 3b in Fig. 1.2). Then, the pressure in the aorta becomes higher than in the ventricle, provoking a deceleration of blood coming into the aorta. When, due to this deceleration, the flow rate becomes negative the aortic valve closes and blood ejection stops (phase 3c in Fig. 1.2).

- *Isovolumic relaxation.* Both the mitral and the aortic valves are now closed and the ventricle is releasing its energy. This causes a fast decrease in ventricular pressure, since no change in volume is possible. So that ventricular pressure becomes smaller then the atrial one and the cycle starts again (phase 4 in Fig. 1.2).

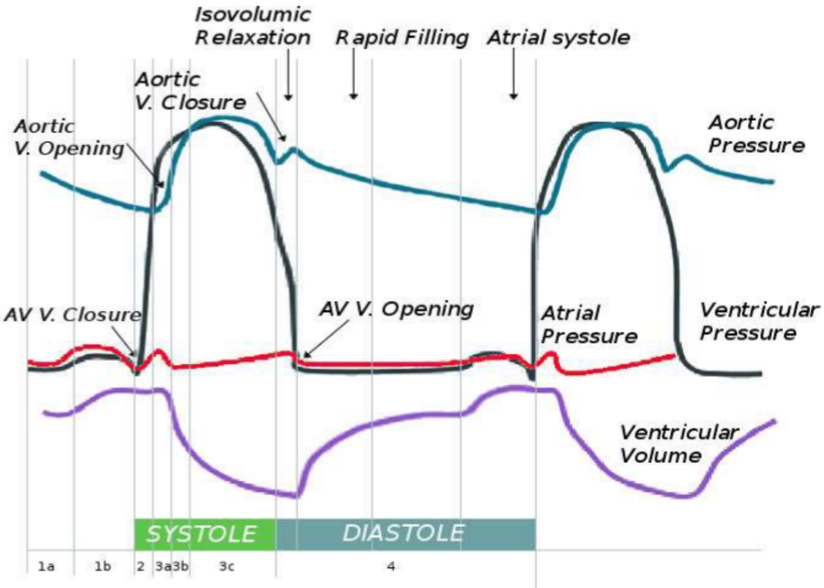

Figure 1.2: Aortic pressure, ventricular pressure, atrial pressure and ventricular volume during the cardiac cycle [2].

1.2. Myocardial perfusion

Being the engine of the human body, an impairment of the work of the heart can compromise the correct functioning of all its organs. The cardiac muscle needs a continuous oxygen and nutrients supply in order to enable a harmonious coordination of all the physical processes involved in the cardiac cycle. In particular, the per gram oxygen consumption of the heart is $\sim 50 \div 100 \ \mu L_{O_2}/min/g$ of tissue (highest among skeletal muscles), receiving about 5% of the cardiac output in rest conditions [3–5]. The blood supply to the cardiac muscle, called *myocardial perfusion*, or *myocardial blood flow* (MBF), is provided by a specialized vascular structure, the *coronary circulation.*

1.2.1. Coronary Circulation

The coronary circulation originates from the *coronary ostia* in the sinuses of Valsalva, just above the aortic valve, with two main vessels: the *right coronary artery* (RCA) and the *left main coronary artery* (LCA) [6, 7] (Fig. 1.3a).

Such main vessels give rise to several smaller branches that will eventually enter inside the cardiac tissue. So that, part of the oxygenated blood expelled from left ventricle into the aorta through the aortic valve is re-directed to the cardiac muscle, where it will exchange oxygen with the tissue when it reaches the capillaries. The blood coming from capillaries is drained by the coronary venous system into the *coronary sinus*, from where it will return to the right atrium.

The morphology of the coronary arterial tree has a well-defined outside-in structure [5], as shown in Figure 1.3b. There is a clear separation of scale between the main large arteries ($\sim 1 \div 5 \ mm$) laying on the epicardium and the smaller arterioles ($\sim 100 \div 300 \ \mu m$) and capillaries ($\sim 5 \div 10 \ \mu m$) penetrating into the muscle. The former will be referred to as *epicardial coronary arteries* and the latter as *intramural vessel*, according to the subdivision proposed in [8].

Distinct coronary arteries supply different myocardial territories, as suggested by experimental evidence from high resolution cryomicrotome imaging [10]. A microscope analysis showing capillary end loops in border zone of such regions provides an additional proof of this division [11]. Such distinct myocardial territories supplied by different coronary arteries are called *perfusion regions.*

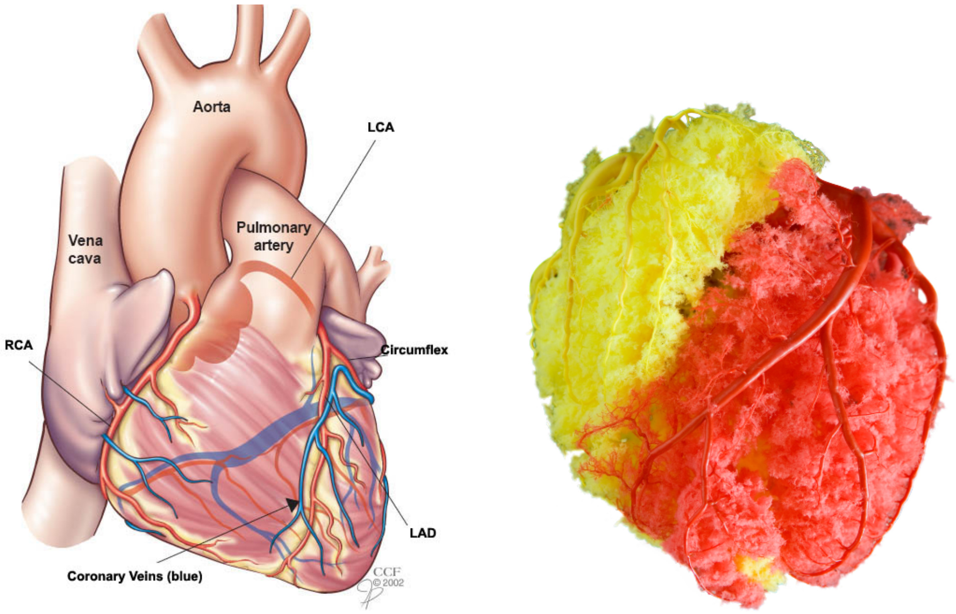

(a) (b)

Figure 1.3: (a) Anatomy of the main coronary arteries and veins. *Source Cleveland Clinic* [9]. (b) Entire coronary artery tree. *Source Wikipedia*.

1.2.2. Coronary Blood Flow

Let us now describe the *coronary blood flow* (CBF). Due to the particular morphology of the coronary artery tree, CBF does not only depend on the gradient between aortic and venous pressure, unlike for the rest of the systemic circulation. Indeed, during systole the intramural vessels of the coronary circulation shrink due to the contraction of the muscle, generating an higher resistance for the blood flow. So that CBF is said to be a diastolic flow since it reaches its peak during early diastole (Fig. 1.4).

The right heart works with lower pressure with respect to the left heart, therefore the contraction has a smaller impact on the downstream vessels and the resulting CBF in RCA is only partially influenced by systole. On the other hand, in early systole the CBF in LCA can reach negative values due to the compressed intramural vessels and low aortic pressure. The flow then increases and reaches its maximum during early diastole when intramural vessels are no longer compressed. So that, around the 80% of the left CBF occurs during diastole. Moreover, the compression of the intramural vessels pushes the venous blood from the endocardial layer to the epicardial one, therefore the flow in coronary veins reaches the peak during systole, unlike in coronary arteries. The pulsatile behavior of the flow inside the coronary arteries is smoothed along the circulation, so that inside the capillaries the blood flow is almost constant during an heart beat.

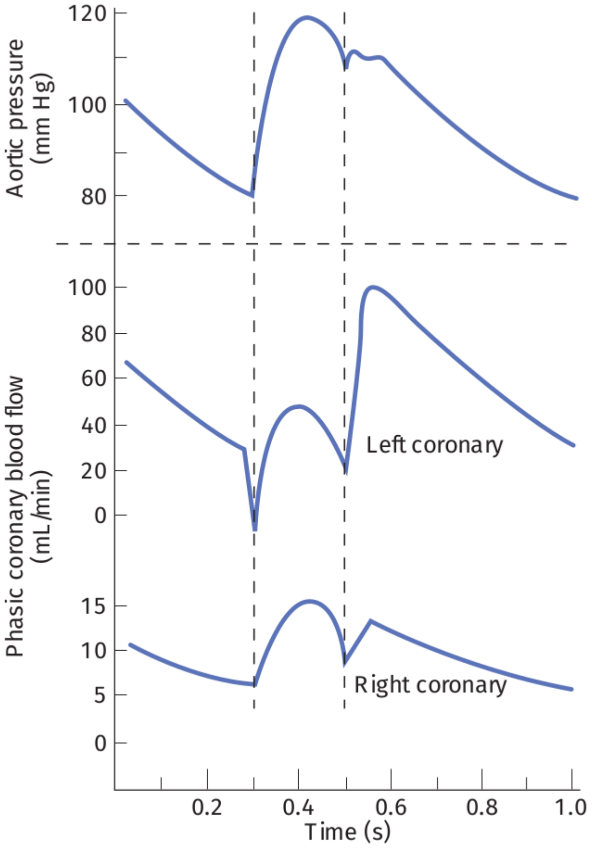

Figure 1.4: Aortic pressure and CBF for LCA and RCA [12].

1.3. Modeling the cardiovascular system

Mathematical models can be used to describe in terms of algebraic, integral or differential equations most of the quantitative processes happening in several fields, such as physics, biology, chemistry, etc. In order to formulate a mathematical model one has to perform a detailed analysis of the process under study, defining the variables of the problem and making assumptions to capture only the most relevant features. In some cases the existence of analytical solutions for these equations is yet to be proven and in general they can be difficult to find. Therefore, approximated solutions are computed using a numerical method, providing quantitative information on the phenomenon under study. Numerical methods are nowadays widely involved in the analysis of several phenomena thanks to the continuous technological development [13].

Computational models represent a non-invasive, practical and flexible approach to study complex phenomena. Indeed, they can provide quantitative information on features that are difficult to capture using experimental or theoretical methods due to economical or physical reasons. Moreover, different scenarios of a system can be analyzed just accounting for a change in the parameters of the model.

For this reasons, computational approaches are becoming more and more popular also in cardiovascular applications. Currently they are mostly used for the study of the physiological system, but they can also represent a practical support for clinicians. Indeed, a model can be personalized using clinical data in order to study a phenomenon in a patient-specific framework. So that, in the future, they may be used in clinical practice for diagnosis, risk stratification, therapy optimization and decision-making support.

In order to perform patient-specific numerical simulations one needs a set of clinical data. The following subdivision can be made:

- **Geometrical data**: clinical images used to reconstruct, through an image segmentation technique, the geometry of the vascular district of interest. A computational mesh has to be then generated on such reconstructed geometry in order to create the computational domain where the model is numerically solved.
- **Boundary data**: a set of conditions to be prescribed on the physical (e.g. vessel's wall) or artificial (e.g. vessel's cross-section) boundaries of the computational domain. They can be derived from physics (e.g. no slip condition on vessel's wall) or from patient-specific measurements (e.g. flow rate through a cross-section).
- **Biological data**: physical parameters of the differential equations constituting the mathematical model. They can be known (e.g. blood viscosity in large vessels) or they have to be estimated.

Computational models have been applied in cardiovascular applications in order to study many phenomena, such as blood dynamics in carotids [14] and in abdominal aortic aneurysms [15, 16], or even the cardiac function [17, 18]. Numerical approaches have been introduced also in the case of myocardial perfusion in order to predict MBF inside the myocardium [19–22].

In this work we are particularly interested in blood dynamics numerical simulations.

1.3.1. About blood behavior

Choosing the governing equations for blood dynamics in cardiovascular applications is very challenging, due to the presence of different spatial scales and the rheological properties of blood. Blood is a dense suspension of cells in a watery solution, the most abundant cellular type are the erythrocytes, whose mean diameter is $\sim 8\ \mu m$.

Therefore, a common strategy to model blood dynamics inside large arteries (at least $\sim$

1 mm) is through the Navier-Stokes (NS) equations, which hold under the assumption of an incompressible Newtonian fluid. Indeed, blood can be assumed to be homogeneous inside such vessels, due to the dimension of its cells [23]. This assumption does not hold inside the capillaries, since their diameter is similar to the diameter of the blood cells [24].

Moreover, it is usually unfeasible to provide an explicit description of the microvasculature, due to the dense network of vessels composing it. For these reasons, authors usually opt for a porous media modeling of the microvasculature, which involves an homogenization of the vasculature district under study.

Qin et al. [25] performed numerical hemodynamics simulations in patient-specific abdominal aorta with aneurysm using the NS equations. While Pillalamarri et al. [26] used them to study blood dynamics inside pulmonary hypertension. In the coronary context, Sankaran et al. [27] leveraged NS equations to analyze the influence of coronary artery bypass graft surgery on hemodynamics.

On the other hand, a porous media modeling approach was applied by Coccarelli et al. [28] in order to describe the flow resistance offered by microcirculation. Moreover, a homogenization of the microvascultaure was perform by Kremheller et al. [29] in order to propose a new approach to describe vascular tumor growth.

1.4. State of the art on computational methods for myocardial perfusion

During the last twenty years computational methods have played an important role in studying the cardiovascular system to investigate physiological and pathological phenomena. Nevertheless, due to the complexity of the myocardial perfusion, a complete and robust model for a comprehensive quantification of this process is yet to be achieved. Indeed, as we highlighted in Section 1.2, the coronary circulation presents a complex morphology and its blood flow depends on different physics related to the cardiac function, which makes it difficult to propose a model able to describe the cardiac perfusion process in all its features.

In this section we give an overview of the modelling approaches followed by various authors for the description of coronary blood flow and myocardial perfusion. Due to the heterogeneous length scales of the coronary circulation different models have been applied for blood dynamics inside the large epicardial coronary arteries and the small intramural vessels, according to the issues explained in Section 1.3.1. First, we give an overview on the strategies that have been used to reduce the complexity of the description. Then, three dimensional models for blood dynamics in large epicardial coronary arteries and intramural vessels are discussed. Finally, we present some geometrical multi-scale approaches and a 3D mathematical model, which couple two or more of the previous models.

1.4.1. Complexity reduction approaches

A complete three-dimensional description of the coronary artery network is not necessary to obtain meaningful quantitative information in some applications. In these cases authors have used models, based on simplifying assumptions, to investigate only the most relevant features of blood dynamics, while significantly decreasing the computational cost.

Let us briefly present here some of the modeling approaches followed in order to reduce the complexity of the description of blood dynamics inside the coronary circulation:

- **Poiseuille's law**: it describes the stationary pressure drop in a rigid cylindrical conduct for an incompressible Newtonian fluid due to the fluid's viscosity. The coronary arterial network can be represented as a series of cylindrical vessels, using the Poiseuille's law to model fluid dynamics inside each vessel. In literature, this approach was enforced to study the impact of the morphological features of the coronary tree (e.g. anatomy, branching pattern) on the distribution of blood flow across the network [30–32]. However, this strategy fails in providing a temporal description of CBF, thus more detailed models are needed for a comprehensive description of CBF.

- **Lumped parameter models**: they model the behavior of a spatially distributed physical system by concentrating its most relevant features in a single element. In particular, the partial differential equations (PDE's) regulating the original model become a set of ordinary differential equations (ODE's), greatly reducing the computational cost of solving the problem. In the study of coronary blood flow and myocardial perfusion, lumped parameter models have been used to describe the entire coronary arterial tree [33–38], mainly providing boundary conditions which account for the peripheral branches downstream a truncated coronary artery. Moreover, such models have been applied to represent single vessel tracts, which are coupled to model the whole vessels network [39–43]. In the latter case, distinct lumped parameter models are used to represent different segments of the vascular network. Due to their concentrated nature such models are not suited to describe the flow rate or pressure wave distribution across the coronary network or the spatial distribution of blood flow inside the myocardium.

- **1D blood dynamics**: a one dimensional description of blood dynamics in a com-

> pliant vessel can be derived from the momentum and mass conservation equations of a 3D Navier-Stokes problem by averaging in space over the vessel cross-section under suitable assumptions. The resulting system presents two PDE's in three unknowns (flow rate, mean pressure and area of the vessel cross-section). Therefore, an additional equation has to be introduced in order to close the system: a common choice is to use a *vessel law*, which is a pressure-area relation derived from finite elasticity. 1D models are the most used for the description of blood dynamics in coronary arterial networks [44–50]. Indeed, they allow the description of wave propagation in a spatially distributed domain, unlike lumped parameter models or Poiseuille's law, while maintaining a low computational cost with respect to a three dimensional description. It is important to note that 1D models, which provide a cheap and detailed analysis in physiological cases, can be too limited when studying pathological cases. Indeed, they do not allow the computation of wall shear stress (WSS), which is a key parameter to predict the possible formation of atherosclerotic plaques, and they can simulate only empirically the viscous losses due to a stenosis.

All the presented approaches have some limitations related to their simplified assumptions. Therefore, for a comprehensive description of blood dynamics in the coronary circulation, particularly in pathological cases, complete 3D approaches should be taken into consideration.

1.4.2. 3D blood dynamics

A complete three dimensional description of blood dynamics is usually performed using the 3D formulation of the Navier-Stokes equations. This approach is much more expensive with respect to the simplified models just presented, so that it is usually enforced if one is interested in an analysis of the coronary circulation considering both physiological and pathological cases. Indeed, this model allows for a description of regional WSS, recirculation zones and secondary flows, which have a non negligible impact on blood dynamics in pathological cases, such as presence of stenosis.

A three dimensional modeling of the whole coronary arterial tree would be unfeasible, due to the high computational cost of solving the Navier-Stokes equations. For this reason, only the main epicardial arteries or parts of their branches are usually modelled following this strategy. This approach has been enforced in different applications, such as to study the effect of a stenosis on the blood flow [35, 51], to numerically compute wall shear stresses [52, 53], to study a coronary artery aneurysms caused by Kawasaki disease [54], to investigate the impact of coronary stents on blood dynamics [55] or to analyze stented coronary bifurcations [56].

Let us highlight that 3D strategies in the CBF context have been mostly applied to study coronary blood dynamics inside the epicardial branches without considering the myocardial perfusion process.

1.4.3. Porous media modeling

A porous medium modeling approach is usually applied to describe the intramural vessels of the coronary circulation. It is based on a homogenization of the myocardium, in which the vasculature is represented as a network of interconnected pores that branches out inside a solid material (cardiac tissue). A porous medium consists of two phases: void and solid. The fraction between the volume of the void phase and the total volume defines the global porosity of the porous medium, analogously also a local porosity can be defined in the different regions of the medium.

This modeling strategy is enforced due to the high computational cost and complexity of modeling explicitly blood dynamics inside the intramural vessels (see Sect. 1.3.1). Moreover, clinical data do not provide a visualization of the intramural network that consequently cannot be reconstructed for a specific patient.

In the context of cardiac applications, Darcy's law is often used to model fluid dynamics in a porous medium. Darcy's law is a physical law holding under the hypothesis of a laminar flow, which makes sense inside the intramural network due to the small dimension of the vessels and the low velocity of blood. In particular, Darcy's law describes the direct proportionality between flow rate and pressure gradient in a fully saturated porous medium, using a proportionality coefficient which depends on the permeability of the porous medium and the dynamic viscosity of the fluid.

Multi-compartment Darcy problem

The characteristic dimension of the vessels changes significantly inside the intramural network (small arteries, arterioles and capillaries). For this reason, Huyghe et al. [57] proposed a hierarchical subdivision of the intramural vessels into different vascular compartments (levels), each of them related to a characteristic length scale. The vascular compartments are then modelled as different porous media coexisting inside the same domain, the myocardium. So that, the resulting physical properties of each porous medium (porosity, permeability) depend only on the corresponding vascular compartment (Fig. 1.5). Different vascular compartments are coupled by means of inter-compartment flows, depending on inter-compartment pressure gradients through some coupling coefficients.

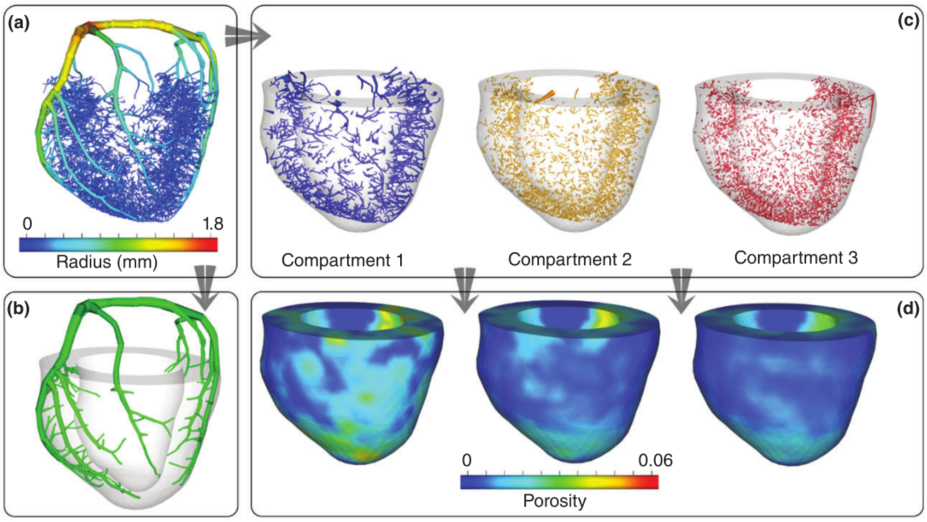

Figure 1.5: Schematic overview of a three-compartment vascular subdivision in a left ventricle: a) porcine left coronary artery network from cryomicrotome images; the network is subdivided in epicardial coronary arteries (b) and intramural vessels, which are partitioned in three groups (c); each group will characterize a different compartment with spatially varying porous media parameters (d). [58]

A single compartment approach for the intramural network would lead to the computation of pressures and flow rates which are not representative of a specific vascular level, thus providing only average information. On the other hand, we are particularly interested in having a quantification of the blood flow inside the capillaries, where blood exchanges oxygen with the cardiac tissue. Therefore a multi-compartment formulation is to be preferred.

The primal and mixed formulations of the multi-compartment Darcy model have been compared from a computational point of view by Michler et al. [59]. They concluded that in clinical application the former is best suited thanks to the significant savings in terms of memory and computational power. Moreover, Cookson et al. [60] coupled a multi-compartment approach with porous mechanics in order to study the interaction between coronary perfusion and myocardial contraction.

The multi-compartment Darcy model depends on a set of physical parameters that have to be estimated, such as the permeability of each vascular compartment and the inter-compartment coupling coefficients. A proper estimation of such parameters is a crucial step to obtain meaningful perfusion results.

A first analysis of the parametrization of the model has been carried out by Vankan et al. [61] by comparing the solution of the multi-compartment Darcy model with the solution obtained applying the Poiseuille's law inside the vascular network. Hyde et al. [62] performed a further analysis, applying the multi-compartment Darcy model to a porcine intramural coronary network. In their study the performances of the multi-compartment model have been analyzed for different choices of the permeability tensor: a porosity scaled isotropic tensor and a 4D estimation of the permeability tensor (proposed by Huyghe et al. [63]). They concluded that the isotropic tensor provides better results in terms of the mismatch with the explicit Poiseuille. Moreover, in the same study they proved that a better agreement can be achieved by using three compartments instead of two and estimating the inter-compartment coupling coefficients relying on anatomical and fluid dynamics features of the vascular network.

1.4.4. Geometric multi-scale coupled models

The myocardial perfusion process involves several physical phenomena which are characterized by different length scales. In this section we have shown that different dimensional models can be applied for the simulation of such phenomena. These models can also be coupled together in order to provide a more comprehensive description of the cardiac perfusion process while maintaining a low computational cost, giving rise to multi-scale models. Multi-scale models can be used to extract only the most relevant features of a phenomenon involved in the myocardial perfusion, while providing a more detailed description of other physics.

Multi-scale models represent a very flexible and cheap approach to model myocardial perfusion, but they are very challenging both from a mathematical and numerical point of view. Indeed, in order to couple different dimensional models one has to formulate proper assumptions, prescribe meaningful boundary conditions and perform a well-posedness analysis. Moreover, ad hoc numerical methods have to be introduced for their solution.

Let us report here some of the multi-scale approaches that have been enforced in the myocardial perfusion modeling:

- 1D blood dynamics for large coronary arteries - 3D porous medium model for the intramural vessels [19, 48, 60, 62, 64].
- 1D blood dynamics for large coronary arteries - 0D approach for the intramural vessels [44, 47, 65, 66].
- 3D blood dynamics for epicardial coronary arteries - 0D approach for the intramural

vessels [35, 67, 68].

- 0D model for the coronary artery network - 3D mechanical contraction model in the left ventricle [22].

Papamanolis et al. [64] applied a multi-scale model in a patient-specific framework in order to study myocardial perfusion both in physiological and pathological cases. Their aim was to propose a patient-specific multi-scale model enabling blood flow simulation from large coronary arteries to myocardial tissue. The blood flow inside the large arteries was modelled following a 1D approach, while a single compartment porous media model was used to describe the myocardium. Patient-specific aortic roots and epicardial coronary arteries were reconstructed from coronary computed tomography angiography data until the limit imposed by the spatial resolution of the images. The vascular network was then extended from the image-based model down to the arteriole level using a space-filling forest of synthetic trees. They applied the model to 6 patients: 5 patients presenting non-obstructive coronary artery disease (CAD) and 1 patient with obstructive CAD. The simulated results compare well to clinical data in case of non-obstructive disease, while for the severe obstruction case, results link coronary artery narrowing with impaired myocardial blood flow, demonstrating that the model is able to predict myocardial regions showing perfusion deficits. This represents one of the first cases in which a computational model for blood flow simulation from epicardial arteries to myocardial tissue has been applied and validated on human data.

1.4.5. Coupled 3D descriptions of large and small coronary arteries

Recently, Di Gregorio et al [69] proposed a mathematical and numerical model for cardiac perfusion, accounting for the different length scales of the vessels in the coronary tree. Analogously to what has been done by Papamanolis et al [64], they aimed at simulating blood flow from epicardial coronary arteries to the myocardial tissue, but in this case they opted for a complete 3D description of fluid dynamics inside large arteries and a multi-compartment porous media modeling of the left ventricle. The 3D Navier-Stokes equations are couple with the multi-compartment Darcy formulation by means of suitable boundary conditions regulating the interaction between the two physical processes. Such model has been then applied to a patient-specific framework [70] in order to predict myocardial blood flow under stress conditions for 9 patients: 4 healthy patients and 5 patients presenting functionally significant coronary artery stenosis. The validation of the model has been carried out by comparing the simulated results with the distribution of MBF inside the left ventricle obtained by clinical data. Different strategies for the estimation of the model parameters are investigated, such as *a priori* estimation (only relying on data obtained from non-invasive techniques) and patient-specific estimation (correcting parameter values using the clinical measurement of MBF). They found that, after a patient-specific parameter estimation, the simulated results provide an excellence agreement with the clinical data, therefore validating the model.

To the best of our knowledge, this is the first time in literature that a 3D computational model for the simulation of cardiac perfusion has been calibrated with geometrical and functional patient-specific data. In figure 1.6 we report, in terms of MBF maps, the results obtained in [70] for the 9 patients using the model proposed in [69].

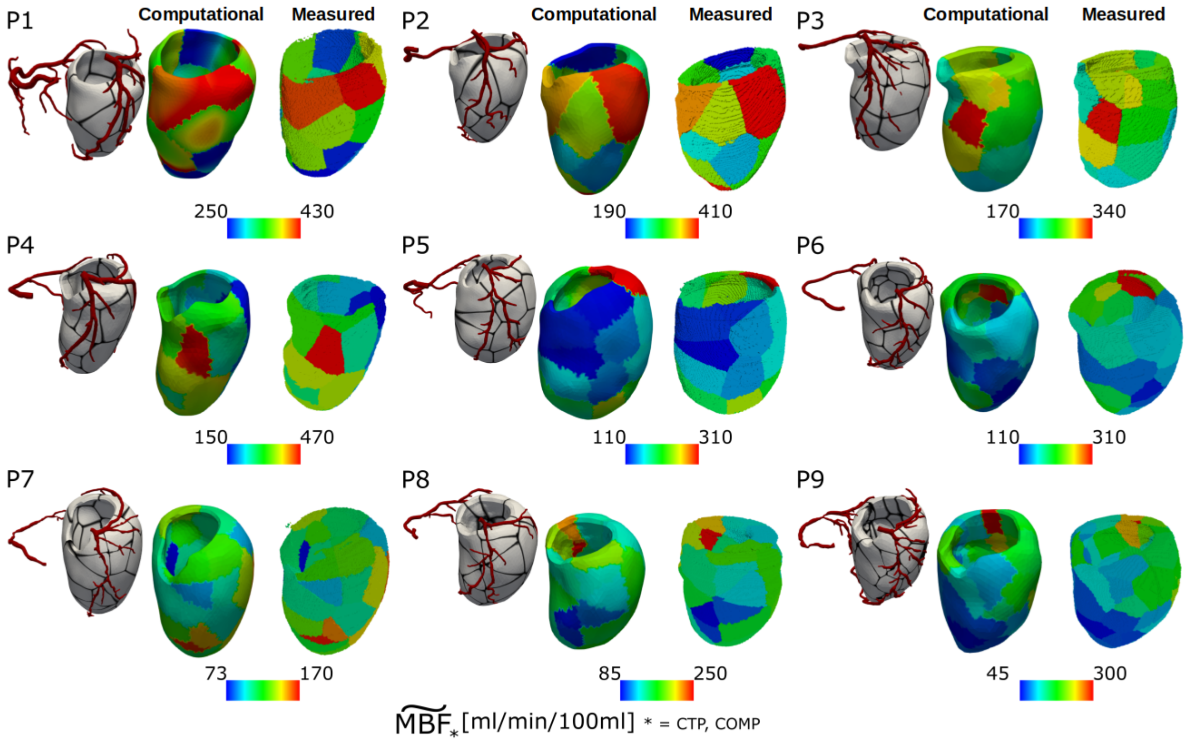

Figure 1.6: For each patient considered in [70] is reported form left to right: the reconstructed epicardial coronary arteries and left ventricle (divided in perfusion regions), the MBF map computed from numerical simulations and the MBF map computed from clinical data. [71]

1.5. Aims of the thesis

This project thesis aims at increasing the upstream capabilities of the computational model proposed by Di Gregorio and colleagues [69] (Section 1.4.5) by including the aortic root inside the computational domain where 3D Navier-Stokes equations are solved. Moreover, this new modeling approach is applied in a geometrically patient-specific framework in order to investigate its performance. To the best of our knowledge, this study represents the first time in literature that a computational model for myocardial perfusion, providing a full 3D description of blood dynamics from the aortic root to the cardiac tissue, is applied to patient-specific geometries and calibrated using clinical data.

To this purpose, the project comprises several steps:

1. reconstruction of patient-specific geometries for the aortic root that have to be connected to the already available reconstructions of the epicardial coronary arteries [70] and generation of a computational mesh on the connected structure;

2. definition of suitable boundary conditions to be prescribed on the aortic inlet and outlet cross-sections and implementation of a numerical method in order to impose them in a simulation;

3. computational fluid dynamics (CFD) simulations inside a patient-specific aortic root and epicardial coronary arteries (thus neglecting the myocardium), with particular focus on the flow partition between left and right coronary arterial branches;

4. coupled problem between CFD in the connected domain (aortic root + epicardial coronaries) and multi-compartment Darcy model for the myocardium;

5. exploit the model reported at point 4. to numerically simulate myocardial perfusion inside patient-specific geometries considering different scenarios in order to understand the impact of the model parameters on the results.

6. investigate the reliability and the accuracy of the computational multi-physics model reported at point 4. in reproducing patient-specific MBF maps starting from cCTA images.

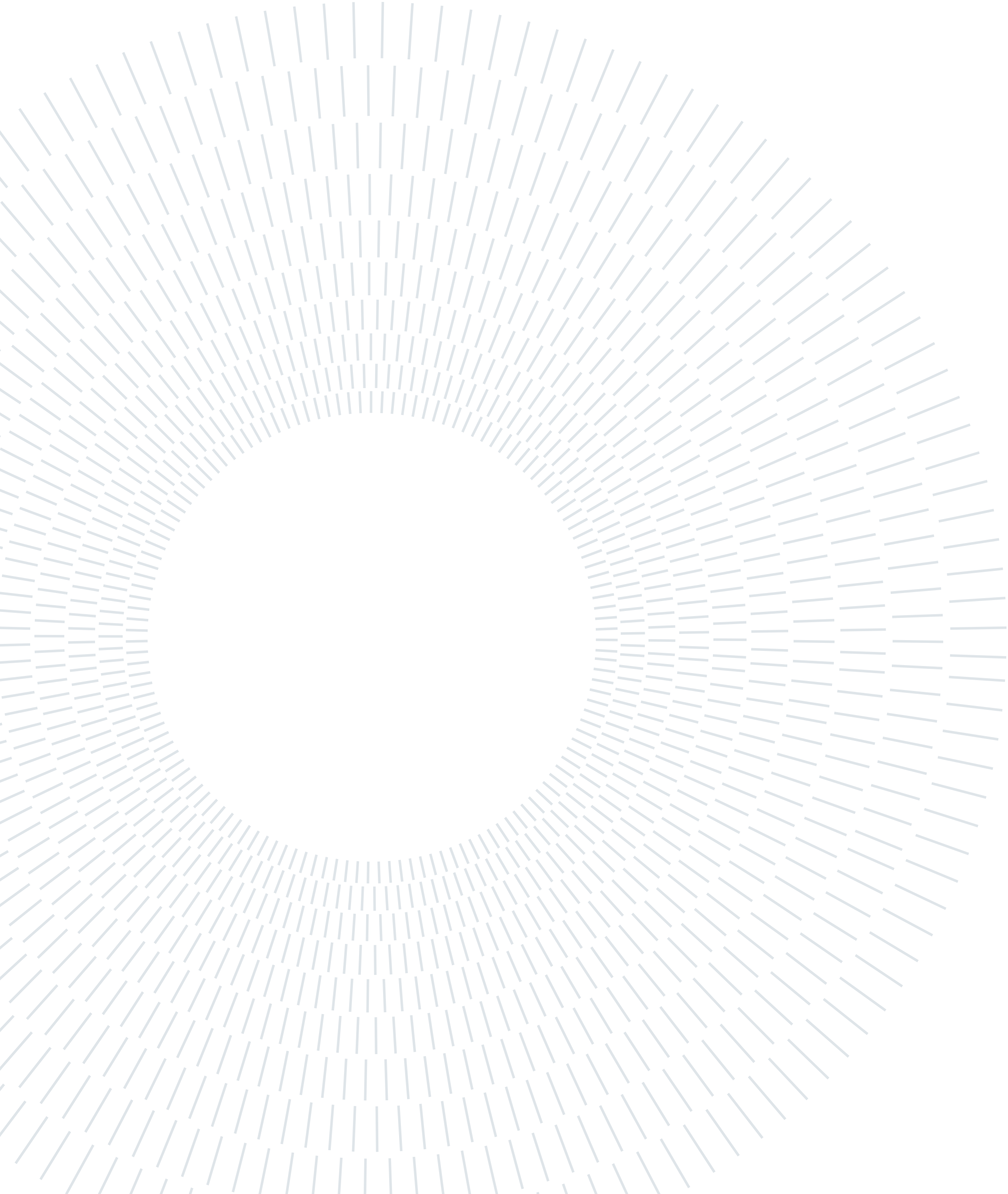

2 | From clinical image to computational domain

In this work we are interested in performing patient-specific simulations of the myocardial perfusion inside the left ventricle, by providing a 3D description of blood dynamics from the aortic root to the cardiac tissue, as explained in Section 1.5. Therefore, computational domains for the aortic root, epicardial coronary arteries and left ventricle had to be created. In order to create a patient-specific computational domain where the mathematical model is numerically solved two steps are needed:

1. patient-specific anatomical geometry reconstruction of aortic root, epicardial coronary arteries and left ventricle through image segmentation techniques;
2. generation of a computational mesh on the reconstructed geometries.

Regarding left ventricle and epicardial coronary arteries, reconstructed anatomical geometries were already available thanks to the work of Di Gregorio et al. [70], whereas the geometry of the aortic root had to be segmented in this work from the same clinical images used in [70]. The newly reconstructed geometry of the aortic root had to be then connected to the epicardial coronary arteries in order to generate a computational mesh on the connected structure, whereas a computational mesh for the left ventricle was available [70].

In this chapter we give an overview of the process that goes from medical images to a computational domain. In particular, in Section 2.1 we present the state of the art regarding image segmentation in cardiovascular applications, focusing on the techniques that have been enforced in this work, such as Thresholding (Sect. 2.1.1), Fast Marching (Sect. 2.1.2), Colliding Fronts (Sect. 2.1.3) and Level Set Method (Sect. 2.1.4). Then we discuss the available clinical data for this work (Sect. 2.2). The reconstruction of anatomical geometries is presented in Section 2.3, first for the already available geometries of epicardial coronary arteries and left ventricle (Sect. 2.3.1), then for the aortic root (Sect. 2.3.2). The mesh generation process is detailed in Section 2.4, highlighting the pre-processing steps performed on the separated structures of aortic root and epicardial coronary arteries (Sect. 2.4.1), the connection of the two structures (Sect. 2.4.2) and the generation of superficial and volumetric mesh on the connected structure (Sect. 2.4.3). Finally, the results obtained are presented in Section 2.5.

2.1. State of the art on image segmentation in cardiovascular applications

Image segmentation is the process of partitioning a digital image into multiple regions by assigning a label to each pixel of the image, so that pixels sharing the same label have similar characteristics. A medical image can be segmented in order to isolate organs, muscles or the lumen of a certain vascular region thanks to the detection of sharp changes in image brightness, representing the boundaries of these objects. In particular, in this study such technique was applied in order to reconstruct geometries of the aortic root by isolating their lumen.

Depending on the anatomy of the region one is interested in segmenting and the contrast of the image, several segmentation techniques can be used:

- *Manual techniques*: consist in a fully manual detection of the boundaries of interest. They are time consuming and often do not lead to reproducible results since they strongly depend on the operator performing the task. Thus, nowadays they are only applied in complex situations where other techniques do not provide accurate results, such as the segmentation of neurons [72].
- *Automatic techniques*: leverage algorithms and models to perform the segmentation without any manual input. They are time efficient and highly reproducible, but they do not always lead to satisfactory results. Indeed, such techniques perform well only in case of regular anatomical shapes, high contrast in brightness and absence of noise produced by adjacent structures (such structures can appear as bright as the region of interest). If large image databases are available, sophisticated algorithms based on artificial intelligence and machine learning can be developed to obtain an efficient automatic segmentation model, as it was done by Kano et al. [73] in order to train an automatic cervical tumor contour segmentation model.
- *Semi-automatic techniques*: hybrid techniques in which an automatic segmentation is performed based on some inputs and corrections provided by an operator. These are robust techniques which still guarantee time efficiency and a certain level of reproducibility. Due to the complex anatomy of the human body, particularly in pathological scenarios, there are several applications in which fully automatic seg-

mentation techniques fail in efficiently isolating the region one needs to reconstruct. Thus, semi-automatic techniques are still the most common for clinical image segmentation, some examples are the segmentation of the thoracic aorta [74], the lower extremity arterial tree [75] and the liver arterial perfusion territories [76].

Due to the presence of adjacent structures having similar grey values and the irregular morphology of the coronary arteries, only semi-automatic techniques were enforced for the reconstruction of the aortic root in this work and the reconstruction of the epicardial coronary arteries and left ventricle performed in [70]. Let us now briefly present some image segmentation techniques which were exploited for such reconstructions both in this work and in [70]. In particular, we present Thresholding and Fast Marching which are techniques used in different fields, Colliding Fronts which was particularly developed for cardiovascular applications in [77] and Level Set Method which is based on deformable models.

2.1.1. Thresholding

In its simplest form the Thresholding technique consists in replacing each pixel of an image with a black or white pixel, depending on if the image intensity is below or above a certain threshold value. Therefore passing from a greyscale image to a binary image (Fig. 2.1). The threshold value can be either selected manually by an operator or automatically by exploiting algorithms such as the Otsu's method [78].

(a) Original image. (b) Binary image.

Figure 2.1: Example of Thresholding segmentation technique. *Source Wikipedia*

An extension of this technique involves the selection of multiple threshold values, so that the pixels of the image are subdivided in several classes based on their grey level. Such extension can be used to isolate the portion of an image having grey values in a certain range.

A Thresholding technique provides an accurate segmentation when the image presents a homogeneous lighting and a low level of noise. Moreover, the portion of the image one wants to isolate has to be clearly separated from other portions having similar grey values, otherwise the segmentation would involve also unwanted regions of the image.

Due to its simplicity, there are not many clinical applications in which this technique provides accurate results as a standalone, but it can be combined with other segmentation techniques in order to achieve a more robust and reproducible segmentation process. Indeed, this is what is done in this work where a Thresholding technique is coupled with a Fast Marching (Sect. 2.1.2) or Colliding Fronts (Sect. 2.1.3) technique in a level set segmentation framework (Sect. 2.1.4) in order to reconstruct anatomical geometries of the aortic root.

Nonetheless, there are situations in which a Thresholding segmentation can be effectively applied to clinical images, such as Magnetic Resonance brain image segmentation [79] or bone segmentation from Computed Tomography images used in medical additive manufacturing [80].

2.1.2. Fast Marching

Fast Marching is a semi-automatic segmentation technique based on the propagation of a wave front inside the image, which was proposed by Sethian in [81]. It consists of manually placing a set of seed points and a set of target points on the image, so that wave fronts start propagating from each seed point in all directions with a velocity $I(\mathbf{x})$ and stop as soon as the first target point is reached. The area covered by the traveling wave fronts before reaching the targets represent the segmented region (Fig. 2.2).

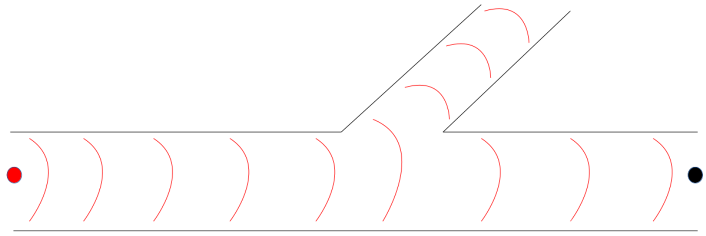

Figure 2.2: Schematic illustration of the Fast Marching method: one source point (red) and one target point (black) are selected inside this idealized vascular district. A wave front propagates inside the district until it reaches the target point, the region covered by the front at this moment is the segmented region. Note that also the bifurcating branch is therefore segmented.

Let us denote with $T_i(\mathbf{x})$ the time needed for the wave front originated from the i-th seed to reach the point $\mathbf{x}$. Then, such variable has to satisfy the Eikonal equation:

$$|\nabla T_i(\mathbf{x})| = \frac{1}{I(\mathbf{x})} \tag{2.1}$$

where $I(\mathbf{x})$ is the wave front propagation speed. Equation (2.1) can be numerically solved using the Fast Marching method [82].

The velocity of the fronts $I(\mathbf{x})$ depends on the local characteristics of the image, in particular a great velocity is achieved in areas with similar grey values while the velocity significantly decreases in presence of steep gradients in image intensity. So that only the regions having similar grey values are segmented.

Steep gradients in image intensity slow down the front propagation, therefore, for an accurate result, the image cannot be noisy, otherwise these gradients can be ill-defined and the front can propagate outside the region of interest. For this reason, in this work Fast Marching is combined with a Thresholding technique, so that wave fronts can only propagate in regions of the image having grey values in a certain range in order to avoid the segmentation of unwanted portions of the image.

This technique is well-suited for segmenting round objects and has been applied by Savic et al. for the detection of lung nodules [83]. But can be also enforced in elongated structures, indeed Jia et al. exploited the Fast Marching technique to compute the centerlines of the coronary arteries [84].

2.1.3. Colliding Fronts

Analogously to Fast Marching, also Colliding Fronts is a semi-automatic segmentation technique based on wave front propagation. In this case an operator has to manually select two sets of seed points for wave propagation, unlike for Fast Marching where one set of seeds and one set of targets are selected (no wave front propagates from the target points). A front propagating from a point belonging to one set of seeds stops when it reaches a point belonging to the other set of seeds. When front propagation stops, only the region of the image where two wave fronts collide represents the segmented region (Fig. 2.3).

We can still define the variable $T_i(\mathbf{x})$ for which the same Eikonal equation (2.1) holds. The difference with respect to Fast Marching is that now the method selects only the region of the image where the following additional property is satisfied:

$$\nabla T_i(\mathbf{x}) \cdot \nabla T_j(\mathbf{x}) < 0 \tag{2.2}$$

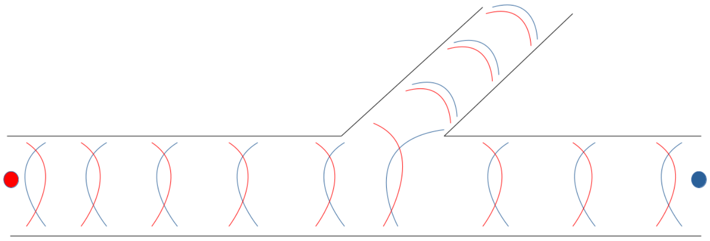

Figure 2.3: Schematic illustration of the Colliding Fronts method: two seed points (red and blue) are selected inside this idealized vascular district. Two wave fronts propagate from each point until they reach the other point, the region where the two fronts collide is the segmented region. So that, only the main branch of the district is segmented using Colliding Fronts.

where i is the index of a point belonging to the first set of seeds and j is the index of a point belonging to the second set of seeds. Therefore selecting the region of the image where two wave fronts collide.

Colliding Fronts represents an alternative to Fast Marching and is exploited in this work in combination with a Thresholding technique for the same reason explained in Section 2.1.2. The choice of using a Fast Marching or a Colliding Fronts technique depends on the particular application.

This technique is very effective for the segmentation of tubular structures, such as tracts of vessels. It has been enforced by Piccinelli et al. for the reconstruction of cerebral aneurysm [85] and by Klepaczko et al. to perform a cerebral arteries segmentation [86].

2.1.4. Level set method

Level sets are a kind of deformable model for the description of the time evolution of curves and shapes. In the image segmentation context, the deformable surface is not represented by a set of points and triangles, but rather described by a 3D function (basically another image) whose contour at level zero is the surface in question, see Figure 2.4. The advantage of using a deformable model is that the location of the surface will locally conform to the peaks of the gradient modulus of the image levels. In other words, the final surface will be located on the regions corresponding to the steepest change of image intensity.

Image segmentation based on the level set method is therefore strictly related to the time evolution of the *level set function* $\phi(\mathbf{x}, t)$, where $\mathbf{x}$ is a three dimensional point inside the image and t represent the time. A first raw segmentation of the image has to be performed in order to provide an initialization $\phi(\mathbf{x}, t = 0)$, then the function is free to evolve in order

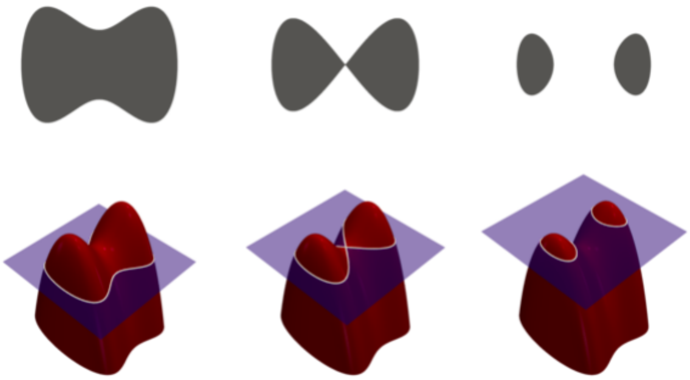

Figure 2.4: Schematic illustration the Level set method: in order to describe the evolution of the surface on top, the level set method exploit a higher dimensional function whose zero-level set is the boundary of the surface of interest. So that the original surface is represented by all the points at which the function is greater or equal to zero. *Source Wikipedia.*

to deform its zero level set (boundary of the isolated region). The shape of the boundary evolves in order to adapt to the curvature of the surface and the image gradients, while being described by the equation:

$$\phi(\mathbf{x}(t), t) = 0 \quad \forall t. \tag{2.3}$$

By integrating (2.3) in time we get:

$$\phi_t + \mathbf{x}_t \cdot \nabla\phi = 0 \quad \forall t$$

where ϕ_t and $\mathbf{x}_t$ are the temporal partial derivative of ϕ and $\mathbf{x}$, respectively. Now, let us suppose that $\mathbf{x}_t$ has only one component in the direction normal to the surface, namely $\mathbf{x}_t = F(\mathbf{x}(t))\mathbf{n} = F(\mathbf{x}(t))\frac{\nabla\phi}{|\nabla\phi|}$. So that,

$$\phi_t + F|\nabla\phi| = 0 \quad \forall t \tag{2.4}$$

where $F(\mathbf{x}(t))$ is called *speed function* and depends on the evolving surface characteristics (e.g. curvature, normal direction) and image characteristics (e.g. grey levels, gradients) [87]. In particular, the speed function F has to be calibrated in order to set proper weights to the different features of the model deformation, such as model inflation, surface regularization and surface adaptation to gradient modulus of image intensity.

Equation (2.4) regulates the time evolution of the level set function ϕ in such a way that its zero level set (boundary of interest) adapts to the surface and image characteristics thanks to the speed function F.

In this work we applied a level-set segmentation to reconstruct the anatomical geometry of the aortic root. In particular, the initialization of the method was performed using either a Fast Marching or Colliding Fronts technique combined with a Thresholding technique as explained in the previous sub-sections. Then, the surface resulting from this raw segmentation was deformed by properly calibrating the speed function F.

Level set approaches have been extensively used for image segmentation in clinical applications, some examples are: carotid artery [88], multiple sclerosis lesion [89] and cardiac ventricles [90].

2.2. Available clinical data

In this work the available clinical data are Coronary Computed Tomography Angiography (cCTA) images taken in rest conditions and provided to us by the Clinical Cardiology Unit & Department of Cardiovascular Imaging in Monzino Cardiology Centre, Milano. This imaging technique consists in an intravenous injection of contrast medium followed by computed tomography (CT) scanning in order to guarantee a clear visualization of the coronary arteries supplying blood to the heart.

CT is a diagnostic imaging modality which exploits the x-ray attenuation in the body to produce cross-sectional images. An x-ray tube rotates around the patient, who lies on a radio-transparent bed, and sends x-rays beams towards them. The attenuated x-ray is measured by a detector, which is positioned on the opposite side of the circular structure and rotates synchronously with the x-ray tube. The information about the x-ray attenuation are transformed in electrical signals and then in digital data, that can be processed by specialized software programs to obtain clinical images [91].

In our study tomographic 256-slice cCTA scans of the patients are used. Rest cCTA was performed with a Revolution CT scanner (GE Healthcare, Milwaukee, Wisconsin). The following parameters were used: slice configuration 256 x 0.625 mm with scintillator detector, to reach a 0.23 mm spatial resolution; gantry rotation time 280 ms; tube voltage 120 kVp and 100 kVp in patients with body mass index $> 30\ kg/m^2$ and $< 30\ kg/m^2$, respectively; effective tube current of 500 mA. One beat axial scan was used in all patients with a variable padding ranging from 70% to 80% and 40% to 80% of the cardiac cycle in patients with HR $< 65\ beats/min$ and $> 65\ beats/min$, respectively. All patients received a 70-ml bolus of iodixanol 320 (Visipaque 320 mg/ml, GE Healthcare, Oslo, Norway) at an infusion rate of 6.2 ml/s followed by 50 ml of saline solution at the same rate of infusion [92].

The reconstruction of both the left and right ventricles was not possible using these images, due to the selected time instants for CT acquisition. Indeed, the injected contrast medium reaches the two chambers with some delay, so an image where both ventricles are highly contrasted cannot be obtained. Moreover, reconstructing the two chambers from images taken in different time instants is not feasible due to the motion of the heart. For these reasons, only the left ventricle has been reconstructed from these images in [70]. This approach makes sense because an ischemic region located in the left ventricle can have more significant impact on the correct functioning of the heart, since this chamber regulates the whole systemic circulation.

The three main views of a single slice of a rest cCTA are reported in Figure 2.5. In each view the aortic sinus is clearly visible thanks to the contrast medium. In particular, the root of the left coronary artery tree can also be identified from the axial view (Fig. 2.5a), while part of the ascending aorta is visible in the Sagittal view (Fig. 2.5b). In the Coronal view (Fig. 2.5c) are visible all three components: aortic sinus, root of the left coronary artery tree and ascending aorta.

2.3. Anatomical Geometry reconstruction

Image segmentation techniques were applied to reconstruct the geometries of the left ventricle, epicardial coronary arteries and aortic root from rest cCTA images. The open-source software packages MITK (Medical Imaging Interaction Toolkit [93]) and VMTK (Vascular Modelling Toolkit [77]) have been extensively involved in the reconstruction of the anatomical geometries used in this project, together with novel techniques developed by Fedele et al. in [94].

2.3.1. Available reconstructed geometries

As already mentioned in the introduction of this chapter, in this work we leverage the reconstructions of the left ventricle and epicardial coronary arteries used in [70]. Let us briefly present the procedure applied for segmenting such geometries.

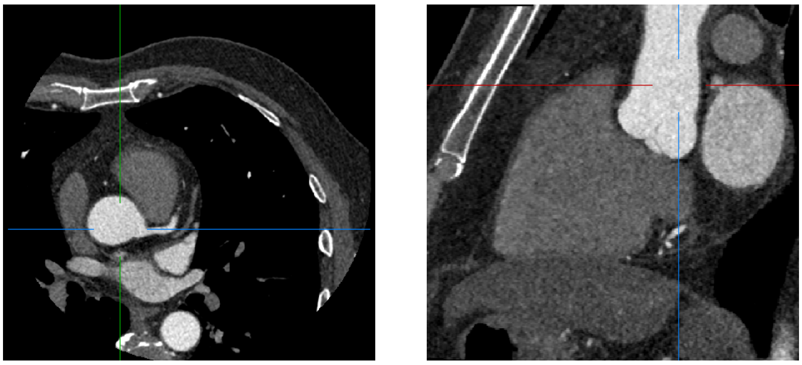

(a) Axial or transverse view. (b) Saggital view.

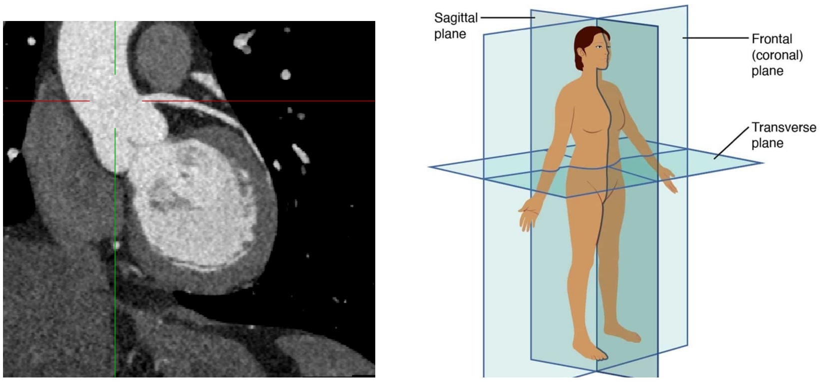

(c) Coronal view. (d)

Figure 2.5: Different views of a single slice cCTA: (a) the root of the left coronary branch is visible from the axial view; (b) the aortic sinus and part of the ascending can be identified from the saggital view; (c) in the coronal view the aortic sinus, root of the left coronary branch and ascending aorta are clearly visible; (d) illustration of the different views.

Left ventricle

For the reconstruction of the left ventricle geometry the following approach has been enforced in [70], as reported in Di Gregorio's PhD thesis [71]:

1. using MITK, perform a semi-automatic segmentation of the epicardial and endocardial surfaces (a fully automatic segmentation is not possible due to the presence of low-contrast boundaries such as with the pericardium);
2. cut both surfaces at the level of the annulus using VMTK;
3. connect the two surfaces with a triangulated surface using the script ***vmtksurfacecapper*** [94] in order to obtain a closed surface representing the left ventricle (Fig. 2.6);

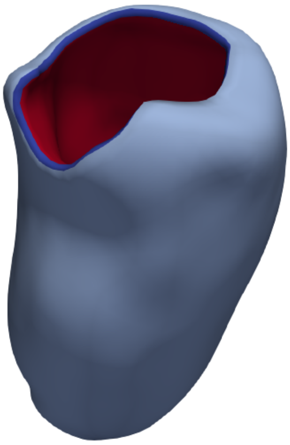

Figure 2.6: Example of a left ventricle reconstructed from rest cCTA images in [70]. The epicardium (light blue) and endocardium (red) are connected by the triangulated surface in blue. *Source* [71]

Epicardial coronary arteries

Due to the tortuosity and unpredictable anatomy of the epicardial coronary arteries, a fully automatic segmentation technique cannot be applied for the reconstruction of their geometry. Such arteries reduce their radius as they branch out, so that, approaching their distal ends, the vessels lumen becomes more difficult to track. Moreover, the contrast progressively reduces due to the noise provided by the intramural networks in the myocardium. Therefore, a pre-processing of the rest cCTA is needed before geometry segmentation in order to have a better visualization of the lumen. The epicardial coronary network has been reconstructed in [70] down to vessels having diameter around $1mm$, because the spatial resolution of the cCTA does not allow to track vessels under such dimension.

The anatomical geometry of epicardial coronary arteries was reconstructed in [70] following this procedure:

1. application of the vesselness filter provided by A. Frangi [95] to the rest cCTA images in VMTK;
2. level set segmentation performed after a Fast Marching or Colliding Fronts initialization [77]. If atherosclerotic plaques are detected, they are initially included in the lumen of the vessels (Fig. 2.7 - A);
3. segmentation of atherosclerotic plaques using MITK (Fig. 2.7 - B);
4. removal of atherosclerotic plaque tracts inside the lumen using the boolean difference

operator in VMTK (Fig. 2.7 - C);

5. smoothing of the resulting surface using the open source software Meshmixer (`https://www.meshmixer.com/`) to remove possible reconstruction defects;
6. computation of the centerlines of epicardial coronary arteries using VMTK and definition of the maximum radius values of inscribed spheres in each point of the centerlines;
7. generation of the final tubular surface of epicardial coronary arteries starting from the centerlines and selecting a radius of each section based on the radius previously calculated (Fig. 2.7 - D)

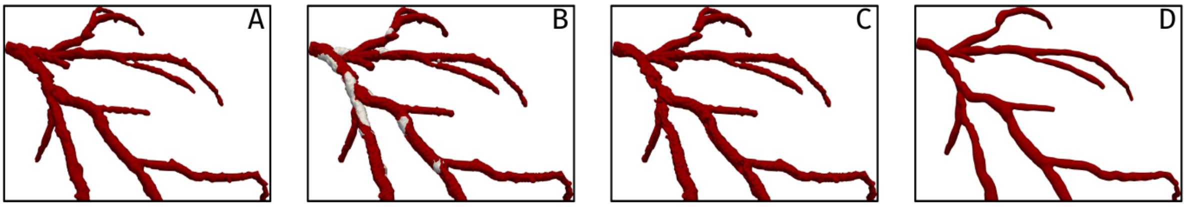

Figure 2.7: Example of an epicardial coronary network reconstructed from rest cCTA images in [70]. A) Lumen segmentation; B) plaque segmentation; C) plaque removal from the lumen; D) tubular surface generation. *Source* [71]

Since only the left ventricle could be reconstructed from cCTA images, in [70] Di Gregorio et al. focused on the myocardial perfusion of this chamber. For this reason, in order to save time and computational power they applied the procedure above to reconstruct only the vessels of the coronary arteries supplying blood to the left ventricle, thus excluding branches which supply the right ventricle and the atria.

However, the reconstruction procedure presented here can be enforced to obtain the full epicardial coronary tree geometry, which has been done in [70] for one patient as an example. Therefore, we performed standalone blood dynamics simulations inside aortic root and epicardial coronary arteries only for this patient in order to study the flow partition between left and right coronary branch. For the other patients is not possible to study the flow partition, due to the missing branches, thus only left ventricle myocardial perfusion simulations have been performed for these patients.

2.3.2. Newly reconstructed geometry: aortic root

The new contribution of this work in terms of anatomical geometry reconstruction is the segmentation of the aortic root, which was used to create the computational domain where the 3D Navier-Stokes problem is solved.

The aortic root presents a regular surface if compared to the coronary arteries, but the presence of adjacent structures having similar grey values makes it unfeasible to perform a fully automatic segmentation of its geometry, as for the left ventricle. Therefore, we have to perform a semi-automatic segmentation of the aortic root.

In particular, using the VMTK script ***vmtklevelsetsegmentation***, a level set segmentation technique, based on either a Fast Marching or Colliding Fronts initialization, is applied for the reconstruction of the aortic root. Moreover, VMTK allows the user to select a lower and upper threshold values, so that the wave front can propagate only in regions of the image having grey values between such thresholds, thus combining Thresholding and front propagation techniques. This is done to ensure a correct initialization in cases where the image intensity gradients at the boundary of the structure of interest are not steep enough to stop the front propagation.

The level set segmentation process is depicted in Figure 2.8. In particular, in Figure 2.8a we reported the clinical image, starting point of the process, in Figure 2.8b the initialization of the level set (in this case the Fast Marching method has been applied) and in Figure 2.8c the final structure, which is obtained from the initialization by deforming the model in order to better adapt it to the image gradients and the curvature of the surface.

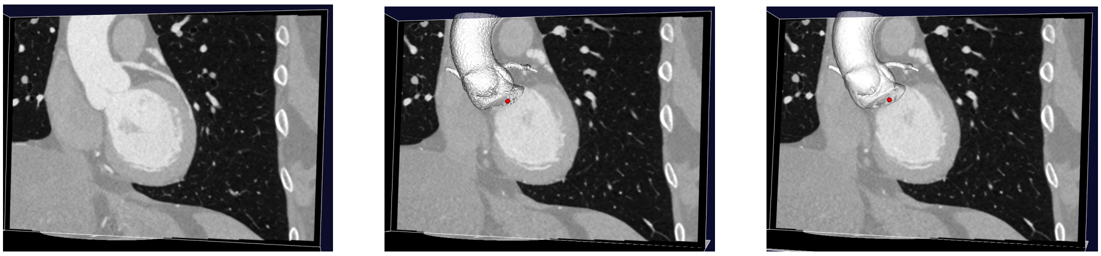
(a) (b) (c)

Figure 2.8: Level set segmentation process: (a) clinical image showing the aortic root we are interested in segmenting; (b) raw segmentation used as initialization for the level set method; (c) model deformation in order to adapt to surface curvature and image gradients.

After the segmentation of the geometry, the zero-level of the level set function is extracted using VMTK, representing the internal boundary of the aortic wall, see Figure 2.9.

Figure 2.9: Zero-level surface, extracted from the level set function, representing the internal wall of the aortic root. The roots of the two coronary branches can be identified on the reconstructed structure.

2.4. Building of the complete computational domain

In this work we are interested in simulating 3D blood dynamics inside the aortic root and the epicardial coronary arteries. To this purpose, after some pre-processing steps have been performed on the separated geometries, the two structures are connected in order to generate the computational domain where the mathematical model is numerically solved.

The computational mesh was designed both to provide numerical results which are virtually mesh independent and to preserve the geometrical details of the domain. First we generated a superficial mesh, whose mesh size was set by scaling the value of an array, defined on the whole domain boundary. Then, the volumetric mesh was created starting from the superficial one. This strategy gives us a lot of flexibility on the mesh size, as will be shown in this Section.

For the mesh generation process we still exploit the functionalities of VMTK developed in both [77] and [94], moreover the open-source data analysis and visualization application Paraview [96] is used.

2.4.1. Pre-processing on separated structures

Aortic root

The aortic root in Figure 2.9 can be subdivided in three regions: the aortic sinus (or sinus of Valsalva), the coronary roots (left and right) and the ascending aorta. In this project we are particularly interest in studying the coronary blood flow, therefore we ask for the final mesh to be more refined inside the aortic sinus (where CBF comes from) and the coronary roots, while it can be coarser inside the ascending aorta (since the blood flow in this region does not influence CBF). Moreover, a small mesh size in the coronary roots is needed to well describe the geometrical features of this region, due to the dimension of the coronary branches.

Let us present here the pre-processing steps performed on the reconstruction of the aortic root (Fig. 2.9) before connecting it to the epicardial coronary arteries:

1. using Paraview the reconstructed surface was cut, making sure that the inlet and outlet boundaries are almost perpendicular to the wall (physical boundary), for numerical reasons (Fig. 2.10a). We cut the outlet sections of the coronary roots a few millimeters away from the inlets of the reconstructed coronary artery tree so that they were ready to be connected (Fig. 2.10b);
2. using the VMTK script ***vmtksurfacetagger***, the aortic root structure was tagged differently in the three distinct regions: aortic sinus, coronary roots and ascending aorta (Fig. 2.11a). So that a particular mesh size could be set in the different areas of the domain.
3. Exploiting the tags, an array called *EdgeLengthSmooth* was defined on the surface:

$$\mathit{EdgeLengthSmooth} = \begin{cases} 1, & \text{in the coronary roots} \\ 2, & \text{in the aortic sinus} \\ 4, & \text{in the ascending aorta.} \end{cases} \tag{2.5}$$

   The mesh size will be set by scaling the value of *EdgeLengthSmooth*, so that the mesh size on the ascending aorta will be double the size on the aortic sinus and so on. Since we want the mesh size to vary continuously inside the domain, then we perform a smoothing of the value of the array near the boundary between two different tags (Fig. 2.11b).

The flexibility on the mesh size is clear already at this stage. As an example, in Figure 2.12 are shown three different superficial meshes for the aortic root. Each of these meshes was generated using the same array *EdgeLengthSmooth* defined in step 3. just by changing the scaling factor used to set the mesh size. Therefore, we can get each superficial mesh with only one line of code starting from the tagged surface where *EdgeLengthSmooth* was defined, thanks to the VMTK script ***vmtksurfaceremeshing***. Note that, due to the definition of *EdgeLengthSmooth*, the mesh size inside the ascending aorta is double the size inside the aortic sinus, which is double the size inside the coronary roots for all three

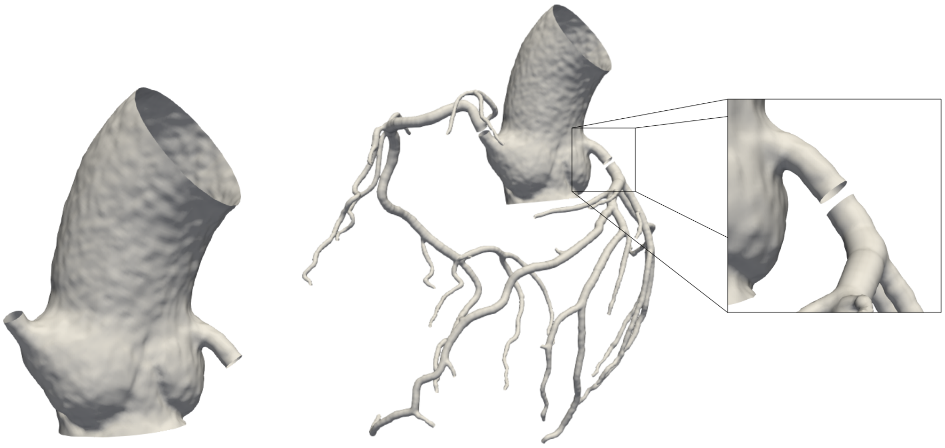

(a) (b)

Figure 2.10: (a) Aortic root structure after clipping via Paraview. (b) Distance left between the reconstructed geometries of aortic root and epicardial coronary arteries.

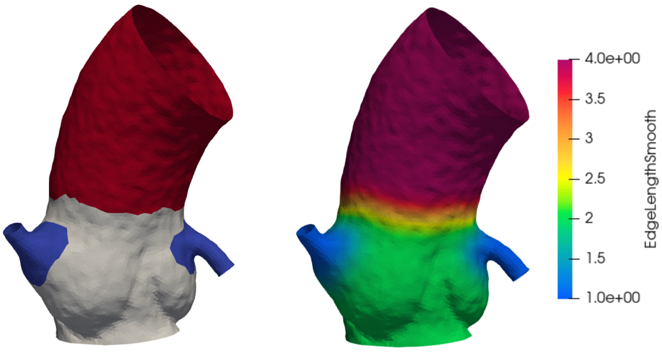

(a) (b)

Figure 2.11: (a) Tagged aortic root surface. (b) Array *EdgeLengthSmooth* defined exploiting the tags shown in Fig. 2.11a.

superficial meshes.

Epicardial coronary arterial tree

Before connecting the two structures (aortic root and epicardial coronary arteries), a new array has to be defined in order to set a radius dependent mesh size on the epicardial coronaries structure. This is done because the radius of the coronary vessels significantly changes across the network and a radius dependent mesh size allows us to describe the geometric features in small arteries while avoiding a too refined mesh in large arteries.

To this purpose, the centerlines of the coronary tree were computed in order to define an array called *DistanceToCenterlines*, which represents in each point of the centerlines the

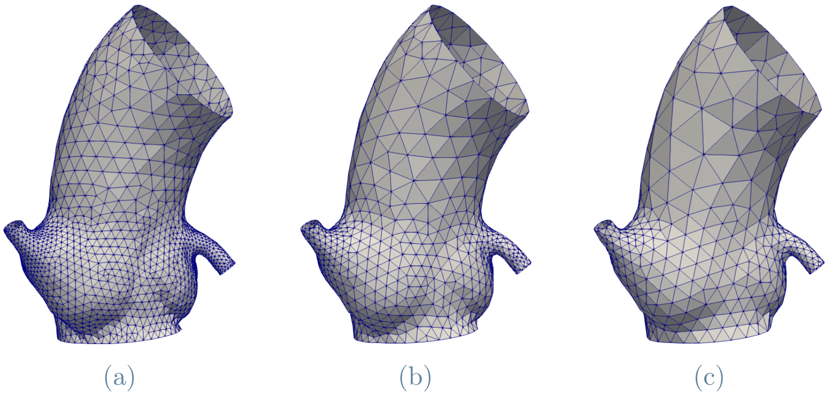

Figure 2.12: Superficial meshes for the aortic root with different levels of refinement. The mesh size of each superficial mesh is set by scaling the value of *EdgeLengthSmooth* in each point of the domain, just changing the scaling factor.

radius of the maximum inscribed sphere (Fig. 2.13).

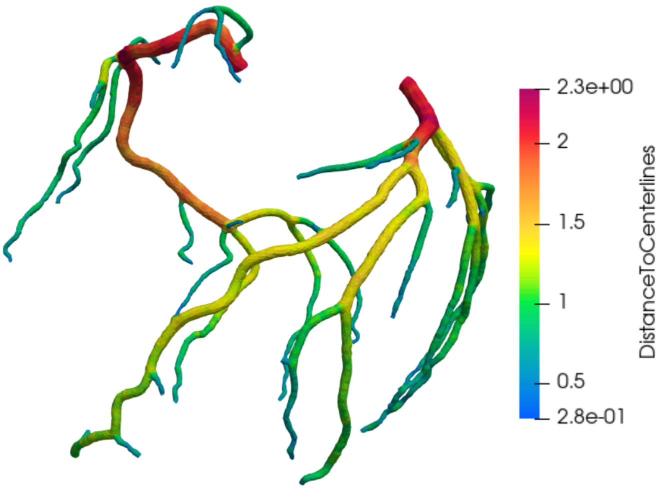

Figure 2.13: Array *DistanceToCenterlines*, defined on the reconstruction of the epicardial coronary artery tree.

2.4.2. Connection of the structures

The two surfaces (epicardial coronary artery tree and aortic root) are now ready to be connected using the script ***vmtksurfaceconnector***, which connects two open boundary rings belonging to two different structures by artificially creating some triangular elements in the connection area.

The two boundary rings have to be close enough so that the artificially reconstructed area does not influence too much the overall precision of the geometry. Nonetheless, for an effective result it is better to take them not too close.

The creation of the artificial elements in the connection area depends on the number of points contained in each of the rings to be connected. For an accurate result it is better to connect rings having a similar number of points, therefore it is good practice to perform an initial re-meshing step before the connection.

In Figure 2.14a the resulting connected structure is shown and the artificially created elements in the connection area between the aortic root and the left coronary artery tree are highlighted. There are jumps in mesh size at the boundary between the structures and the connection area due to triangular elements artificially created by the VMTK script.

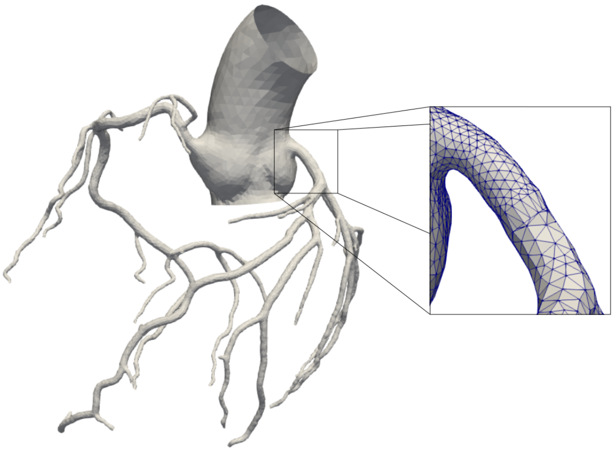

(a)

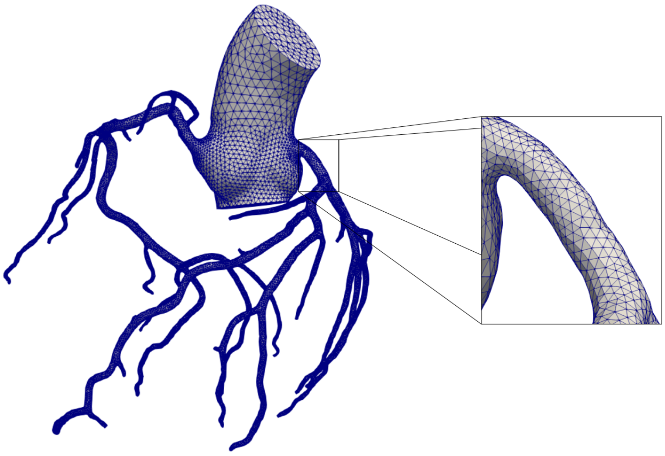

(b)

Figure 2.14: (a) Output of ***vmtksurfaceconnector***, focusing on the connection area between aortic root and left coronary branch. (b) Superficial mesh for the connected structure. The mesh size is now varying continuously across the whole domain, also in the connection area.

2.4.3. Superficial and volumetric mesh for the connected structure

Analogously to what was done for the aortic root structure, we want to define a new array on the connected structure and use it to set the mesh size of a superficial mesh.

The new array, called *GlobalH*, coincides with *EdgeLengthSmooth* on the aortic root, whereas it is a function of *DistanceToCenterlines* on the epicardial coronary arteries, namely:

$$GlobalH = \begin{cases} EdgeLengthSmooth, & \text{on the aortic root} \\ \alpha * (DistanceToCenterlines)^{\beta}, & \text{on the epicardial coronaries} \end{cases} \tag{2.6}$$

where the parameters α and β have to be manually tuned in order to guarantee that:

- *GlobalH* is continuous in the connection area;
- the geometrical details of the small arteries are preserved;
- the computational cost of simulating inside the mesh does not become too high.

A representation of *GlobalH*, is provided in Figure 2.15.

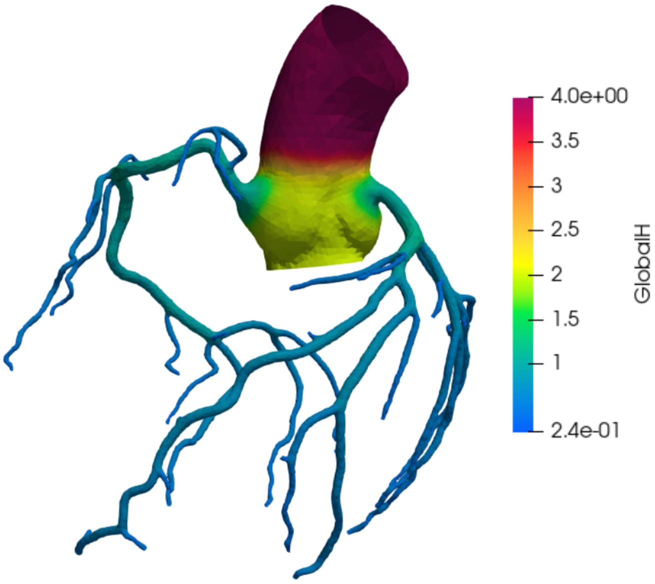

Figure 2.15: Array *GlobalH*, defined on the connected structure.

Note that, in case of a proper selection of α and β, *GlobalH* is a continuous array, therefore a superficial mesh generated exploiting its definition presents a continuous mesh size throughout the domain.

The inlet and outlet sections of the surface are still open and have to be closed in order to generate a volumetric mesh on the geometry. The VMTK script ***vmtksurfacecapper*** was used to perform this operation.

We are now ready to generate a superficial mesh on the surface representing aortic root and epicardial coronary arteries. Thanks to the definition of *GlobalH* we will get a radius dependent mesh size on the coronaries, whereas on the aortic root we have the three levels of refinement set by *EdgeLengthSmooth.* There are no more jumps in mesh size, which varies continuously across the whole structure going from 4 mm in the ascending aorta down to 2.4x10^{-1} mm in the smallest coronary arteries. In Figure 2.14b the superficial mesh is represented, highlighting the continuity of the mesh size in the connection area.

Again, the flexibility of our approach can be exploited to generate different superficial meshes starting from the value of *GlobalH* and changing the scaling factor used to set the mesh size, as shown in Figure 2.16.

Once the superficial mesh has been fixed we passed to a three-dimensional mesh using the script ***vmtkmeshgenerator***. Note that, since we have already set a superficial mesh size and capped the structure, we skipped the re-meshing and capping steps that this script can perform. Thus the script only fills the void volume inside the closed surface with tetrahedral elements, whose size depends on the size of the triangular elements of the superficial mesh.

VMTK is optimized for working with triangular and tetrahedral elements. Nonetheless, once a volumetric tetrahedral mesh is generated we can pass to a hexahedral one using the script ***vmtkmeshtethex***, which splits each tetrahedral element into four hexahedral elements, significantly reducing the size of each element. The software used in this study to perform numerical simulations supports both hexahedral and tetrahedral meshes. Therefore, we decided to use tetrahedral meshes in order to have a direct control on the mesh size and possibly reduce the computational cost of the simulation. Anyway, the same processing steps can be applied to obtain an hexahedral computational mesh, just accounting for the reduction in mesh size due to the transformation from tetrahedra to hexahedra.

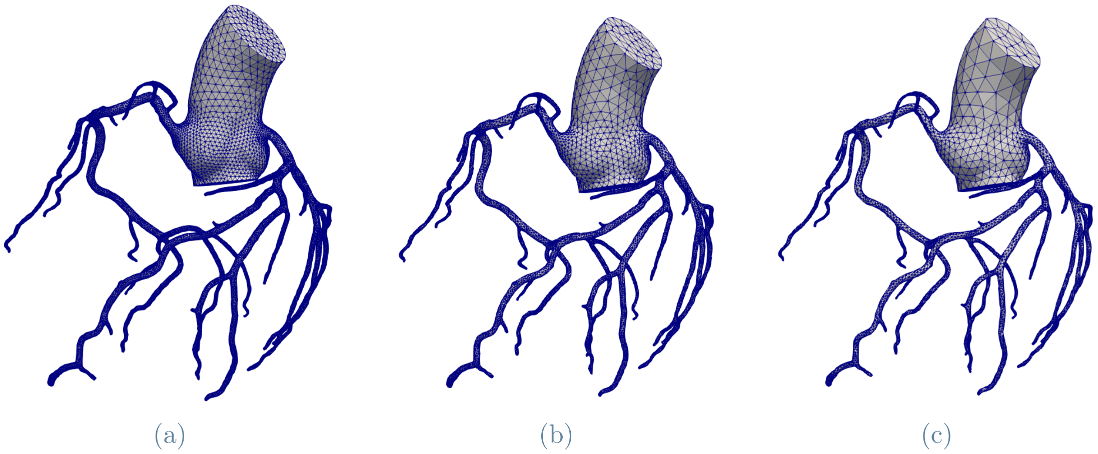
(a) (b) (c)

Figure 2.16: Superficial meshes for the connected geometry with different levels of refinement. The mesh size of each superficial mesh is set by scaling the value of *GlobalH* in each point of the domain, just changing the scaling factor.

2.5. Results

We have applied the procedure detailed in this chapter to generate four patient-specific computational domains of aortic root and epicardial coronary arteries. Moreover, patient-specific hexaedral meshes for the left ventricle were already available for each patient. Using VMTK such meshes were generated starting from tetrahedral meshes, as explained in Section 2.4.3. In the case of the ventricle we need a hexahedral mesh due to technical reasons, which depend on the software used for the simulations.

Remember that we aim to simulate blood dynamics from the aortic root to the myocardial capillaries by coupling a 3D Navier-Stokes problem with a multi-compartment description of the myocardium. The Navier-Stokes problem is solved in the tetrahedral mesh representing aortic root and epicardial coronaries while the Darcy problem is solved inside the hexahedral mesh of the left ventricle. This can be done since, as it will be explained in Section 4.3, the two problems are solved sequentially.

The resulting patient-specific computational domains are reported in Figure 2.17. These four patients are considered healthy and represent a subset of the nine patients forming the study population of [70], for the remaining five patients a functionally significant coronary artery disease was detected. We decided to initially work only with healthy patients in order to asses the performance of the models in physiological cases, the application to pathological cases can provide meaningful insights in future studies. For patients P2 and P3 we were able to reconstruct from the cCTA a bigger portion of the ascending aorta

(Fig. 2.17b 2.17c).

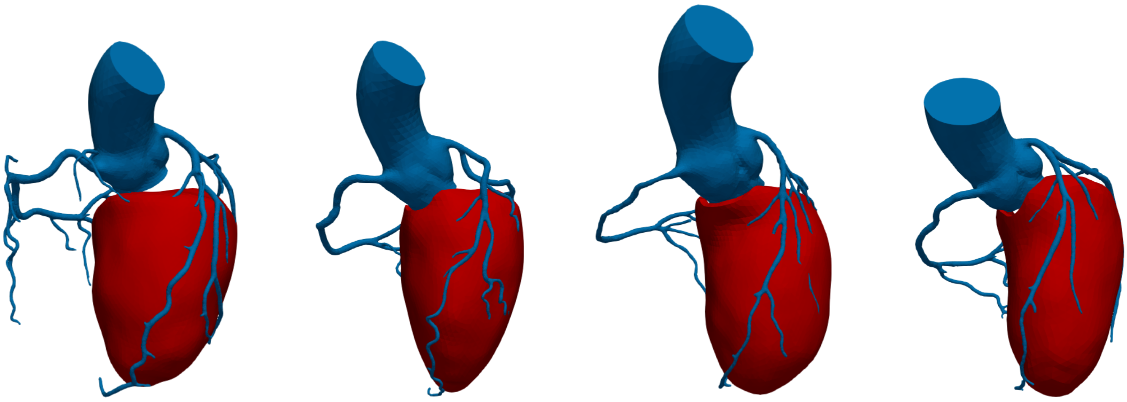

(a) P1. (b) P2. (c) P3. (d) P4.

Figure 2.17: Computational domains for aortic root and epicardial coronary arteries (blue) and left ventricle (red) in four patient-specific cases.

3 | Computational hemodynamics in aortic root and epicardial coronary arteries

Before applying our new modeling framework to the numerical simulation of patient-specific myocardial perfusion, we are interested in studying hemodynamics inside aortic root and epicardial coronary arteries as a standalone problem.

This chapter is structured as follows:

- In Section 3.1 we first present the governing equations used in this work to model blood dynamics in the considered domain.
- In Section 3.2 we introduce a particular weak formulation, based on the Lagrange multipliers method, to deal with a *defective* flow rate boundary condition.
- In Section 3.3 we detail the numerical approximation of the presented equations, considering temporal discretization (Sect. 3.3.1), spatial discretization (3.3.2) and algebraic counterpart (Sect. 3.3.3).
- In Section 3.4 the implementation on the Finite Element library $life^x$ of the numerical methods needed to perform simulations is described.
- In Section 3.5 numerical results obtained in a cylindrical idealized geometry are presented in order to assess the validity of the implemented numerical methods.
- In Section 3.6 we report some numerical results obtained in a patient-specific geometry of aortic root and epicardial coronary arteries. First we assess their physiological consistency (Sect. 3.6.1), then we study an alternative scenario to achieve a more accurate flow partition between left and right coronary artery tree (Sect. 3.6.2).
- In Section 3.7 we provide some final remarks on the standalone model for hemodynamics inside aortic root and epicardial coronary arteries.

3.1. Navier-Stokes equations

In this work we model blood dynamics inside the aortic root and epicardial coronary artery using the 3D formulation of the Navier-Stokes (NS) equations. This approach provides a greater accuracy and allows for a better representation of the anatomical features of a particular patient with respect to reduced order models, at the price of a much higher computational cost for the numerical resolution of the equations. In pathological cases, involving stenosis and luminal narrowing, a complete 3D description is necessary to capture the flow disturbances downstream an occlusion. Such functional assessment of an occlusion is of utmost importance in clinical practice, therefore a 3D hemodynamics description is chosen.

As a first approximation, we consider in this work the rigid wall assumption. Such assumption does not hold true in reality, since the aortic root and the coronary arteries are compliant structures able to deform due to the action of blood pressure. This is particularly relevant for the aorta, whereas it is negligible in the coronaries, even if coronary compliance allows one to model the closing of the vessel due to the cardiac contraction. In this first work considering the coupling between aortic root, coronaries and cardiac perfusion we are mainly interested in the diastolic phase (open vessels) and we accepted an approximate solution in the aorta, therefore we ignored FSI.

Lastly, we assumed to be working with a homogeneous, incompressible and Newtonian fluid, which makes sense in large vessels [23, 24], such as the aorta and the epicardial coronary arteries.

The computational domain Ω_{AC}, representing the aortic root and the epicardial coronary arteries of a specific patient, is depicted in Figure 3.1 together with all its different boundaries. The only physical boundary is Γ_w, which is usually denoted as wall and has to be intended as the luminal endothelium. All the other boundaries are artificial boundaries, since we artificially created them for simulation purposes, but they do not exist in reality. Such boundaries comprises: the aortic inlet cross-section Γ_{in}, the aortic outlet cross-section Γ_{out} and the coronary outlet cross-sections Γ^j, where j is the index of each section.

Let us introduce now the 3D Navier-Stokes equations used to model blood dynamics inside

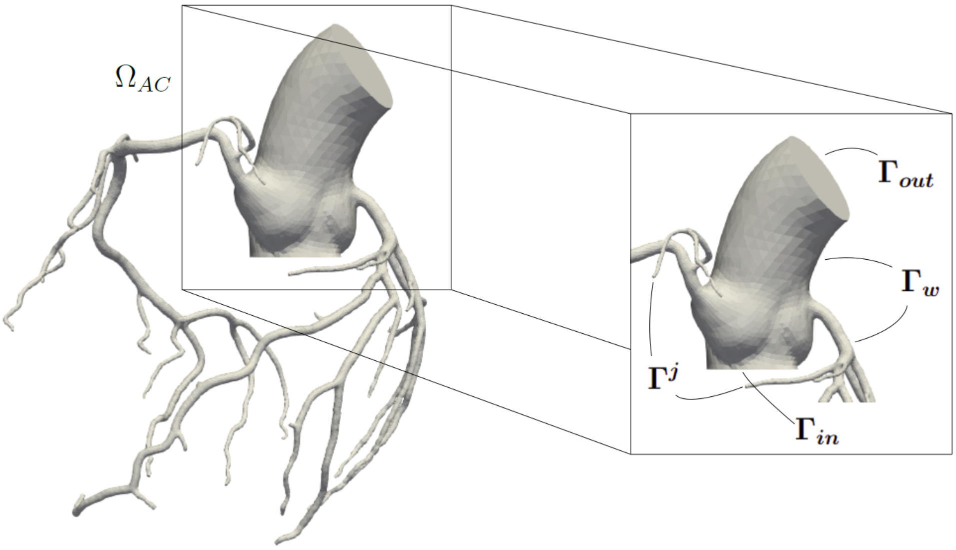

Figure 3.1: Reconstructed computational domain for aortic root and entire epicardial coronary arterial tree. The volumetric domain Ω_{AC} is represented with its boundaries: wall Γ_w, aortic inlet Γ_{in}, aortic outlet Γ_{out} and coronaries outlets Γ^j.

the computational domain Ω_{AC} (Fig. 3.1):

$$\begin{cases} \rho(\partial_t \mathbf{u} + (\mathbf{u}\cdot\nabla)\mathbf{u}) - \mu\nabla\cdot(\nabla\mathbf{u} + \nabla\mathbf{u}^T) + \nabla p = \mathbf{0} & in\ \Omega_{AC}, \\ \nabla\cdot\mathbf{u} = 0 & in\ \Omega_{AC}, \\ \mathbf{u} = \mathbf{0} & on\ \Gamma_w, \\ \mathbf{u} = \mathbf{u}_{in} & on\ \Gamma_{in}, \\ -p\mathbf{n} + \mu(\nabla\mathbf{u} + \nabla\mathbf{u}^T)\mathbf{n} = \mathbf{h}_N^j & on\ \Gamma^j, \\ \int_{\Gamma_{out}} \mathbf{u}\cdot\mathbf{n} = Q_{out} & on\ \Gamma_{out}. \end{cases} \tag{3.1}$$

The first equation derives from the conservation of linear momentum: $\mathbf{u}$ and p are the unknown blood velocity and pressure fields, respectively, ρ the blood pressure and μ the blood dynamic viscosity. Whereas, the second equation derives from mass conservation. Both equation are solved in the volumetric domain Ω_{AC}.

The other four equations are the boundary conditions expressed on each boundary of the domain: on Γ_w we impose a null velocity field (homogeneous Dirichlet condition), due to the rigid wall assumption (no-slip condition); on Γ_{in} we prescribe a physiological velocity profile $\mathbf{u}_{in}$ (non homogeneous Dirichlet condition), indeed we know from literature that the blood velocity has almost a flat spatial profile on the aortic inlet; on each Γ^j we fix the components of the Cauchy normal stress tensor through the function $\mathbf{h}_N^j$ (Neumann condition), in order to obtain physiological pressure values on these sections.

Let us now focus on the last equation, which provides an average condition on the velocity field, in particular it prescribes the flow rate through Γ_{out} using a time dependent function Q_{out}. In order to guarantee the existence of a solution for a Navier-Stokes problem in classical settings, a number of conditions equal to the spatial dimension of the problem has to be prescribed in each point of the domain boundary [97]. Our problem is 3D, but on Γ_{out} we are just prescribing an average condition, thus this is not enough to close the system and we denote such condition as a *defective* flow rate condition. In order to deal with such defective condition we have to introduce an augmented weak formulation of the problem, as it will be shown in Section 3.2. For the moment, let us explain the reasoning behind such an approach.

In this work we are interested in numerically studying the flow partition between left and right coronary branches in physiological conditions using patient-specific geometries. To this purpose, we want to impose a physiological flow rate incoming and outgoing the considered portion of the aorta and analyze how the flow distributes between the two coronary branches. A possible strategy is to impose a velocity profile on the aortic outlet using a Dirichlet condition, analogously to what was done for the aortic inlet. However, the spatial distribution of the velocity field in the ascending aorta is very chaotic, thus selecting *a priori* an accurate spatial profile on Γ_{out} is unfeasible and can lead to numerical instabilities. Another possible strategy is to work with pressures, thus prescribing Neumannn conditions both on Γ_{in} and Γ_{out} in order to achieve a physiological flow rate inside the aortic portion. Also this strategy can lead to numerical instabilities due to the use of a Neumann condition in inlet. For this reasons, we decided to work with a defective flow rate condition on Γ_{out}.

The Lagrange multipliers method is applied for the prescription of the defective flow rate condition, because, as will be shown in the next section, it allows to impose a flow rate through the aortic outlet cross-section Γ_{out} without fixing *a priori* the spatial profile of the velocity field on that section.

3.2. Lagrange multipliers method for defective flow rate boundary condition

The Navier-Stokes problem arising from the system of equations (3.1) is not well-posed in classical settings, due to the scalar boundary condition prescribed on the aortic outlet cross-section. In order to recover well-posedness we want to devise an augmented weak formulation of the problem, which involves a Lagrange multiplier. In fact, this formulation selects one particular solution among all the physical solutions of the original differential problem thanks to an "implicit" Neumann-like boundary condition acting on section Γ_{out} [97].

Let us first introduce some functional spaces:

$$\begin{aligned} &V = \{\mathbf{v} \in [H^1(\Omega_{AC})]^3 : \mathbf{v}|_{\Gamma_w} = \mathbf{0} \ \wedge \ \mathbf{v}|_{\Gamma_{in}} = \mathbf{u}_{in}\}, \\ &V_0 = \{\mathbf{v} \in [H^1(\Omega_{AC})]^3 : \mathbf{v}|_{\Gamma_w} = \mathbf{0} \ \wedge \ \mathbf{v}|_{\Gamma_{in}} = \mathbf{0}\}, \\ &Q = L^2(\Omega_{AC}). \end{aligned} \tag{3.2}$$

We are now ready to define the augmented weak formulation used to recover a well-posed NS problem starting from formulation (3.1).

Problem 3.1. *Given ρ, μ, $\boldsymbol{h}_N^j$ $\forall j$, Q_{out} and $\boldsymbol{u}_0 \in V$, find $\boldsymbol{u} \in V$, $p \in Q$ and $\lambda \in \mathbb{R}$ such that $\boldsymbol{u} = \boldsymbol{u}_0$ if $t = 0$ and for each $t > 0$ it holds true:*

$$\begin{cases} \rho\,(\partial_t \boldsymbol{u} + (\boldsymbol{u}\cdot\nabla)\boldsymbol{u}, \boldsymbol{v}) + \mu(\nabla\boldsymbol{u} + \nabla\boldsymbol{u}^T, \nabla\boldsymbol{v}) + \lambda(\boldsymbol{v}, \boldsymbol{n})_{\Gamma_{out}} & \\ \qquad\qquad -(p, \nabla\cdot\boldsymbol{v}) = \displaystyle\sum_{j=1}^{N_j} (\boldsymbol{h}_N^j, \boldsymbol{v})_{\Gamma^j} & \forall \boldsymbol{v} \in V_0, \\ (q, \nabla\cdot\boldsymbol{u}) = 0 & \forall q \in Q, \\ (\boldsymbol{u}, \boldsymbol{n})_{\Gamma_{out}} = Q_{out} & \end{cases} \tag{3.3}$$

where $(\cdot,\cdot)$, $(\cdot,\cdot)_{\Gamma_{out}}$ and $(\cdot,\cdot)_{\Gamma^j}$ denote the L^2 product in Ω_{AC}, Γ_{out} and Γ^j $\forall j$, respectively; N_j is the total number of coronary outlet sections; λ is a Lagrange multiplier used in order to impose the defective flow rate condition in a weak sense.

Proposition 3.1 (Well-posedness of the Augmented formulation). *For sufficiently small boundary datum Q_{out} and initial datum $\boldsymbol{u}_0$* Problem 3.1 *is locally well-posed, i.e. there exists a time $T^* > 0$ such that a solution $(\boldsymbol{u}, p, \lambda)$ exists in $[0, T^*]$.* [98]

The proof of this theorem is rather complex, thus please refer to [98].

Proposition 3.2. *Any smooth solution of* Problem 3.1 *satisfies the additional boundary conditions:*

$$\begin{cases} [p - \mu(\nabla\boldsymbol{u} + \nabla\boldsymbol{u}^T)\boldsymbol{n}\cdot\boldsymbol{n}]\Big|_{\Gamma_{out}} = \lambda \\ [\mu(\nabla\boldsymbol{u} + \nabla\boldsymbol{u}^T)\boldsymbol{n}\cdot\boldsymbol{\tau}_i]\Big|_{\Gamma_{out}} = 0, \quad i = 1, 2 \end{cases} \tag{3.4}$$

namely, both the normal and tangential components of the normal Cauchy stress tensor are constant over the section Γ_{out} ($\boldsymbol{\tau}_i$, $i = 1, 2$, are the two tangential unit vectors on Γ_{out}). In particular, the normal component is equal to the Lagrange multiplier λ and the tangential components are equal to zero. Furthermore, $(\boldsymbol{u}, p)$ satisfies the original system of differential equations (3.1). [97]

Proof. The Dirichlet conditions on Γ_w ($\mathbf{u} = \mathbf{0}$) and Γ_{in} ($\mathbf{u} = \mathbf{u}_{in}$) and the defective flow rate condition on Γ_{out} ($\int_{\Gamma_{out}} \mathbf{u} \cdot \mathbf{n} = Q_{out}$) are trivially satisfied. Integrating by parts the first equation of (3.3) yields for any $\mathbf{v} \in V_0$:

$$\begin{aligned}(\rho[\partial_t \mathbf{u} + (\mathbf{u} \cdot \nabla)\mathbf{u}] - \mu \nabla \cdot (\nabla \mathbf{u} + \nabla \mathbf{u}^T) + \nabla p, \mathbf{v}) \\ + \sum_{j=1}^{N_j} \int_{\Gamma^j} [-p\mathbf{n} + \mu(\nabla \mathbf{u} + \nabla \mathbf{u}^T)\mathbf{n} - \mathbf{h}_N^j] \cdot \mathbf{v} \\ + \int_{\Gamma_{out}} [-p\mathbf{n} + \mu(\nabla \mathbf{u} + \nabla \mathbf{u}^T)\mathbf{n} + \lambda \mathbf{n}] \cdot \mathbf{v} = 0. \quad (3.5)\end{aligned}$$

Now, taking $\mathbf{v} \in \mathcal{D}(\Omega_{AC})$ we recover the momentum equation of (3.1) in the sense of $\mathcal{D}'(\Omega_{AC})$. Consequently, from (3.5), it follows that:

$$\begin{aligned}\sum_{j=1}^{N_j} \int_{\Gamma^j} [-p\mathbf{n} + \mu(\nabla \mathbf{u} + \nabla \mathbf{u}^T)\mathbf{n} - \mathbf{h}_N^j] \cdot \mathbf{v} \\ + \int_{\Gamma_{out}} [-p\mathbf{n} + \mu(\nabla \mathbf{u} + \nabla \mathbf{u}^T)\mathbf{n} + \lambda \mathbf{n}] \cdot \mathbf{v} = 0 \quad \forall \mathbf{v} \in V. \quad (3.6)\end{aligned}$$

Multiplying the Cauchy normal stress tensor on Γ_{out} first by the outer normal vector $\mathbf{n}$ and then for the tangential unit vectors, denoted by $\boldsymbol{\tau}_i$, $i = 1, 2$, we deduce that:

- $[-p\mathbf{n} + \mu(\nabla \mathbf{u} + \nabla \mathbf{u}^T)\mathbf{n}]\Big|_{\Gamma^j} = \mathbf{h}_N^j \quad \forall j \in [1, N_j]$,
- $[p - \mu(\nabla \mathbf{u} + \nabla \mathbf{u}^T)\mathbf{n} \cdot \mathbf{n}]\Big|_{\Gamma_{out}} = \lambda$ and $\mu(\nabla \mathbf{u} + \nabla \mathbf{u}^T)\mathbf{n} \cdot \boldsymbol{\tau}_i\Big|_{\Gamma_{out}} = 0 \quad i = 1, 2.$

Therefore $(\mathbf{u}, p)$ is a solution of (3.1) which satisfies the additional boundary conditions (3.4). □

This proof was taken from [97] and adapted to our particular problem.

3.3. Numerical approximation

In this Section we present the numerical methods applied to provide an approximated solution of the Problem 3.1. For the spatial discretization of the problem we followed a

Finite Element approach, while a Finite Difference method is used for its temporal discretization. Finally, we report the algebraic counterpart, which is what it is implemented in practice in order to numerically solve the problem.

3.3.1. Temporal discretization and linearization

We are interested in numerically solving Problem 3.1 in the time interval $[0, T]$, which represents an heartbeat. Let us subdivide the time interval into N_t sub-intervals of constant length $\Delta t = \frac{T}{N_t}$ and define the time-steps $t^n := n\Delta t$, $n = 0, ..., N_t$. So that, given a function of time $z(t)$, we can denote as z^n the approximation of $z(t^n)$. In particular:

$$\mathbf{u}^n(\mathbf{x}) \approx \mathbf{u}(\mathbf{x}, t^n) \tag{3.7}$$

We consider a discretization of the time derivative via a Backward Difference Formula (BDF) of order 1:

$$\frac{\partial \mathbf{u}(\mathbf{x}, t^{n+1})}{\partial t} \approx \frac{\mathbf{u}(\mathbf{x}, t^{n+1}) - \mathbf{u}(\mathbf{x}, t^n)}{\Delta t}, \tag{3.8}$$

and a semi-implicit treatment of the convective term $(\mathbf{u} \cdot \nabla)\mathbf{u}$.

Thus, the augmented weak formulation (3.3) is discretized in time at $t = t^{n+1}$ as:

$$\begin{cases} \rho \left(\dfrac{\mathbf{u}^{n+1} - \mathbf{u}^n}{\Delta t} + (\mathbf{u}^n \cdot \nabla)\mathbf{u}^{n+1}, \mathbf{v} \right) + \mu(\nabla \mathbf{u}^{n+1} + \nabla {\mathbf{u}^{n+1}}^T, \nabla \mathbf{v}) & \\ \qquad + \lambda^{n+1}(\mathbf{v}, \mathbf{n})_{\Gamma_{out}} - (p^{n+1}, \nabla \cdot \mathbf{v}) = \displaystyle\sum_{j=1}^{N_j} ({\mathbf{h}_N^j}^{\,n+1}, \mathbf{v})_{\Gamma^j} & \forall \mathbf{v} \in V_0, \\ (q, \nabla \cdot \mathbf{u}^{n+1}) = 0 & \forall q \in Q, \\ (\mathbf{u}^{n+1}, \mathbf{n})_{\Gamma_{out}} = Q_{out}^{n+1} & \end{cases} \tag{3.9}$$

where the dependence on space is understood.

The semi-implicit treatment was chosen in order to avoid the presence of the non-linear convective term $(\mathbf{u}^{n+1} \cdot \nabla)\mathbf{u}^{n+1}$, which gives rise to a non-linear problem, significantly increasing the complexity of numerically solving the approximated problem. Due to this linearization, the stability of the numerical solution is guaranteed under a CFL-like condition on Δt, namely $\Delta t \lesssim h_{min}$, where h_{min} is the minimal element size of the computational mesh for Ω_{AC} [99].

An alternative strategy which furthermore simplifies the solution of the discretized problem is to treat explicitly all the unknowns of the problem, leading to another CFL-like condition: $\Delta t \lesssim h_{min}^2$. In this study we work with a very refined computational mesh in order to capture the geometrical details of the coronary circulation, thus this condition is too restrictive on the possible values of Δt. For this reason we opted for a semi-implicit treatment of the convective term, while all other terms are treated implicitly.

3.3.2. Spatial discretization

Regarding the spatial discretization of the considered problem we followed a Finite Element approach: we introduce a triangulation $\mathcal{T}^h$ of the continuous domain Ω_{AC}; exploiting the triangulation we define some finite dimensional functional spaces with associated Lagrangian basis function; we look for the solution of the approximated problem in these finite dimensional spaces.

The domain Ω_{AC} is discretized following the procedure presented in Section 2.4. So that, we can write:

$$\Omega_{AC} \approx \cup_{K \in \mathcal{T}^h} K \tag{3.10}$$

where K is a tetrahedral volumetric element belonging to the computational mesh $\mathcal{T}^h$.

We adopt a P1/P1 Finite Element discretization, introducing the functional spaces:

$$\begin{aligned}
V^h &= \{\mathbf{v}^h \in [H^1(\Omega_{AC})]^3 : \mathbf{v}^h|_{\Gamma_w} = \mathbf{0},\ \mathbf{v}^h|_{\Gamma_{in}} = \mathbf{u}_{in}^h,\ \mathbf{v}^h|_K \in \mathbb{P}^1(K)\ \forall K \in \mathcal{T}^h\},\\
V_0^h &= \{\mathbf{v}^h \in [H^1(\Omega_{AC})]^3 : \mathbf{v}^h|_{\Gamma_w} = \mathbf{0},\ \mathbf{v}^h|_{\Gamma_{in}} = \mathbf{0},\ \mathbf{v}^h|_K \in \mathbb{P}^1(K)\ \forall K \in \mathcal{T}^h\},\\
Q^h &= \{q^h \in L^2(\Omega_{AC}) : q^h|_K \in \mathbb{P}^1(K)\ \forall K \in \mathcal{T}^h\}
\end{aligned} \tag{3.11}$$

where $\mathbf{u}_{in}^h$ is a suitable approximation of the boundary datum $\mathbf{u}_{in}$ and $\mathbb{P}^1(K)$ represents the space of polynomials of order 1 living on the element K.

The choice of P1/P1 elements does not satisfy the inf-sup condition, thus, in order to avoid the occurrence of spurious pressure modes, we need to add a stabilization term inside the discrete weak formulation of the problem [99]. We chose a SUPG-PSPG stabilization, which allows us to work with inf-sup unstable spaces, while also providing stabilization for possible numerical instabilities arising from the advection-dominated fluid dynamics [100, 101].

We are now ready to introduce the fully-discrete formulation of Problem 3.1. For simplicity, the apex h is understood for all the functions belonging to a finite dimensional space.

Problem 3.2. *Given* ρ, μ, Q_{out} *and* $\boldsymbol{u}_0$, *for* $n = 0, ..., N_t - 1$ *find* $\boldsymbol{u}^{n+1} \in V^h$, $p^{n+1} \in Q^h$

and $\lambda^{n+1} \in \mathbb{R}$ *such that:*

$$\begin{cases} \displaystyle\int_{\Omega_{AC}} \rho \frac{\boldsymbol{u}^{n+1}}{\Delta t} \cdot \boldsymbol{v} + \int_{\Omega_{AC}} \mu \nabla \boldsymbol{u}^{n+1} : \nabla \boldsymbol{v} \\ \quad \displaystyle + \int_{\Omega_{AC}} \rho (\boldsymbol{u}^n \cdot \nabla) \boldsymbol{u}^{n+1} \cdot \boldsymbol{v} - \int_{\Omega_{AC}} p^{n+1} \nabla \cdot \boldsymbol{v} \\ \quad\quad \displaystyle + \int_{\Omega_{AC}} \tau_m(\boldsymbol{u}^n) \boldsymbol{r}_m(\boldsymbol{u}^{n+1}, p^{n+1}) \cdot (\rho \boldsymbol{u}^n \cdot \nabla \boldsymbol{v} + \nabla q) \\ \quad\quad\quad \displaystyle + \int_{\Omega_{AC}} \tau_c(\boldsymbol{u}^n) r_c(\boldsymbol{u}^{n+1}) (\nabla \cdot \boldsymbol{v}) + \lambda^{n+1} \int_{\Gamma_{out}} \boldsymbol{v} \cdot \boldsymbol{n} \\ \quad\quad\quad\quad \displaystyle + \int_{\Omega_{AC}} q \nabla \cdot \boldsymbol{u}^{n+1} = \int_{\Omega_{AC}} \rho \frac{\boldsymbol{u}^n}{\Delta t} \cdot \boldsymbol{v} + \sum_{j=1}^{N_j} \int_{\Gamma^j} \boldsymbol{h}_N^j \cdot \boldsymbol{v} \\ \displaystyle\int_{\Gamma_{out}} \boldsymbol{u}^{n+1} \cdot \boldsymbol{n} = Q_{out} \end{cases} \tag{3.12}$$

for each $v \in V_0^h$ *and* $q \in Q^h$*.*

Where $\mathbf{r}_m(\mathbf{u}^{n+1}, p^{n+1})$ and $r_c(\mathbf{u}^{n+1})$ are the strong residuals of the momentum and continuity (mass conservation) equations, respectively:

$$\begin{aligned} &\mathbf{r}_m(\mathbf{u}^{n+1}, p^{n+1}) = \rho \left(\frac{\mathbf{u}^{n+1}}{\Delta t} + \mathbf{u}^n \cdot \nabla \mathbf{u}^{n+1} \right) + \nabla p^{n+1} - \mu \Delta \mathbf{u}^{n+1} - \rho \frac{\mathbf{u}^n}{\Delta t}, \\ &r_c(\mathbf{u}^{n+1}) = \nabla \cdot \mathbf{u}^{n+1}. \end{aligned} \tag{3.13}$$

Moreover, τ_m and τ_c are the stabilization parameters defined as follows:

$$\begin{aligned} \tau_m(\mathbf{u}^n) &= \left(\frac{\rho^2}{\Delta t^2} + \rho^2 \mathbf{u}^n \cdot \mathbf{G} \mathbf{u}^n + C_r \mu^2 \mathbf{G} : \mathbf{G} \right)^{-\frac{1}{2}}, \\ \tau_c(\mathbf{u}^n) &= \left(\tau_m(\mathbf{u}^n) \mathbf{g} \cdot \mathbf{g} \right)^{-1}, \end{aligned} \tag{3.14}$$

where $\mathbf{G}$ and $\mathbf{g}$ are the metric tensor and the metric vector, respectively, and C_r is a constant obtained by an inverse inequality relation [102].

3.3.3. Algebraic counterpart

Problem 3.2 gives rise to a linear algebraic system of equations that can be solved to obtain an approximated solution of Problem 3.1 at each time step. Being finite dimensional, each discrete functional space admits a finite set of *basis functions*, which we can leverage in order to write the algebraic system.

Note that, for simplicity, in Problem 3.2 we are looking for the solution $\mathbf{u}^{n+1}$ inside a functional space which is different from the space of the test functions $\mathbf{v}$. However, the Finite Element approximation of the original problem works only if the solution lives in the same space as the test functions, therefore we use the *Lifting operator* in order to look for a solution in V_0^h by suitably modifying the discrete weak formulation [99]. We do not enter into details regarding the Lifting operator, but we just consider to look for a solution in the space of test functions V_0^h.

By denoting as $\{\boldsymbol{\varphi}_i\}$ and $\{\psi_j\}$ the basis functions of V_0^h and Q^h respectively, we have:

$$\begin{aligned} \mathbf{v}_h(\mathbf{x},t) &= \sum_{i=1}^{N^h} v_i(t)\boldsymbol{\varphi}_i(\mathbf{x}) \quad \forall \mathbf{v}_h \in V_0^h, \\ q_h(\mathbf{x},t) &= \sum_{j=1}^{M^h} q_j(t)\psi_j(\mathbf{x}) \quad \forall q_h \in Q^h \end{aligned} \tag{3.15}$$

where $N^h = dim(V_0^h) < +\infty$ and $M^h = dim(Q^h) < +\infty$ are the finite dimensions of the two spaces.

Let us denote by $\mathbf{U}^{n+1}$ (resp. $\mathbf{P}^{n+1}$) the components of $\mathbf{u}_h^{n+1}$ (resp. p_h^{n+1}) with respct to the basis $\{\boldsymbol{\varphi}_i\}$ (resp. $\{\psi_j\}$). Then the discrete augmented weak formulation (3.12) gives rise to the following algebraic system of equations:

$$\begin{bmatrix} \mathbb{F}(\mathbf{U}^n) & \mathbb{B}^t & \Phi^t \\ \mathbb{B} & \mathbb{S} & 0 \\ \Phi & 0 & 0 \end{bmatrix} \begin{bmatrix} \mathbf{U}^{n+1} \\ \mathbf{P}^{n+1} \\ \lambda^{n+1} \end{bmatrix} = \begin{bmatrix} \mathbf{G}^{n+1} \\ 0 \\ Q_{out}^{n+1} \end{bmatrix} \tag{3.16}$$

where $\mathbb{F}(\mathbf{U}^n) = \frac{1}{\Delta t}\mathbb{M} + \mathbb{A} + \mathbb{N}(\mathbf{U}^n)$ and $\mathbb{S}$ is a block coming from the stabilization.

In particular, neglecting for simplicity the stabilization terms, we have:

$$\begin{aligned} [\mathbb{M}]_{i,k} &= \rho \int_{\Omega_{AC}} \boldsymbol{\varphi}_k \cdot \boldsymbol{\varphi}_i, && \mathbb{M} \in \mathbb{R}^{N^h \times N^h} \\ [\mathbb{A}]_{i,k} &= \mu \int_{\Omega_{AC}} \nabla\boldsymbol{\varphi}_k : \nabla\boldsymbol{\varphi}_i, && \mathbb{A} \in \mathbb{R}^{N^h \times N^h} \\ [\mathbb{N}(\mathbf{U}^n)]_{i,k} &= \rho \int_{\Omega_{AC}} \left(\sum_{m=1}^{N^h} u_m^n \boldsymbol{\varphi}_m \cdot \nabla \right) \boldsymbol{\varphi}_k \cdot \boldsymbol{\varphi}_i, && \mathbb{N}(\mathbf{U}^n) \in \mathbb{R}^{N^h \times N^h} \\ [\mathbb{B}]_{j,i} &= -\int_{\Omega_{AC}} \psi_j \nabla \cdot \boldsymbol{\varphi}_i, && \mathbb{B} \in \mathbb{R}^{M^h \times N^h} \end{aligned}$$

$$[\Phi]_{1,i} = \int_{\Gamma_{out}} \boldsymbol{\varphi}_i \cdot \mathbf{n}, \qquad \Phi \in \mathbb{R}^{1\times N^h}$$

$$[\mathbf{G}^{n+1}]_i = \left[\frac{1}{\Delta t}\mathbb{M}\mathbf{U}^n\right]_i + \sum_{j=1}^{N_j} \int_{\Gamma_j} \mathbf{h}_N^j(t^{n+1}) \cdot \boldsymbol{\varphi}_i, \qquad \mathbf{G}^{n+1} \in \mathbb{R}^{N^h}.$$

Note that, such matrices have to be suitably modified in order to deal with the Dirichlet boundary conditions on Γ_{in} and Γ_w.

Applying the Lagrange multipliers method for the prescription of a defective flow rate boundary condition gives rise to an augmented algebraic system, which has an extra block with respect to the system arising from a well-posed Navier-Stokes problem. The extra block is associated with the Lagrange multiplier λ and is used to impose the defective condition on the flow rate in a weak sense.

In this work we are interested in solving the algebraic system (3.16) in its monolithic formulation, without resorting to splitting algorithms. Therefore, we cannot rely on black-box available solvers for a NS problem, but we have to implement the augmented algebraic system.

System (3.16) is solved using the preconditioned GMRES algorithm. In particular, we consider the SIMPLE preconditioner in its approximated formulation (aSIMPLE) [103].

3.4. Implementation

In this study we rely on the library $life^x$ (`https://lifex.gitlab.io/`) [104] for all the numerical simulations. $life^x$ is a high-performance Finite Element library mainly focused on mathematical models and numerical methods for cardiac applications; it is written in *C++* and is based on the deal.II Finite Element core [105]. Being programmed following an object oriented approach, the library presents various *C++* classes related to the different physical processes involved in the cardiac function. In this project we consider the class associated with the fluid dynamics of the blood inside the cardiovascular system. This class, called *FluidDynamics*, contains all the methods and utilities needed to solve a generic Navier-Stokes problem following a parallel computing approach.

As previously anticipated, we are interested in solving the algebraic system (3.16) in its monolithic form. Indeed, applying iterative splitting schemes implies multiple resolutions of a NS problem for each time step, which can be particularly expensive from a computational point of view due to the huge number of degrees of freedom arising with patient-specific geometries. However, the augmented algebraic system was not yet implemented inside the *FluidDynamics* class of $life^x$. Thus, we had to modify the class in order to solve the augmented system in case of defective flow rate boundary condition treatment.

On paper, the implementation of the augmented algebraic linear system (3.16) seems straightforward, since we just need to add one row and one column to the system matrix arising from a Navier-Stokes problem and an element to the right end side. Unfortunately, this procedure was not trivial due to the way the degrees of freedom (DoF's) of the algebraic system are handled in a typical deal.II program. In particular, deal.II codes rely on the initialization of a *C++* object, called *DoFHandler*, which is used together with some associated tools to handle the DoF's of a system in a parallel computing framework.

The extra DoF related to the multiplier λ is global, in the sense that it does not depend on the triangulation of the domain. Indeed, λ is only a function of time, thus it is constant over the whole domain at each time instant. However, the *DoFHandler* is not able to deal with a global DoF. Thus, we cannot rely on the DoFHandler and its tools to deal with the multiplier DoF, but we have to manually mimic their action.

As an example, let us consider the process of assigning the ownership of each DoF to a certain processor, which is a necessary step to perform parallel computations. Such operation is performed automatically by the *DoFHandler* for all the DoF's related to the classical NS blocks of the system, so that each DoF is owned by only one processor. To this purpose, the *DoFHandler* initializes a set of indices, called *Locally owned DoF's*, which contains the indices of all the DoF's owned by a certain processor. Since the *DoFHandler* does not take into account the extra DoF, then we need to manually add the index of such DoF to a *Locally owned DoF's* set just for one processor, so that only such processor owns the extra DoF.

The *DoFHandler* and its tools are extensively involved inside the *FluidDynamics* class in procedures as:

- set up of the algebraic system;
- prescription of the boundary conditions;
- assembly of the algebraic system;
- output of the results.

Therefore, particular strategies have to be applied in order to deal with the extra multiplier DoF in all these situations.

Moreover, due to the increased dimension of the algebraic system, a suitable preconditioner has to be designed in order to account for the extra DoF of the system. Since we are interested in solving a NS problem with just one defective flow rate boundary condition, then the resulting algebraic system presents an extra block composed of just one row. For this reason, we chose to extend the aSIMPLE preconditioner, already implemented in $life^x$, by adding a 1×1 identity block on the diagonal extra element. Indeed, this choice is surely not optimal, but the performances of the preconditioner should not be significantly impacted, since the extra block consists in only one row.

In order to validate the implementation of the Lagrange multipliers method inside the *FluidDynamics* class we tested the code in a cylindrical geometry and we analyzed the results obtained using different flow rate patterns. In Section 3.5 we briefly present one simple test, among the ones performed, which highlights the advantages of prescribing defective flow rate boundary condition using this method.

3.5. Numerical results on an idealized geometry

In this Section we present some numerical results obtained from computational fluid dynamics simulations where a defective flow rate boundary condition is treated using the Lagrange multipliers method. In particular, a simple NS problem is solved in a cylindrical domain in order to assess the validity of the implemented numerical methods in an idealized geometry and to highlight the advantages of following a Lagrange multipliers approach for the prescription of a defective condition.

In all the numerical simulations we used the following parameters: $\rho = 1.06$ $[g/cm^3]$ and $\mu = 0.035$ $[dyne \cdot s/cm^2]$. Moreover the Finite Element library $life^x$ (`https://lifex.gitlab.io/`) is used to perform all the simulations.

Let us consider the cylindrical domain Ω_{cyl} with length $l = 5$ $[cm]$ and radius $r = 1$ $[cm]$ shown in Figure 3.2a.

The boundary of Ω_{cyl} can be divided into: Γ_{wall}^{cyl}, which is the lateral surface, or wall, of the cylinder; Γ_{inlet}^{cyl}, which is a cylinder's cross-section used as inlet boundary; Γ_{outlet}^{cyl}, which is the other cross-section used as outlet boundary.

We are interested in solving a Navier-Stokes problem inside the domain Ω_{cyl} (momentum and continuity equations are the same as in (3.1)) supplemented by the following boundary conditions.

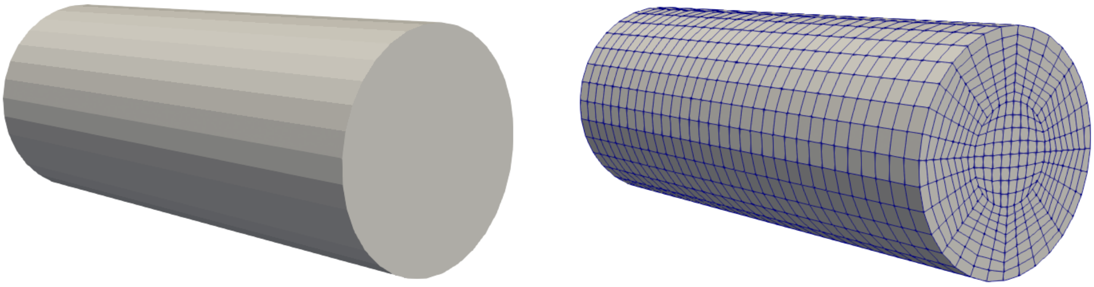
(a) (b)

Figure 3.2: Cylindrical computational domain Ω_{cyl}. The mesh elements are highlighted in Fig. 3.2b

On Γ^{cyl}_{wall} a homogeneous Dirichlet boundary condition, no-slip condition:

$$\mathbf{u} = \mathbf{0}, \text{ on } \Gamma^{cyl}_{wall}. \tag{3.19}$$

Thus the cylinder is still.

On Γ^{cyl}_{inlet} a defective flow rate condition:

$$\int_{\Gamma^{cyl}_{inlet}} \mathbf{u} \cdot \mathbf{n} = Q, \text{ on } \Gamma^{cyl}_{inlet}, \tag{3.20}$$

where Q is an assigned function of time. So that, we are imposing a certain flow rate incoming our domain.

On Γ^{cyl}_{outlet} a homogeneous Neumann condition:

$$-p\mathbf{n} + \mu(\nabla\mathbf{u} + \nabla\mathbf{u}^T)\mathbf{n} = \mathbf{0}, \text{ on } \Gamma^{cyl}_{outlet}. \tag{3.21}$$

Namely, Γ^{cyl}_{outlet} is a stress-free boundary.

Therefore, we want to analyze fluid dynamics inside a fixed cylinder where a time dependent flow rate is prescribed through the inlet cross-section.

For the discretization of the problem we followed an approach based on a Finite Element space discretization and a BDF of order 1 time discretization with semi-implicit treatment of the convective term, analogously to what we have presented Section 3.3. In particular, we work with an hexahedral computational mesh ($h \approx 2.2$ $[mm]$) for the cylindrical domain (Fig. 3.2b), using Q1/Q1 element with a SUPG-PSPG stabilization, while for the time step we chose $\Delta t = 10^{-2}$ $[s]$.

In order to validate the implementation of the Lagrange multipliers method for the prescription of a defective flow rate condition in a Navier-Stokes problem we tested the code for different choices of the inlet flow rate function Q and the computational mesh size. A quantitative validation was given by the computation of the numerical flow rate through the inlet boundary, which in all cases showed an excellent agreement with the prescribed flow rate, moreover qualitative validations were performed with good results. Let us now present some numerical results obtained in the computational mesh shown in Figure 3.2b for a particular choice of Q, so that the advantages of applying the Lagrange multipliers method can be highlighted.

Consider a sinusoidal ramp profile for the assigned flow rate in inlet (Fig. 3.3). At time $t = 0$ $[s]$ the assigned flow rate is equal to 0 $[cm^3/s]$, at $t = 1$ $[s]$ it reaches the maximum value of 3 $[cm^3/s]$, then it remains constant until $T = 10$ $[s]$. So that, the maximum Reynolds number obtained during the simulation is $Re_{max} = \frac{\rho U(2r)}{\mu} = \frac{2\rho Q}{\pi r \mu} \approx 60$ and the flow is laminar.

As a first validation for the implementation of the numerical method, in Figure 3.3 we compare the flow rate through the inlet cross-section Γ^{cyl}_{inlet} computed from the numerical solution with the assigned flow rate Q and we find an excellence agreement between the two. Therefore the implemented Lagrange multipliers method is able to prescribe the defective flow rate condition on the inlet boundary efficiently.

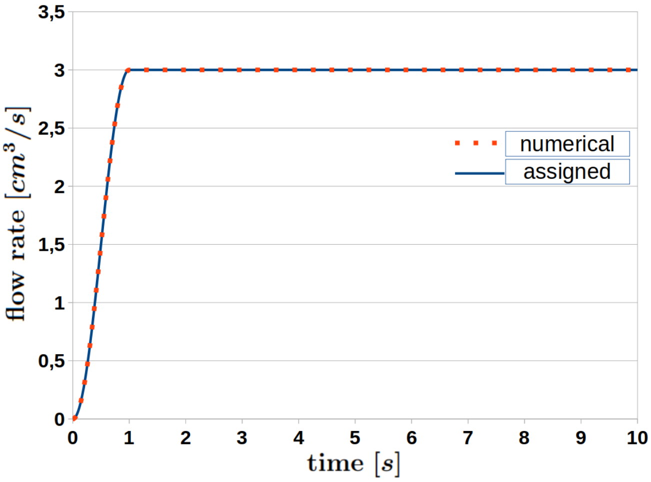

Figure 3.3: Temporal profile of the inlet flow rate Q assigned on the boundary Γ^{cyl}_{inlet} (blue line) together with the inlet flow rate computed from the numerical solution at each time-step (red dots). *CFD cylinder*

In order to highlight the advantages of the Lagrange multipliers method, let us numerically solve the considered problem following two different approaches:

- prescription on the cylinder inlet section of a Dirichlet condition matching the assigned flow rate (we need to fix *a priori* the spatial profile of the velocity field on such section);
- application of the Lagrange multipliers method for defective flow rate condition treatment;

At the final time of $T = 10[s]$ we expect to have a fully-developed laminar stationary flow inside the cylinder, thus the velocity field should present a parabolic spatial profile. So that, we set a parabolic profile for the velocity on the inlet cross-section when working with the Dirichlet condition.

In Figure 3.4 we report the velocity spatial profiles on the inlet and outlet cross-sections of the cylinder at time $t = 1$ $[s]$ (as soon as the assigned flow rate has reached its maximum value) for the numerical solutions obtained following both strategies.

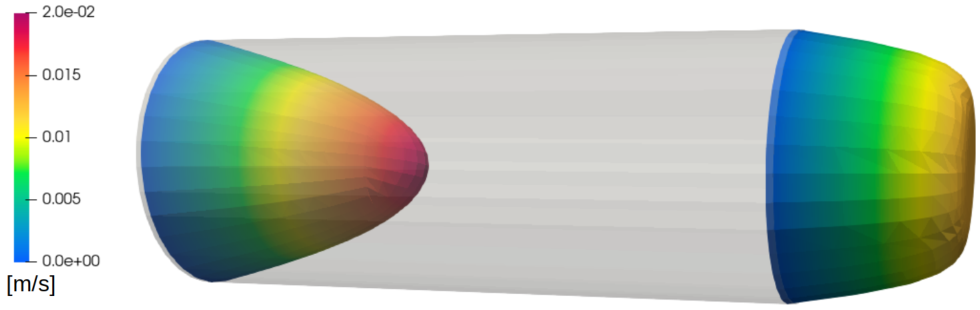

(a) Dirichlet condition in inlet.

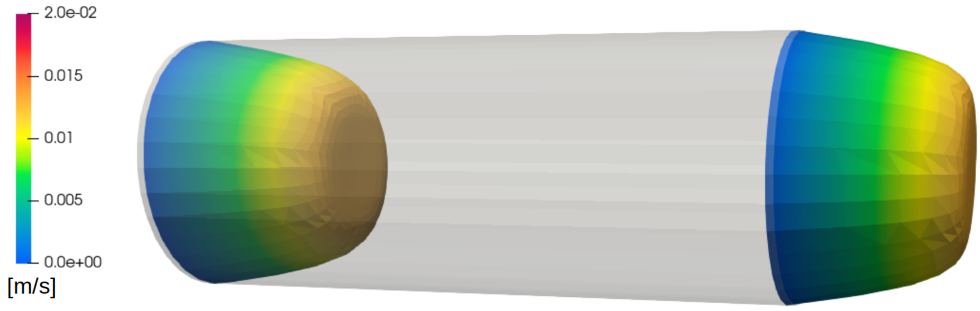

(b) Lagrange multipliers method.

Figure 3.4: Spatial velocity profiles on inlet and outlet cylinder cross-sections for the numerical solutions obtained imposing a Dirichlet condition in inlet (3.4a) and applying the Lagrange multipliers method (3.4b) at $t = 1$ $[s]$. *CFD cylinder*

It is possible to see how fixing *a priori* the spatial profile of the velocity strongly influences the accuracy of the numerical solution in a neighborhood of the boundary where the Dirichlet condition is prescribed. Indeed, following the Dirichlet approach, we are imposing a parabolic profile on the inlet cross-section, even if at this time step the flow did not have time to fully develop, thus the profiles on the inlet and outlet sections differ. While, applying the Lagrange multipliers method, the velocity profile on the inlet section is free to change in time in order to adapt to the problem under study, so that we have the same profile both in inlet and in outlet as we would expect.

Let us now perform the same comparison at time $t = 10$ $[s]$ (Fig. 3.5). In this case the numerical solutions obtained following the different approaches almost coincide. Indeed, the flow is now fully developed, therefore the parabolic spatial profile fixed in inlet using the Dirichlet condition is obtained also on the outlet cross-section. So that, we have a qualitative validation of the implemented method which is able to represent a fully developed steady laminar flow in a cylinder.

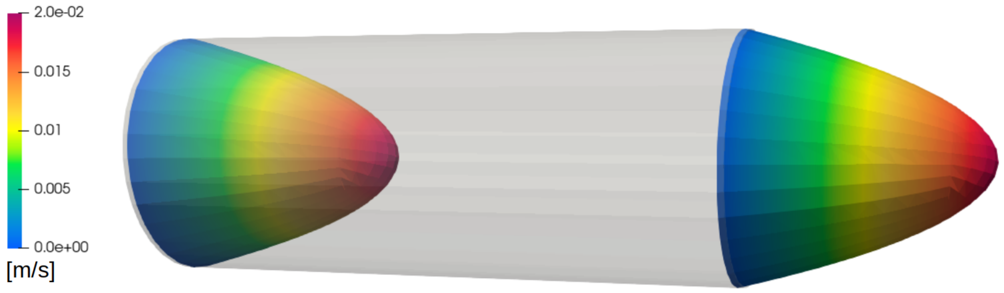

(a) Dirichlet condition in inlet.

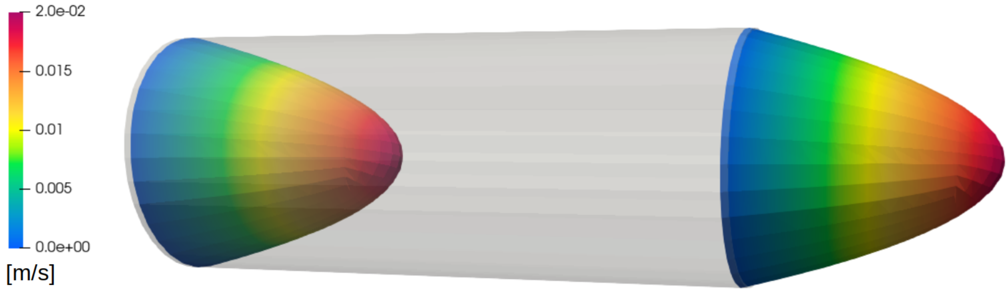

(b) Lagrange multipliers method.

Figure 3.5: Spatial velocity profiles on inlet and outlet cylinder cross-sections for the numerical solutions obtained imposing a Dirichlet condition in inlet (3.5a) and applying the Lagrange multipliers method (3.5b) at $t = 10$ $[s]$. *CFD cylinder*

This simple example highlights the Neumann nature of the implicit boundary condition imposed using the Lagrange multipliers method, which allows the numerical solution to find the best suited spatial profile of the velocity field for the considered problem. So that, using this method we are able to get an accurate numerical solution across the whole domain at each time step, while using a Dirichlet condition the global accuracy can be achieved only in the time steps where the flow is fully developed.

3.6. Application to a patient-specific geometry

In this Section numerical results of computational hemodynamics simulations inside the patient-specific geometry of aortic root and epicardial coronary arteries Ω_{AC} (see Fig. 3.6) are reported to assess the robustness and validity of the presented approach in real geometries. In particular, let us consider the numerical solution of the original Navier-Stokes problem defined by the system of equation (3.1) following the approach presented in Section 3.3, thus solving the augmented NS algebraic system related to the application of the Lagrange multipliers method. From now on we will refer to the computational model for hemodynamics simulation inside aortic root and epicardial coronary arteries as *Standalone CFD model*.

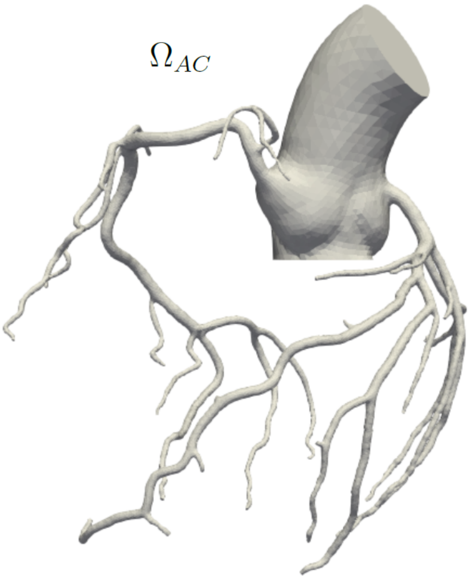

Figure 3.6: Patient-specific geometry of aortic root and epicardial coronary arteries where computational hemodynamics are simulated.

Remember that the entire epicardial coronary artery tree has been reconstructed only for one patient (P1), therefore we study blood dynamics only for such patient. Indeed, analyzing the flow partition between left and right coronary branch for the other patients would be meaningless due to the missing branches inside the right coronary tree. In particular, patient P1 is a healthy patient (no coronary arteries stenosis), which allows us to apply the model in a realistic physiological case.

In all the numerical simulations we used the following parameters: $\rho = 1.06$ $[g/cm^3]$ and $\mu = 0.035$ $[dyne \cdot s/cm^2]$. Moreover the Finite Element library $life^x$ (`https://lifex.gitlab.io/`) is used to perform all the simulations.

We aim at numerically simulating hemodynamics in Ω_{AC} for a whole heartbeat. To this purpose, we exploit the heartbeat measures performed by clinicians on this patient in rest conditions, since for the moment we are interested in reproducing physiological conditions. In particular, they found that the patient-specific resting heart beat is 65 bpm resulting in a heartbeat period of around 0.923 $[s]$. Therefore, we set $T = 0.923$ $[s]$ as the final time for the numerical simulation.

As already mentioned, the continuous problem has been discretized following the approach presented in Section 3.3. In particular the volumetric computational mesh of Ω_{AC} for patient P1 has a maximum mesh size $h_{max} \approx 5$ $[mm]$, in the ascending aorta, and minimum mesh size $h_{min} \approx 0.18$ $[mm]$, in the smallest coronary vessels. Moreover, we used as time step $\Delta t = 10^{-3}$ $[s]$.

Regarding boundary conditions:

- Using a defective flow rate condition with the Lagrange multipliers method, we imposed on the aortic outlet Γ_{out} a physiological flow rate (Fig. 3.7a) taken from patient-specific PC-MRI images in [106] and accordingly scaled as explained below.

- On the aortic inlet Γ_{in} we prescribed a Dirichlet condition, fixing a flat spatial profile for the velocity in inlet. In order to guarantee that the total flow entering inside the coronary circulation is physiological, we set the flow rate on the aortic inlet to be equal to the sum of the flow rate on the aortic outlet (Fig. 3.7a) and the expected flow rate inside the coronaries (Fig. 3.7b). For the temporal profile of the flow rate in the coronaries we exploited some blood flow measurement inside the Left Anterior Descending (LAD) coronary branch used in [107] and we translated upward the profile in order to avoid a negative total flow rate in early systole. Indeed, the reverse flow is often visible inside the left coronary branch, but not in the right one, where flow rate is always greater than zero during an heartbeat [5]. Moreover, the flow rate profiles have been scaled in such a way that: the average flow rate on the aortic inlet is 5.1 $[L/min]$, since the cardiac output in physiological conditions is $\sim 5-6$ $[L/min]$ [108]; the flow entering the coronary circulation during an heartbeat is around 5% of the total flow coming into the aorta, since coronary blood flow is 5% of the cardiac output in rest conditions [12, 109].

- On the coronary outlet sections Γ^j we prescribe Neumann conditions, basically fixing a value for the pressure field on those outlet boundaries. This is done in order to get physiological pressure values across the domain during the whole heartbeat. We prescribed the same temporal profile (Fig. 3.7c) for the pressure value on all the coronary outlet boundaries. Such profile was obtained from the classical pressure waveform in the aorta, since, in physiological cases, the pressure inside the epicardial coronary arteries roughly follows the same temporal profile as in the aorta, as suggested by [8, 35].

Each temporal profile has been scaled in time in order to match the period of the patient-specific heartbeat.

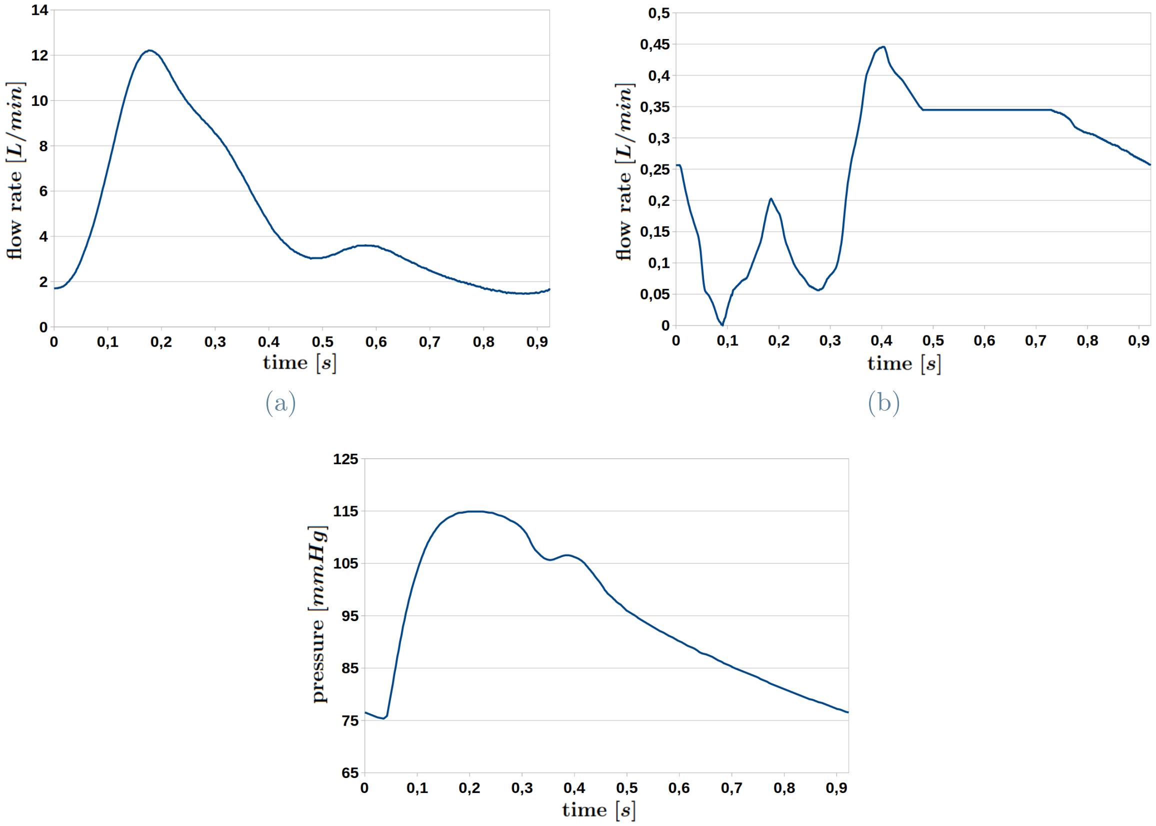

(a) (b)

(c)

Figure 3.7: Temporal profiles used to prescribe boundary conditions: (a) assigned flow rate on aortic outlet boundary [106]; (b) expected total flow rate in coronary circulation [107]; (c) assigned pressure waveform on coronary outlet sections. *Standalone CFD model*

Note that the expected flow rate in the coronaries presents a phasic pattern, being significantly greater during diastole, this is done to represent the increase flow resistance during systole, caused by the myocardial contraction, which, again, is not captured otherwise by the model.

In this section we aim at showing that using the set up just presented we are able to obtain physiologically coherent numerical results in terms of pressure distribution across the domain and flow partition between left and right coronary branches. Moreover, we analyze the flow partition also in a different scenario in order to evaluate the impact of a change in boundary conditions on this feature. In particular, different pressure boundary conditions are prescribed on the outlet sections of the coronary arteries perfusing the left and right heart in the alternative scenario .

3.6.1. Base scenario: physiological consistency

Analogously to what we did for the test in the cylinder, in Figure 3.8a we show that, using the implemented Lagrange multipliers method for the prescription of the defective flow rate condition on the aortic outlet boundary, the flow rate computed from the numerical solution is in excellent agreement with the assigned flow rate. This validates the implementation of such method also in the case of real geometries, proving its robustness.

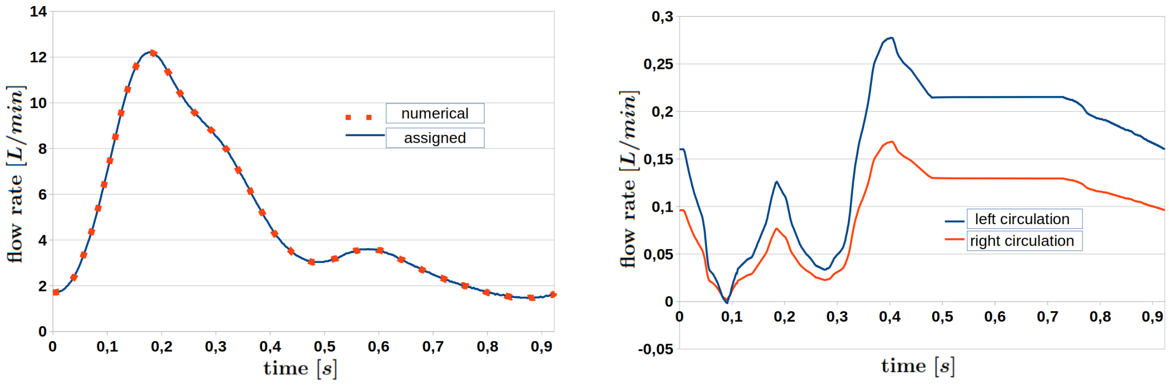

(a)

(b)

Figure 3.8: (a) Comparison between the flow rate through the aortic outlet section computed from the numerical solution and the assigned flow rate through the same section. (b) Numerical flow rate inside left (blue) and right (red) coronary circulations. *Standalone CFD model*

Let us now analyze how the blood flow entering inside the coronary circulation distributes between the left and right coronary branches. To this purpose, in Figure 3.8b we report the numerical flow rate inside each branch.

In this simulation we are imposing a physiological flow rate inside the aorta, while guaranteeing that the total flow entering inside the coronary circulation is the one depicted in Figure 3.7b. Therefore, we are not manually setting the amount of blood flow incoming the left or right coronary circulations, but the numerical solution presents a certain flow partition depending on the geometry of the coronary arteries and the boundary conditions imposed on the coronary outlets. In this case, we are prescribing the same pressure values on both the left and right coronary outlet sections, thus assuming to have the same pressure drop from the aortic root to the outlet sections of each circulation. Under this assumption, the numerical results show a greater amount of blood flow inside the left coronary circulation, as we would expect [5, 12].

During diastole it makes sense to assume to have the same pressure on the right and left coronary outlet boundaries. Indeed, in this period there is no compression of the intramural vessels, thus blood flow mostly depends on the pressure gradient between the aorta and the coronary veins, which is almost independent of the coronary branch, in physiological conditions. Therefore, our simulation suggests that during diastole the geometrical features of the coronary branches (e.g. luminal volume) are enough to explain a greater blood flow inside the left coronary circulation.

On the other hand, during systole the compression of the intramural coronary vessels is more significant inside the left heart due to the higher pressures needed to pump blood in the whole systemic circulation [12]. For the moment we are not describing such higher resistance in our model, but this can be done by modifying the pressure values at the coronary outlets, as will be shown later.

Since we are solving 3D NS equations inside our domain, then we have a local description of both the pressure and velocity field, as shown in Figure 3.9, where the pressure distribution and the streamlines of the velocity field are reported for different time instants across the whole domain. For each time instant we also reported two small charts representing the flow rate inside the coronary circulation (Fig. 3.7b) and inside the aorta (Fig. 3.7a) together with a red dot indicating the position of such time instant on the temporal profiles.

The numerical results reported in Figure 3.9 show that for each considered time instant we get physiological pressure values across the domain. In particular: during early systole (Fig. 3.9a) the pressure is rapidly increasing, thus in the aortic root is ~ 98 $[mmHg]$; at the systolic peak (Fig. 3.9b) the pressure reached its maximum value of ~ 120 $[mmHg]$; during early diastole (Fig. 3.9c) the pressure starts decreasing, but for the selected time instant is still high, it takes values between $\sim 105 - 115$ $[mmHg]$; in mid-late diastole (Fig. 3.9d) the pressure had time to decrease, so that we have pressure values in the range $\sim 85 - 90$ $[mmHg]$ across the domain. Moreover, for both time instants during systole, Figure 3.9 shows regular velocity streamlines inside the aortic root and small velocity magnitude inside the coronaries, as we expected; whereas during diastole, thanks to its 3D description, the numerical model is able to capture secondary flows and recirculation areas inside the aortic root, leading to more chaotic velocity streamlines.

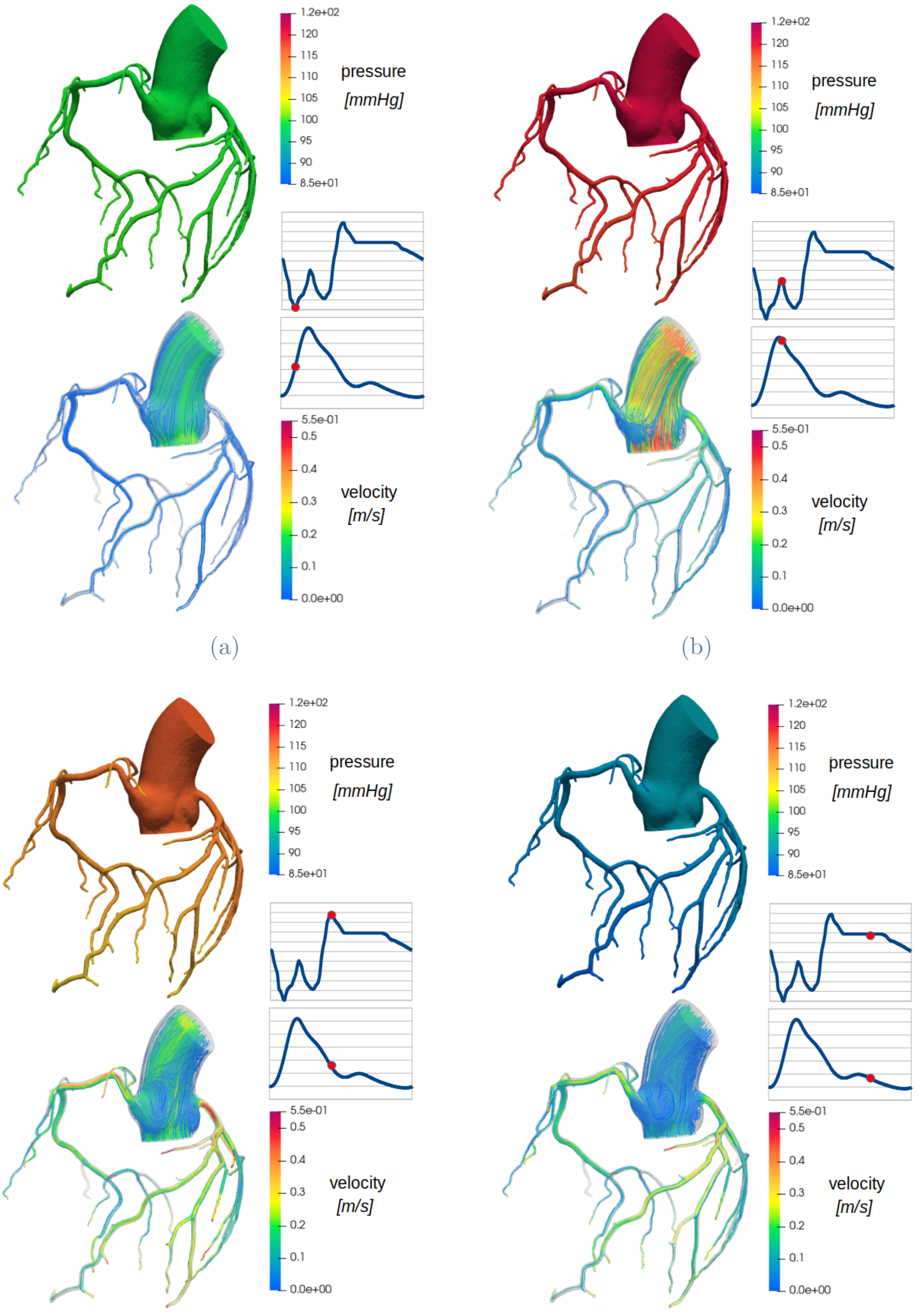

(a) (b)

(c) (d)

Figure 3.9: Numerical pressure and velocity streamlines across the domain for different time instants: (a) $t = 0.09$ $[s]$, minimum CBF in systole; (b) $t = 0.18$ $[s]$, peak aortic flow rate in systole; (c) $t = 0.4$ $[s]$, peak CBF in early diastole (d) $t = 0.7$ $[s]$, mid-late diastole. *Standalone CFD model*

Notice that, the velocity magnitude on the aortic outlet assumes physiological values [110], while inside the aortic sinus is underestimated during systole of about $30-40\%$. Indeed, the flow rate on the aortic inlet should be represented by an on-off signal, active only during systole (when the aortic valve is open), resulting in a greater value for the peak systolic flow rate, thus a greater peak systolic velocity. However, since we are not considering the compliance of the vessel, we are not able to impose both an on-off flow rate on the aortic inlet and the smoothed profile represented in Figure 3.7a on the aortic outlet. Therefore, in this first study we accept the under estimation of the velocity inside the sinus of Valsalva since it allows us to obtain a physiological cardiac output in terms of average flow rate (5.1 $[L/min]$), a physiological flow rate inside the coronary circulation (Fig. 3.7b) and accurate numerical solutions in the ascending aorta. In order to get more physiologically consistent peak systolic velocity values inside the sinus of Valsalva different choices for the boundary conditions imposed on the aortic cross-sections can be investigated in future studies.

Let us now perform an analysis of the spatial pressure gradient in the domain. To this purpose, in Figure 3.10 we report the pressure distribution for two different time instants, corresponding to the minimum and maximum value of CBF during the heartbeat. Again we also report the temporal profile of the flow rate inside the coronaries together with a red dot indicating the location of the time instant on the profile.

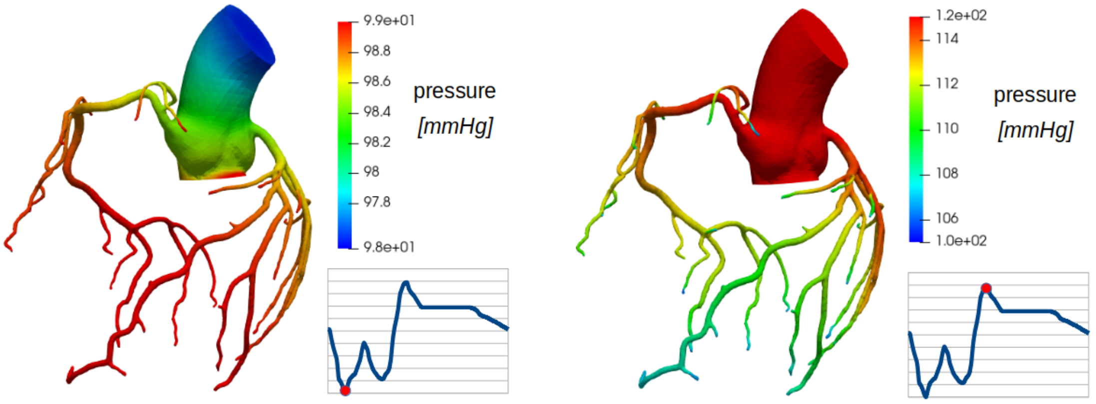

(a) (b)

Figure 3.10: Numerical pressure gradients for different time instants: (a) $t = 0.09$ $[s]$, minimum CBF in systole; (b) $t = 0.4$ $[s]$, peak CBF in early diastole. Note that the reference scales change between picture (a) and (b). *Standalone CFD model*

Figure 3.10a shows a significant pressure gradient between the inlet and outlet sections of the aortic root due to the acceleration of the flow inside the aorta, whereas the higher pressure inside the coronaries with respect to the aortic root does not allow flow to enter the coronary circulation. On the other hand, in Figure 3.10b there is a positive pressure gradient between aortic root and coronary arteries, since the flow inside coronaries is maximum for this instant

Therefore, this computational model for blood dynamics simulations inside the aortic root and epicardial coronary arteries is able to provide physiologically consistent numerical results in a patient-specific reconstructed anatomical geometry.

Thanks to the 3D description that our model provides, in future studies it can be applied to compute the Wall Shear Stress (WSS) across the whole domain, also in the coronary sinuses, which was not possible without the inclusion of the aorta in the computational domain. Moreover, if used in pathological cases, our model allows to capture the pressure drop due to the presence of a stenosis, which is of utmost importance for the computational evaluation of the Fractional Flow Reserve (FFR), as proposed by Taylor et al. in [23]. FFR represents the ratio between the maximal coronary blood flow through a stenotic artery and the blood flow in the hypothetical case that the artery was normal and is used in clinical practice in order to perform a functional assessment of a coronary artery stenosis. Further improvements on the computational model can be made by coupling it with reduced order model (e.g. lumped parameters, 1D models) in order to obtain more physiologically consistent boundary conditions.

3.6.2. Alternative scenario: different pressure conditions for left and right heart

As already mentioned, during systole the compression of the intramural vessels is more significant inside the left heart, due to the high pressure values needed to pump blood into the systemic circulation [12]. In order to capture such feature, we prescribed different pressure boundary conditions on the coronary outlet sections perfusing the left and right heart. The identification of the branches perfusing each side of the heart was done using the server Paraview and was consistent with the work of Di Gregorio during his PhD [71]. The enforced strategy consisted on defining a pressure difference between left and right heart, such pressure difference increases linearly in early systole, reaching the maximum value of 2 $[mmHg]$ in the instant of minimum CBF, then decreases to zero during the remaining systolic period.

In Figure 3.11 there is a comparison between the flow rates inside the left and right coronary branches obtained following the two presented strategies, namely:

- prescribing same pressure boundary conditions on each coronary outlet section, regardless of the perfusion region related to the coronary branch (Fig. 3.11a);

- accounting for an higher pressure value during systole for those coronary branches perfusing the left heart (Fig. 3.11b).

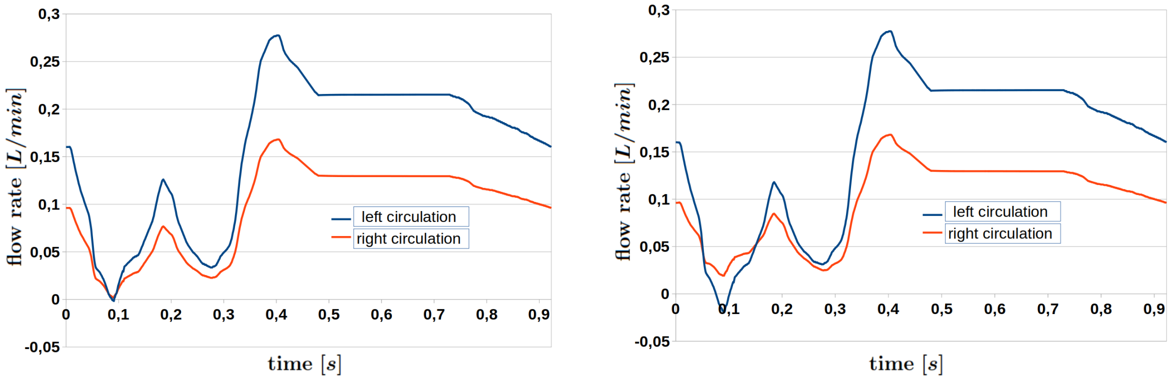

(a)

(b)

Figure 3.11: Flow rates in left and right coronary branches following two strategies: (a) same pressure boundary conditions for left and right heart; (b) account for a pressure correction in left heart during systole. *Standalone CFD model*

Following the first strategy the flow rate inside each coronary branch follows the temporal profile in Figure 3.7b, in particular both the left and right profile almost reaches the value of 0 [L/min] in early systole. On the other hand, accounting for a pressure correction in the left heart, the model is able to describe retrograde flow in the left coronary branch while the flow rate remains positive in the right branch for the whole heartbeat. Thus, the second strategy qualitatively provides more physiologically consistent numerical results in terms of flow partition between left and right coronary circulations.

Such alternative approach highlights the flexibility of this computational model for hemodynamics inside aortic root and epicardial coronary arteries. Indeed, one can easily study different scenarios in order to understand what are the features of the model having the biggest impact on flow partition, pressure distribution and velocity field description.

3.7. Final remarks

Novelty of this work:

- this is not the first occurrence of a computational model for hemodynamics simulations applied inside patient-specific aortic root and epicardial coronary arteries geometries and based on the 3D formulation of the Navier-Stokes equations (e.g. [23]). However, to the best of our knowledge, such modeling framework has never been combined with the treatment of defective flow rate boundary conditions exploiting the Lagrange multipliers method.

Take home messages:

- the implemented Lagrange multipliers method has proven to effectively prescribe defective flow rate conditions for a NS problem both in an idealized geometry and in patient-specific geometries, highlighting its accuracy and robustness;
- using the presented standalone CFD model we are able to obtain physiologically consistent numerical results inside real geometries in terms of flow partition between left and right coronary tree, velocity streamlines and pressure distribution. The only limitation concerns the velocity magnitude inside the aortic sinus, which is under estimated due to the rigid wall assumption;
- the flexibility provided by the standalone CFD model allows us to study different scenarios in a practical way;
- by considering physiologically meaningful modifications of the model, such as accounting for higher pressure in the left heart during systole, we managed to obtain even more accurate numerical results. Thus, the standalone CFD model has room for improvement, specially concerning boundary conditions.

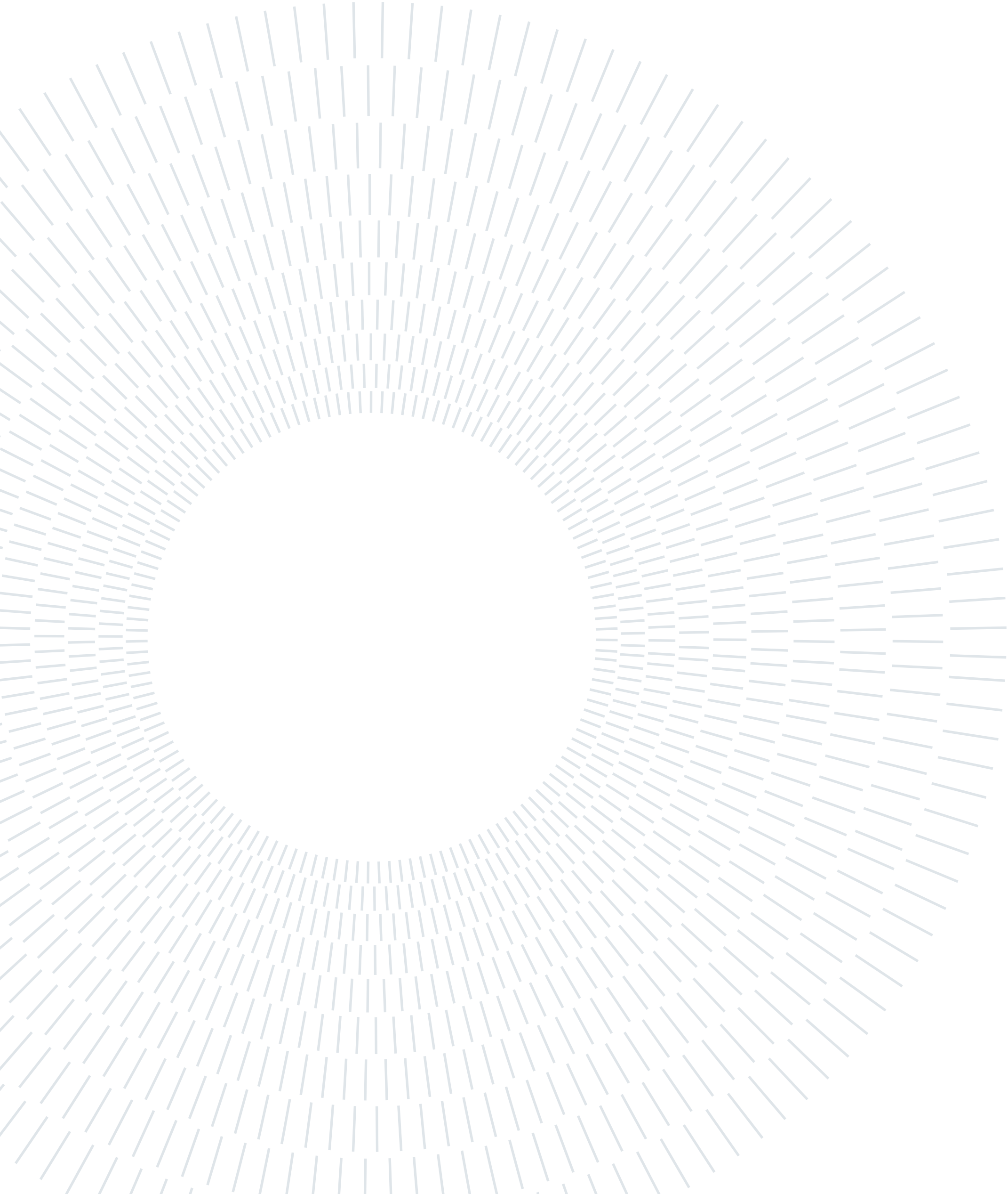

4 | Computational multi-physics coupled model for myocardial perfusion

In Chapter 3 we considered blood dynamics inside the aortic root and epicardial coronary arteries as a standalone problem, introducing the regulating equations (Navier-Stokes equations), their numerical approximation and some numerical results. In this chapter we couple such problem with hemodynamics inside the intramural coronary vessels, which are described by a different set of equations (multi-compartment Darcy model) due to the different characteristic lengths of the vessels, thus giving rise to a multi-physics coupled mathematical and numerical model, analogously to what was proposed in [69].

The novelty of this study with respect to the model proposed in [69] is the inclusion of the aorta inside the computational domain where 3D Navier-Stokes equations are solved. Thus, the mathematical formulation of the coupled model has to be modified accordingly.

This chapter is structured as follows:

- In Section 4.1 the regulating equations of blood dynamics inside the intramural vessels are presented. In particular the strong formulation (Sect. 4.1.1), weak formulation (Sect. 4.1.2) and numerical approximation (Sect. 4.1.3) of the considered multi-compartment Darcy model are reported.

- In Section 4.2 we provide an overview of the multi-physics coupled model, which comprises: the coupling conditions (Sect. 4.2.1), the mathematical formulation of the coupled model (Sect. 4.2.2) and the model's parameters estimate (Sect. 4.2.3).

- In Section 4.3 we describe the numerical approximation of the coupled model. First focusing on its temporal discretization and introducing an iterative splitting strategy for its numerical solution (Sect. 4.3.1), then completing the description with the spatial discretization and associated algebraic formulation (Sect. 4.3.2).

4.1. Hemodynamics in the intramural coronary vessels

The intramural coronary vascular network could not be reconstructed from the available cCTA images due to small dimension of its vessels and the presence of the surrounding tissue. Thus, as explained in Section 2.3.1, the whole myocardial volume of the left ventricle was reconstructed in [70] for each patient in their study population. An explicit description of the patient-specific intramural network is therefore unfeasible due to lack of data, moreover it would be too computationally expensive to explicitly simulate blood dynamics inside such network due to huge amount of vessel composing it (Sect. 1.3.1).

For this reasons, in this work we consider a multi-compartment Darcy modeling of the left ventricle, having three compartments related to the different length scales of the intramural network (arteries, arterioles and capillaries), since in [62] a 3-compartment model was found to be preferable with respect to a 2-compartment model. As mentioned in Section 1.4.3, such modeling approach consists in the subdivision of the intramural vessels into different levels (or compartments), each of them modelled through a porous medium, which coexist in the same computational domain, the myocardium (Fig. 4.1).

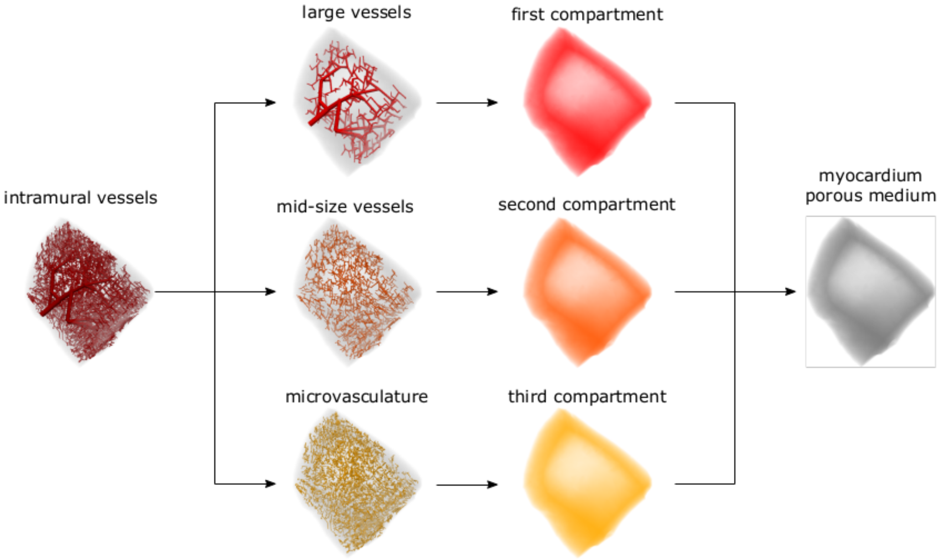

Figure 4.1: Schematic overview of the 3-compartment porous medium in a piece of myocardium: the intramural vessels are sub-divided in three groups, each group will characterize a different compartment. The three compartments co-exist in the myocardium. [71]

The multi-compartment Darcy model was proposed and analyzed in a computational framework in [59, 60, 62].

4.1.1. Multi-compartment Darcy model

The multi-compartment Darcy model consists in the solution of Darcy equations inside each compartment, providing a description of the blood flow associated to each considered length scales. As already mentioned, the three compartments live in the same domain, the myocardium, which we denote as Ω_M.

The Darcy equations solved in each compartment $i \in [1, 3]$ read:

$$\mathbf{K}_i^{-1}\mathbf{u}_{M,i} + \nabla p_{M,i} = \mathbf{0} \qquad \text{in } \Omega_M, \tag{4.1a}$$

$$\nabla \cdot \mathbf{u}_{M,i} = g_i - \sum_{k=1,k\neq i}^{3} \beta_{i,k}(p_{M,i} - p_{M,k}) \qquad \text{in } \Omega_M, \tag{4.1b}$$

$$\mathbf{u}_{M,i} \cdot \mathbf{n} = 0 \qquad \text{on } \partial\Omega_M, \tag{4.1c}$$

where, for each compartment $i = 1, 2, 3$, $\mathbf{u}_{M,i}$ and $p_{M,i}$ are the Darcy velocity and pore pressure, respectively, $\mathbf{K}_i$ is the permeability tensor, g_i is a volumetric source (or sink) term and $\beta_{i,k}$, $k = 1, 2, 3$ $k \neq i$, are the inter-compartment pressure-coupling coefficients. The parameters $\mathbf{K}_i$ and $\beta_{i,k}$ have to be estimated, we will give an overview of the estimation strategies in Section 4.2.3.

Mass conservation is enforced by compensating the divergence of the Darcy velocity in each compartment with a source, or sink, external term (g_i) and mass exchanges between the different compartments ($\beta_{i,k}(p_{M,i} - p_{M,k})$). In particular, only adjacent compartments can exchange mass, so that $\beta_{1,3} = \beta_{3,1} = 0$. Moreover, the intermediate compartment cannot communicate with the external environment, thus $g_2 = 0$. In order to correctly impose mass conservation, some compatibility conditions have to be satisfied:

$$\beta_{i,k} = \beta_{k,i} \quad \forall i, k \in [1, 3],\ i \neq k, \tag{4.2a}$$

$$\int_{\Omega_M} (g_1 + g_3) d\mathbf{x} = 0, \tag{4.2b}$$

where condition (4.2b) is due to the null flux conditions on the epicardial and endocardial surfaces $\partial\Omega_M$ (4.1c).

The system of equations (4.1) is called mixed formulation of the multi-compartment Darcy model. We can pass to the primal Darcy formulation by substituting equation (4.1a) in

(4.1b), thus eliminating the Darcy velocity and writing the equations only for the pressure variable $p_{M,i}$. The resulting system of equations reads:

$$-\nabla \cdot (\mathbf{K}_i \nabla p_{M,i}) = g_i - \sum_{k=1,k\neq i}^{3} \beta_{i,k}(p_{M,i} - p_{M,k}) \qquad \text{in } \Omega_M, \tag{4.3a}$$

$$(-\mathbf{K}_i \nabla p_{M,i}) \cdot \mathbf{n} = 0 \qquad \text{on } \partial\Omega_M. \tag{4.3b}$$

The Darcy velocity can be obtained through a post-processing of the pressure computed in (4.3), namely:

$$\mathbf{u}_{M,i} = -\mathbf{K}_i \nabla p_{M,i} \qquad \text{in } \Omega_M. \tag{4.4}$$

Thanks to the elimination of the Darcy velocity, the algebraic system related to the numerical approximation of the primal formulation presents a small number of degrees of freedom. Thus, numerically solving the primal formulation is easier and faster than solving the original mixed formulation. However, a loss of accuracy is entailed in the computation of the velocity (4.4). Since we do not exploit the velocity in order to numerically compute MBF inside the myocardium, then the primal formulation is used in this work. Therefore, from now on we will consider only the primal formulation of the three-compartment Darcy model under consideration.

Let us now focus for a moment on the source (or sink) external terms g_i. The first compartment is the most proximal to the epicardial coronary arteries, therefore g_1 is related to the blood dynamics inside such large arteries (Sect. 4.2.1). As already mentioned, the second compartment does not exchange mass with the external environment, thus $g_2 = 0$. Finally, the third compartment is related to the microvasculature, therefore we need a sink term accounting for the venous return, namely:

$$g_3 = -\gamma(p_{M,3} - p_{veins}), \tag{4.5}$$

where p_{veins} is the venous pressure and γ a suitable draining coefficient.

We are now ready to write the complete 3-compartment Darcy model for blood dynamics inside the myocardium in its primal formulation.

Problem 4.1 (Three-compartment Darcy strong primal formulation). *Given* g_1, $\beta_{1,2} =$

$\beta_{2,1}$, $\beta_{2,3} = \beta_{3,2}$, $\boldsymbol{K}_i$, γ and p_{veins}, find $p_{M,i}$, $i = 1,2,3$, such that:

$$\begin{cases} -\nabla \cdot (\boldsymbol{K}_1 \nabla p_{M,1}) = g_1 - \beta_{1,2}(p_{M,1} - p_{M,2}) & \text{in } \Omega_M, \\ -\nabla \cdot (\boldsymbol{K}_2 \nabla p_{M,2}) = -\beta_{2,1}(p_{M,2} - p_{M,1}) - \beta_{2,3}(p_{M,2} - p_{M,3}) & \text{in } \Omega_M, \\ -\nabla \cdot (\boldsymbol{K}_3 \nabla p_{M,3}) = -\gamma(p_{M,3} - p_{veins}) - \beta_{3,2}(p_{M,3} - p_{M,2}) & \text{in } \Omega_M. \end{cases} \tag{4.6}$$

Supplemented with the boundary conditions (4.3b)*, $i = 1,2,3$.*

4.1.2. Weak formulation

Let us define the trial space for the pressure field:

$$Q = L^2(\Omega_M). \tag{4.7}$$

The weak formulation of Problem 4.1 reads:

Problem 4.2 (Three-compartment Darcy weak primal formulation)**.** *Given g_1, $\beta_{1,2} = \beta_{2,1}$, $\beta_{2,3} = \beta_{3,2}$, $\boldsymbol{K}_i$, γ and p_{veins}, find $p_{M,i} \in Q$, $i = 1,2,3$, such that:*

$$\begin{cases} \int_{\Omega_M} (\boldsymbol{K}_1 \nabla p_{M,1}) \cdot \nabla q_M = \int_{\Omega_M} g_1 q_M - \beta_{1,2} \int_{\Omega_M} (p_{M,1} - p_{M,2}) q_M, \\ \int_{\Omega_M} (\boldsymbol{K}_2 \nabla p_{M,2}) \cdot \nabla q_M = -\beta_{2,1} \int_{\Omega_M} (p_{M,2} - p_{M,1}) q_M - \beta_{2,3} \int_{\Omega_M} (p_{M,2} - p_{M,3}) q_M, \\ \int_{\Omega_M} (\boldsymbol{K}_3 \nabla p_{M,3}) \cdot \nabla q_M = -\gamma \int_{\Omega_M} (p_{M,3} - p_{veins}) q_M - \beta_{3,2} \int_{\Omega_M} (p_{M,3} - p_{M,2}) q_M \end{cases} \tag{4.8}$$

for each test function $q_M \in Q$.

4.1.3. Numerical approximation

Analogously to what was done for the Navier-Stokes problem in Section 3.3, we followed a standard Galerkin approach for the spatial discretization of Problem 4.2 based on the Finite Element method. Let us denote with $\mathcal{T}^h$ a regular triangulation of the myocardial domain Ω_M made of hexahedral element Ω_K:

$$\Omega_M = \bigcup_{\Omega_K \in \mathcal{T}^h} \Omega_K.$$

Exploiting the triangulation of the domain we can introduce the polynomial finite dimensional space where we look for an approximated solution of the problem:

$$Q^h = \left\{ q_h \in L^2(\Omega_M) : q_h|_{\Omega_K} \in \mathbb{Q}^1(\Omega_K) \ \forall \Omega_K \in \mathcal{T}^h \right\} \subseteq Q, \tag{4.9}$$

where $\mathbb{Q}^1(\Omega_K)$ is the space of tensor-product of polynomials of global degree ≤ 1 inside each hexahedral element Ω_K.

We do not report here the discrete weak formulation of the problem since it is equivalent to formulation 4.8, just taking all the trial and test function inside the space Q^h instead of Q.

Thanks to the finite dimension of the space Q^h, every function $q_h \in Q^h$ can be written as a linear combination of the basis functions for such space. In particular, if we denote as $\{\psi_j\}_{j=1}^{M^h}$, the set of basis function of Q^h, then all the unknowns of the Galerkin problem can be written in terms of such basis functions, namely:

$$p_{M,i}^h(\mathbf{x}) = \sum_{j=1}^{M^h} p_{M,i}^j \psi_j(\mathbf{x}), \qquad i = 1, 2, 3, \tag{4.10}$$

where $M^h = dim(Q^h) < +\infty$ is the finite dimension of the space Q^h.

By denoting as $\mathbf{P}_{M,i}$ the vector made of the components of $p_{M,i}^h$ with respect to the basis functions $\{\psi_j\}$, the Finite Element approximation of Problem 4.2 gives rise to the following algbraic linear system:

$$\begin{bmatrix} \mathbb{D}_1 + \mathbb{C}_{12} & -\mathbb{C}_{12} & 0 \\ -\mathbb{C}_{21} & \mathbb{D}_2 + \mathbb{C}_{21} + \mathbb{C}_{23} & -\mathbb{C}_{23} \\ 0 & -\mathbb{C}_{23} & \mathbb{D}_3 + \mathbb{C}_{32} + \mathbb{C}_\gamma \end{bmatrix} \begin{bmatrix} \mathbf{P}_{M,1} \\ \mathbf{P}_{M,2} \\ \mathbf{P}_{M,3} \end{bmatrix} = \begin{bmatrix} \mathbf{G}_1 \\ 0 \\ \mathbf{G}_3 \end{bmatrix}, \tag{4.11}$$

where, for each compartment $i = 1, 2, 3$, $\mathbf{G}_i$ is the vector accounting for the external source term.

In particular, the sub-matrices involved inside system (4.11) are defined as:

$$[\mathbb{D}_i]_{l,j} := \int_{\Omega_M} (\mathbf{K}_i \nabla \psi_j) \cdot \nabla \psi_l \qquad \mathbb{D}_i \in \mathbb{R}^{M^h \times M^h}$$

$$[\mathbb{C}_{ik}]_{l,m} := \int_{\Omega_M} \beta_{i,k} \psi_m \psi_l \qquad \mathbb{C}_{ik} \in \mathbb{R}^{M^h \times M^h}$$

$$[\mathbb{C}_\gamma]_{l,m} := \int_{\Omega_M} \gamma \psi_m \psi_l \qquad \mathbb{C}_\gamma \in \mathbb{R}^{M^h \times M^h}$$

$$[\mathbf{G}_3]_l := \int_{\Omega_M} \gamma p_{veins} \psi_l \qquad \mathbf{G}_3 \in \mathbb{R}^{M^h}$$

4.2. Multi-physics coupled mathematical model

In this work we are interested in numerically simulating myocardial perfusion by coupling the 3D description of blood dynamics inside the aortic root and epicardial coronary arteries (Chapter 3) with the multi-compartment Darcy model for the intramural vessels (Sect. 4.1), exploiting the mathematical model proposed in [69]. To this purpose, a suitable set of coupling conditions has to be introduced in order to guarantee the continuity of momentum and mass between the two problems. Then, the complete mathematical formulation of the model is reported and the techniques enforced to estimate the model parameters are discussed.

Such multi-physics modeling approach was chosen due to the separation of scale in the coronary circulation (Sect. 1.2.1), which makes it unfeasible to apply the same model for hemodynamics inside both the large epicardial arteries and the small intramural vessels.

4.2.1. Coupling conditions

Two coupling conditions, one for the conservation of mass and the other one for the balance of interface forces [111], are needed in order to couple the 3D Navier-Stokes problem inside aortic root and epicardial coronary arteries with the multi-compartment Darcy problem inside the myocardium.

Remember that, as mentioned in Section 1.2.1, the myocardium can be divided into perfusion regions, each of them perfused by a particular epicardial coronary artery. Therefore, by denoting with Ω_M^j each perfusion region ($\Omega_M = \cup_j \Omega_M^j$), we have a one to one correspondence between the epicardial coronary outlet sections Γ^j (see Sect. 3.1) and the perfusion regions Ω_M^j. In particular, the two problems can exchange information only between the coronary outlet section Γ^j and the correspondent perfusion region Ω_M^j, $j = 1, ..., N^j$. The enforced strategies to subdivide the patient-specific left ventricles into perfusion regions will be explained in Section 4.2.3.

Note that the Neumann conditions imposed on each Γ^j in (3.1) (Sect. 3.1) are now substituted by some coupling conditions, describing the information exchange between the two problems.

As proposed in [69], the coupling conditions between the NS equations (3.1), without the Neumann conditions on each Γ^j, and the multi-compartment Darcy primal formulation (4.3) are the following:

- *conservation of mass*: the blood flux through each coronary outflow section Γ^j enters inside the corresponding perfusion region Ω_M^j only for the first compartment (the most upstream one). Thus, the volumetric source term g_1 should depend on the outgoing coronary flow rate, namely:

$$g_1(\mathbf{x}) = \sum_{j=1}^{N^j} \frac{\chi_{\Omega_M^j}(\mathbf{x})}{|\Omega_M^j|} \int_{\Gamma^j} \mathbf{u}_{AC} \cdot \mathbf{n} \, d\gamma, \tag{4.12}$$

  where $\mathbf{u}_{AC}$ is the fluid velocity of the NS problem (3.1) and the notation χ_A stands for the characteristic function of the domain A;

- *balance of interface forces*: due to the heterogeneity of the two models and the distributed nature of the Darcy model, we expect to have a pressure jump at the interface Γ^j which induces the following epicardial coronary flow rate [69]:

$$\int_{\Gamma^j} \mathbf{u}_{AC} \cdot \mathbf{n} \, d\gamma = \alpha^j \Big(\frac{1}{|\Gamma^j|} \int_{\Gamma^j} p_{AC}(\mathbf{x}) \, d\mathbf{x} - \frac{1}{|\Omega_M^j|} \int_{\Omega_M^j} p_{M,1}(\mathbf{x}) \, d\mathbf{x} \Big), \tag{4.13}$$

  with $j = 1, ..., N^j$, where p_{AC} is the fluid pressure of the NS problem (3.1) and α^j are the conductance parameters between epicardial coronary arteries and the porous medium, which depend on the perfusion region.

  Note that (4.13) provides an average condition, thus it is defective for a 3D Navier-Stokes problem [97, 98]. Therefore, it was reformulated in [69] into the following Robin-like condition, which guarantees enough boundary information for the normal component:

$$\begin{aligned} -p_{AC} + \mu(\nabla \mathbf{u}_{AC} + \nabla {\mathbf{u}_{AC}}^T)\mathbf{n} \cdot \mathbf{n} + \frac{1}{\alpha^j} \int_{\Gamma^j} \mathbf{u}_{AC} \cdot \mathbf{n} \, d\gamma \\ = -\frac{1}{|\Omega_M^j|} \int_{\Omega_M^j} p_{M,1}(\mathbf{x}) \, d\mathbf{x} \quad \text{on } \Gamma^j \end{aligned} \tag{4.14}$$

  for each $j = 1, ..., N^j$.

  Moreover, the NS problem also needs a condition for the tangential components, thus in [69] they assumed that the tangential tractions are null, i.e.:

$$\mu(\nabla \mathbf{u}_{AC} + \nabla {\mathbf{u}_{AC}}^T)\mathbf{n} \cdot \boldsymbol{\tau}_i = 0, \quad i = 1, 2 \quad \text{on } \Gamma^j, \tag{4.15}$$

where $\boldsymbol{\tau}_i$ are the two tangential unit vectors.

4.2.2. Coupled mathematical model

We are now ready to write the complete coupled mathematical model for myocardial perfusion with its coupling conditions. For simplicity we do not report here the boundary conditions on the aortic inlet (Γ_{in}) and outlet (Γ_{out}) sections (see (3.1)) and the boundary condition on myocardial boundary $\partial\Omega_M$ (see (4.3b)). Note that, as explained in Section 4.1.1, we only consider a 3-compartment Darcy model in its primal formulation.

Problem 4.3 (Coupled mathematical model)**.** *Given* ρ, μ, α^j, $\beta_{1,2} = \beta_{2,1}$, $\beta_{2,3} = \beta_{3,2}$, $\boldsymbol{K}_i$, γ *and* p_{veins}*, find* $p_{M,i}$, $\boldsymbol{u}_{AC}$ *and* p_{AC}, $i = 1, 2, 3$*, such that:*

$$\rho(\partial_t \mathbf{u}_{AC} + (\mathbf{u}_{AC} \cdot \nabla)\mathbf{u}_{AC}) - \mu\nabla \cdot (\nabla \mathbf{u}_{AC} + \nabla {\mathbf{u}_{AC}}^T) + \nabla p_{AC} = \mathbf{0} \quad \text{in } \Omega_{AC}, \tag{4.16a}$$

$$\nabla \cdot \mathbf{u}_{AC} = 0 \quad \text{in } \Omega_{AC}, \tag{4.16b}$$

$$\begin{aligned} -p_{AC} + \mu(\nabla \mathbf{u}_{AC} + \nabla {\mathbf{u}_{AC}}^T)\mathbf{n} \cdot \mathbf{n} + \frac{1}{\alpha^j} \int_{\Gamma^j} \mathbf{u}_{AC} \cdot \mathbf{n}\, d\gamma & \\ = -\frac{1}{\Omega^j_M} \int_{|\Omega^j_M|} p_{M,1}(\mathbf{x})\, d\mathbf{x} & \quad \text{on } \Gamma^j, \end{aligned} \tag{4.16c}$$

$$\mu(\nabla \mathbf{u}_{AC} + \nabla {\mathbf{u}_{AC}}^T)\mathbf{n} \cdot \boldsymbol{\tau}_i = 0, \qquad i = 1, 2 \qquad \text{on } \Gamma^j, \tag{4.16d}$$

$$-\nabla \cdot (\mathbf{K}_1 \cdot \nabla p_{M,1}) = \sum_{j=1}^{N^j} \frac{\chi_{\Omega^j_M}(\mathbf{x})}{|\Omega^j_M|} \int_{\Gamma^j} \mathbf{u}_{AC} \cdot \mathbf{n}\, d\gamma - \beta_{1,2}(p_{M,1} - p_{M,2}) \quad \text{in } \Omega_M, \tag{4.16e}$$

$$-\nabla \cdot (\mathbf{K}_2 \cdot \nabla p_{M,2}) = -\beta_{2,1}(p_{M,2} - p_{M,1}) - \beta_{2,3}(p_{M,2} - p_{M,3}) \quad \text{in } \Omega_M, \tag{4.16f}$$

$$-\nabla \cdot (\mathbf{K}_3 \cdot \nabla p_{M,3}) = -\gamma(p_{M,3} - p_{veins}) - \beta_{3,2}(p_{M,3} - p_{M,2}) \quad \text{in } \Omega_M. \tag{4.16g}$$

The model parameters α^j, $j = 1, ..., N^j$, $\beta_{1,2}$, $\beta_{2,3}$ and K_i, $i = 1, 2, 3$, were estimated for each patient in the study population of [70] according to the procedures proposed in [69] (see Sect. 4.2.3).

4.2.3. Model's parameters estimate

In [69] Di Gregorio and colleagues proposed a strategy for the estimation of the parameters of Problem 4.3, which was then applied in [70] for the patient-specific geometries of their study population. Since in this project we work with a subset of the patient-specific geometries used in [70], then we decided to leverage the estimates obtained in [70], without performing a new estimation of the model parameters. Nonetheless, let us briefly present the strategy proposed in [69] for the estimation.

Two preliminary steps are needed for the estimation of the model parameters α^j, $j = 1, ..., N^j$, $\beta_{1,2}$, $\beta_{2,3}$ and K_i, $i = 1, 2, 3$:

- division of the myocardial domain Ω_M into non overlapping perfusion regions Ω_M^j depending on the position of the corresponding coronary outlet boundary Γ^j. In particular, the strategy consists in the projection of the barycenter of each section Γ^j on the epicardial surface of $\partial\Omega_M$, so that, for each point in Ω_M, the closest projected barycenter can be identified by solving an Eikonal equation. A point in Ω_M is assigned to the perfusion region Ω_M^j associated to the coronary outlet Γ^j having the closest barycenter. As an example, in Figure 4.2a we report the perfusion regions obtained in [70] for patient P1.
- Generation of a surrogate intramural coronary network. To this purpose, in [69] they developed an algorithm inspired by the *bifurcating volume-filling network generation* algorithm proposed in [112, 113] and extended to the case of non-convex geometries using an approach similar to the one proposed in [114], based on isopotential surfaces constraint. Each vessel inside the surrogate intramural network is then assigned to a certain compartment exploiting a hierarchic parameter. In Figure 4.2b we report the surrogate intramural network generated in [70] inside the myocardial domain of patient P1.

The permeability tensors $\mathbf{K}_i$, $i = 1, 2, 3$, can be then estimated leveraging only the geometrical description of the surrogate intramural network. Indeed, a local porosity ϕ_i^j, associated to compartment i and perfusion region Ω_M^j, can be defined as the ratio between the volume of the network's vessels inside Ω_M^j belonging to compartment i and the total volume of Ω_M^j. In [69] they assumed to have an isotropic permeability tensor inside each perfusion region and compartment, which only depends on the local porosity ϕ_i^j. The choice of an isotropic tensor is motivated by the observation made in [62] that the error between the Poiseuille and the multi-compartment pressures is smaller with respect to that obtained by using an anisotropic tensor, computed for instance with Huyghe and Van Campen method (see Sect. 1.4.3).

On the other hand, some information regarding the fluid dynamics properties of the surrogate intramural network are needed to estimate the parameters $\beta_{i,k}$ and α^j. In particular, the strategy proposed in [69] consists in the solution of a Poiseuille flow problem inside the epicardial coronary arteries and the surrogate intramural network and the

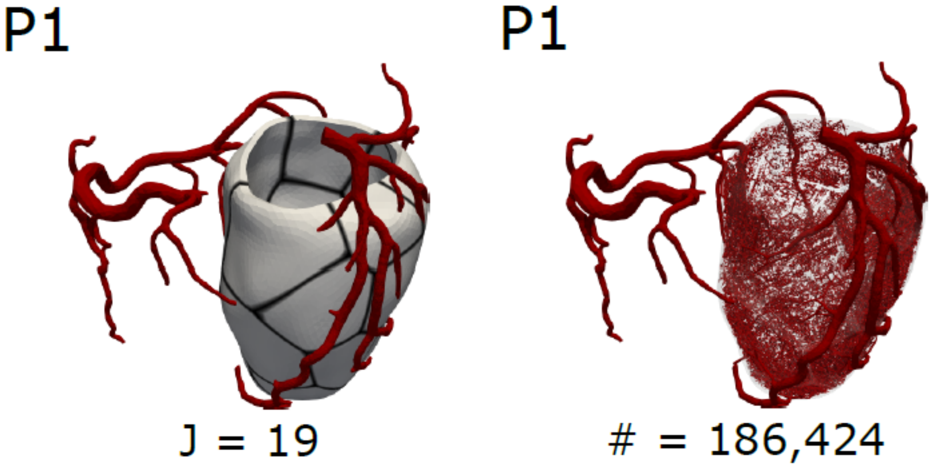

(a) (b)

Figure 4.2: (a) Perfusion regions obtained in [70] for patient P1; J is the number of perfusion regions. (b) Surrogate intramural vascular network generated inside the myocardial domain Ω_M in [70] for patient P1 and used only for the estimation of the parameters; the total number of vessels is also reported.

estimation of the parameters based on the computed Poiseuille flow rates and pressure jumps between the epicardial arteries and the different compartments of the network.

Notice that the surrogate intramural networks are used only for the estimation of the model parameters. Indeed, blood dynamics inside the intramural vessels are not solved explicitly inside the network, but they are modelled through a porous medium approach as explained in Section 4.1.

Please refer to [71] for a detailed description of all the procedures involved in the estimation of the model parameters.

4.3. Numerical approximation of the coupled model

In this section we present all the numerical techniques applied in order to numerically solve Problem 4.3. We considered a Finite Element approach for the spatial discretization and a Finite Difference method for the temporal discretization. Moreover, an iterative splitting strategy was enforced for the numerical solution of the coupled problem, so that the NS and the multi-compartment Darcy problems were solved sequentially, resorting to available Finite Element solvers for each sub-problem.

4.3.1. Temporal discretization and iterative splitting

For the time discretization of Problem 4.3 we followed the same approach presented in Section 3.3.1. In particular, the interval $[0, T]$ is divided into N_t sub-intervals of constant length Δt ($t^n := n\Delta t$, $n = 0, ..., N_t$), the time derivative in the NS problem is discretized with a BDF of order 1 and a semi-implicit treatment of the convective NS term is considered. Moreover, we denote with z^n the value of a generic time function z evaluated at $t = t^n$.

In order to reduce the complexity of the implementation, as proposed in [69], an iterative splitting strategy is enforced for the numerical solution of Problem 4.3 instead of a monolithic approach. Indeed, the former strategy consists in the sequential resolution of the two sub-problems, thus allowing us to exploit the available Navier-Stokes and multi-compartment Darcy solvers.

In particular, the splitting strategy consists in the sequential resolutions of a NS problem equipped with a Neumann boundary condition on each Γ^j, which comes from the Robin condition (4.16c), and a multi-compartment Darcy problem where the volumetric source term in the first compartment depends on the NS solution.

The iterative splitting strategy is described in Algorithm 4.1: the current temporal index $n + 1$ is omitted for notation, s is the current iteration, ϵ_{tol} is a given tolerance, $diff_x = \frac{\|x^{(s)} - x^{(s-1)}\|}{\|x^{(s)}\|}$, where we considered the $[H^1]^3$ norm for the velocity and the L^2 norm for pressures. Moreover, a relaxation of the solutions $p_{M,1}$ and $\mathbf{u}_{AC}$ is introduced at each iteration exploiting the relaxation coefficients ω_M and ω_{AC}.

Note that, for the sake of simplicity we reported in Algorithm 4.1 only the coupling conditions, thus neglecting the boundary conditions related to the single problems. In particular, we considered a defective flow rate condition on the aortic outlet section for the NS problem (see Sect. 3.1), thus such problem is numerically solved at point 3. of the Algorithm exploiting the augmented weak formulation presented in Section 3.2. Moreover, if we neglect the while loop inside Algorithm 4.1, thus performing only one iteration for each time step, then we obtain a fully explicit scheme.

In [69] a more detailed description of the splitting strategy is provided together with a convergence analysis in the simplified case of a Stokes problem for fluid dynamics in large arteries, thus neglecting the convective term of the Navier-Stokes equations.

Algorithm 4.1 Iterative splitting strategy for Problem 4.3

```
for $n = 0, ..., N_t - 1$ do
    while $max(diff_{\mathbf{u}_{AC}}; diff_{p_{AC}}; diff_{p_{M,1}}) > \epsilon_{tol}$ do
        Solve the Navier-Stokes problem at iteration s:
        $\rho\Big(\frac{\tilde{\mathbf{u}}_{AC}^{(s)} - \mathbf{u}_{AC}^{n}}{\Delta t} + (\mathbf{u}_{AC}^{n} \cdot \nabla)\tilde{\mathbf{u}}_{AC}^{(s)}\Big) - \mu\nabla \cdot (\nabla\tilde{\mathbf{u}}_{AC}^{(s)} + \nabla\tilde{\mathbf{u}}_{AC}^{(s)\,T}) + \nabla p_{AC}^{(s)} = \mathbf{0} \quad \text{in } \Omega_{AC}, \quad (4.17a)$
        $\nabla \cdot \tilde{\mathbf{u}}_{AC}^{(s)} = 0 \quad \text{in } \Omega_{AC}, \quad (4.17b)$
        $-p_{AC}^{(s)} + \mu(\nabla\tilde{\mathbf{u}}_{AC}^{(s)} + \nabla\tilde{\mathbf{u}}_{AC}^{(s)\,T})\mathbf{n} \cdot \mathbf{n} = -\frac{1}{|\Omega_M^j|}\int_{\Omega_M^j} p_{M,1}^{(s-1)}\, d\mathbf{x} - \frac{1}{\alpha^j}\int_{\Gamma^j} \mathbf{u}_{AC}^{(s-1)} \cdot \mathbf{n}\, d\gamma \quad \text{on } \Gamma^j, \quad (4.17c)$
        $\mu(\nabla\tilde{\mathbf{u}}_{AC}^{(s)} + \nabla\tilde{\mathbf{u}}_{AC}^{(s)\,T})\mathbf{n} \cdot \boldsymbol{\tau}_i = 0, \quad i = 1, 2 \quad \text{on } \Gamma^j \quad (4.17d)$
        Solve the multi-compartment Darcy problem at iteration s:
        $-\nabla \cdot (\mathbf{K}_1 \nabla\tilde{p}_{M,1}^{(s)}) = \sum_{j=1}^{N^j} \frac{\chi_{\Omega_M^j}}{|\Omega_M^j|}\int_{\Gamma^j} \tilde{\mathbf{u}}_{AC}^{(s)} \cdot \mathbf{n}\, d\gamma - \beta_{1,2}(\tilde{p}_{M,1}^{(s)} - p_{M,2}^{(s)}) \quad \text{in } \Omega_M, \quad (4.18a)$
        $-\nabla \cdot (\mathbf{K}_2 \nabla p_{M,2}^{(s)}) = -\beta_{2,1}(p_{M,2}^{(s)} - \tilde{p}_{M,1}^{(s)}) - \beta_{2,3}(p_{M,2}^{(s)} - p_{M,3}^{(s)}) \quad \text{in } \Omega_M, \quad (4.18b)$
        $-\nabla \cdot (\mathbf{K}_3 \nabla p_{M,3}^{(s)}) = -\gamma(p_{M,3}^{(s)} - p_{veins}) - \beta_{3,2}(p_{M,3}^{(s)} - p_{M,2}^{(s)}) \quad \text{in } \Omega_M \quad (4.18c)$
        $p_{M,1}^{(s)} = \omega_M \tilde{p}_{M,1}^{(s)} + (1 - \omega_M)p_{M,1}^{(s-1)}$
        $\mathbf{u}_{AC}^{(s)} = \omega_{AC}\tilde{\mathbf{u}}_{AC}^{(s)} + (1 - \omega_{AC})\mathbf{u}_{AC}^{(s)}$
        $s \to s + 1$
    end while
end for
```

4.3.2. Spatial discretization and algebraic counterpart

According to Algorithm 4.1, we consider to numerically solve the coupled formulation of Problem 4.3 by solving each sub-problem in a sequential fashion, thus we can rely on the spatial discretization of the single problems presented in Section 3.3 for Navier-Stokes and in Section 4.1.3 for the multi-compartment Darcy. In particular, we introduce two regular triangulations $\mathcal{T}^h_{AC}$, $\mathcal{T}^h_M$ for the two domains involved in the coupled problem Ω_{AC}, Ω_M, respectively. As explained in Section 2.5, notice that $\mathcal{T}^h_{AC}$ is made of tetrahedral elements K, while $\mathcal{T}^h_M$ of hexahedral elements Ω_K.

Let us define the discrete sub-spaces needed for the numerical approximation of each problem:

$$\begin{aligned} V^h_{AC} &= \{\mathbf{v}_h \in [H^1(\Omega_{AC})]^3 : \mathbf{v}_h|_K \in \mathbb{P}^1(K)\ \forall K \in \mathcal{T}^h_{AC}\}, \\ Q^h_{AC} &= \{q_h \in L^2(\Omega_{AC}) : q_h|_K \in \mathbb{P}^1(K)\ \forall K \in \mathcal{T}^h_{AC}\}, \\ Q^h_M &= \{q_h \in L^2(\Omega_M) : q_h|_{\Omega_K} \in \mathbb{Q}^1(\Omega_K)\ \forall \Omega_K \in \mathcal{T}^h_M\}. \end{aligned} \tag{4.19}$$

with $dim(V^h_{AC}) = N^h_{AC} < +\infty$, $dim(Q^h_{AC}) = M^h_{AC} < +\infty$ and $dim(Q^h_M) = M^h_M < +\infty$. Remember that, since the spaces for the velocity and pressure variables of the NS problem do not satisfy the inf-sup condition, then we consider a SUPG-PSPG stabilization of the discrete problem, as explained in Section 3.3.2.

The discrete weak formulation of the Navier-Stokes sub-problem (4.17) is equivalent to formulation (3.12) presented in Section 3.3.2 just by suitably modifying the terms related to the Neumann conditions on each Γ^j. Moreover, the Galerkin formulation of the multi-compartment Darcy equations (4.18) is the one reported in formulation (4.8) (Sect. 4.1.2), taking the trial and test functions inside the discrete space Q^h_M and substituting the correct expression for g_1. For these reasons, we do not report here such formulations, but we just consider the algebraic linear systems arising from the numerical solution of each sub-problem in Algorithm 4.1.

Let us denote as $\{\boldsymbol{\varphi}_{AC,l}\}_{l=1}^{N^h_{AC}}$, $\{\psi_{AC,l}\}_{l=1}^{M^h_{AC}}$, $\{\psi_{M,l}\}_{l=1}^{M^h_M}$ the basis functions for V^h_{AC}, Q^h_{AC}, Q^h_M, respectively. Then, each function belonging to a discrete functional space can be expressed as a linear combination of the basis functions related to that space. So that, we can identify as $\mathbf{U}^{(s)}_{AC}$, $\mathbf{P}^{(s)}_{AC}$, $\mathbf{P}^{(s)}_{M,i}$ the vectors of components of each unknown function at iteration s in Algorithm 4.1 with respect to the related basis functions. Analogously the apex n stands for the time-step $t = t^n$.

We are now ready to write the algebraic linear systems to be solved sequentially for each iteration s of Algorithm 4.1:

$$\begin{bmatrix} \mathbb{F}(\mathbf{U}^n_{AC}) & \mathbb{B}^t & \Phi^t \\ \mathbb{B} & \mathbb{S} & 0 \\ \Phi & 0 & 0 \end{bmatrix} \begin{bmatrix} \mathbf{U}^{(s)}_{AC} \\ \mathbf{P}^{(s)}_{AC} \\ \lambda^{(s)} \end{bmatrix} = \begin{bmatrix} \mathbf{G}^n_{AC} + \mathbf{C}_1(\mathbf{U}^{(s-1)}_{AC}) + \mathbf{C}_2(\mathbf{P}^{(s-1)}_{M,1}) \\ 0 \\ Q^{n+1}_{out} \end{bmatrix}, \tag{4.20}$$

$$\begin{bmatrix} \mathbb{D}_1 + \mathbb{C}_{12} & -\mathbb{C}_{12} & 0 \\ -\mathbb{C}_{21} & \mathbb{D}_2 + \mathbb{C}_{21} + \mathbb{C}_{23} & -\mathbb{C}_{23} \\ 0 & -\mathbb{C}_{23} & \mathbb{D}_3 + \mathbb{C}_{32} + \mathbb{C}_{\gamma} \end{bmatrix} \begin{bmatrix} \mathbf{P}_{M,1}^{(s)} \\ \mathbf{P}_{M,2}^{(s)} \\ \mathbf{P}_{M,3}^{(s)} \end{bmatrix} = \begin{bmatrix} \mathbf{G}_1(\mathbf{U}_{AC}^{(s)}) \\ 0 \\ \mathbf{G}_3 \end{bmatrix}, \tag{4.21}$$

where $\lambda^{(s)}$ is the Lagrange multiplier at iteration s used to weakly impose the defective flow rate condition on the aortic outlet Γ_{out} (see Sect. 3.3.3); $\mathbb{F}(\mathbf{U}_{AC}^n) = \frac{1}{\Delta t}\mathbb{M} + \mathbb{A} + \mathbb{N}(\mathbf{U}_{AC}^n)$; $\mathbf{G}_{AC}^n = \frac{1}{\Delta t}\mathbb{M}\mathbf{U}_{AC}^n$.

In the following we report only the definitions of the vectors appearing for the first time in (4.20)-(4.21), for the definitions of the remaining matrices and vectors please refer to Section 3.3.3 for the Navier-Stokes problem and to Section 4.1.3 for the multi-compartment Darcy. We have that:

$$\begin{aligned}
&[\mathbf{C}_1(\mathbf{U}_{AC}^{(s-1)})]_l = -\sum_{j=1}^{N^j} \frac{1}{\alpha^j} \int_{\Gamma^j} \mathbf{u}_{AC}^{(s-1)} \cdot \mathbf{n}\, d\gamma \int_{\Gamma^j} \boldsymbol{\varphi}_l \cdot \mathbf{n}\, d\gamma && \mathbf{C}_1(\mathbf{U}_{AC}^{(s-1)}) \in \mathbb{R}^{N_{AC}^h}, \\
&[\mathbf{C}_2(\mathbf{P}_{M,1}^{(s-1)})]_l = -\sum_{j=1}^{N^j} \frac{1}{|\Omega_M^j|} \int_{\Omega_M^j} p_{M,1}^{(s-1)}\, d\mathbf{x} \int_{\Gamma^j} \boldsymbol{\varphi}_l \cdot \mathbf{n}\, d\gamma && \mathbf{C}_2(\mathbf{P}_{M,1}^{(s-1)}) \in \mathbb{R}^{N_{AC}^h}, \\
&[\mathbf{G}_1(\mathbf{U}_{AC}^{(s)})]_k = (\sum_{j=1}^{N^j} \frac{\chi_{\Omega_M^j}}{|\Omega_M^j|} \int_{\Gamma^j} \mathbf{u}_{AC}^{(s)} \cdot \mathbf{n}\, d\gamma) \int_{\Omega_M} \psi_k\, d\mathbf{x} && \mathbf{G}_1(\mathbf{U}_{AC}^{(s)}) \in \mathbb{R}^{M_M^h},
\end{aligned} \tag{4.22}$$

where

$$\begin{aligned}
\mathbf{u}_{AC}^{(s)} &= \sum_{l=1}^{N_{AC}^h} [\mathbf{U}_{AC}^{(s)}]_l \boldsymbol{\varphi}_l \\
p_{M,1}^{(s-1)} &= \sum_{k=1}^{M_M^h} [\mathbf{P}_{M,1}^{(s-1)}]_k \psi_k
\end{aligned}$$

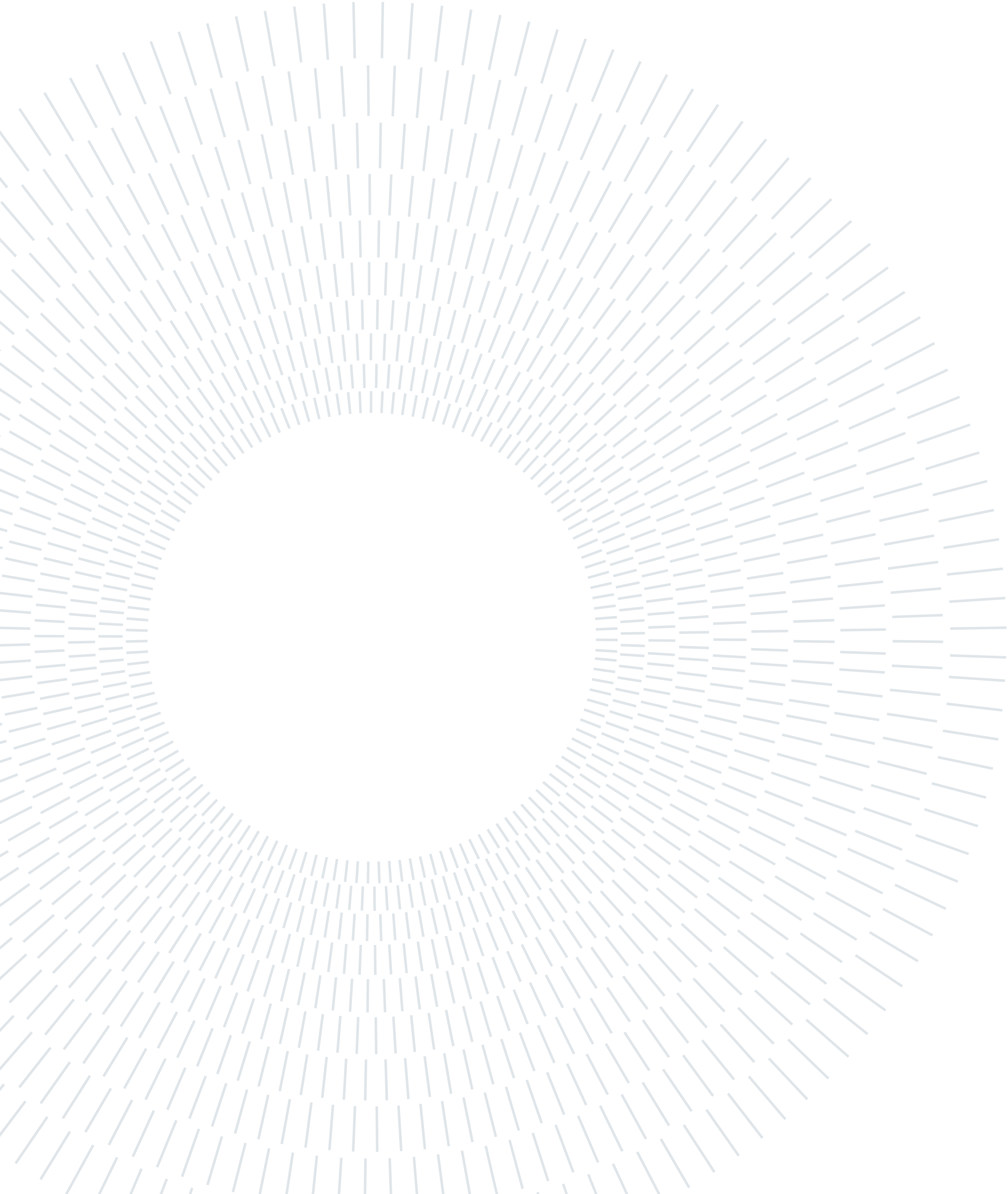

5 | Application of the coupled model to patient-specific cases

In this Chapter we apply the multi-physics computational model presented in Chapter 4 to numerically simulate myocardial perfusion in patient-specific geometries. In particular, we are interested in computing myocardial blood flow (MBF) maps, which are a visualization of MBF under stress conditions that can be obtained both from numerical and clinical data.

We considered patient P2, P3 and P4, whose computational domains are reported in Figure 2.17. Remember that all these patients are considered healthy, since no functionally significant coronary artery disease was detected by clinicians in their cases. We do not perform numerical simulations of cardiac perfusion for patient P1 due to missing data for this patient, therefore only hemodynamics simulations inside aortic root and epicardial coronary arteries were performed in the computational domain for patient P1 (see Sect. 3.6), whereas the coupled computational model for myocardial perfusion is applied for all the other patients (P2, P3 and P4).

The chapter is structured as follows:

- in Section 5.1 we briefly present MBF maps, showing that we have a one to one comparison between numerical and clinical data.
- In Section 5.2 we report some strategies, proposed in [70], that can be used to adjust the model parameters in order to account for stress conditions. In particular, we consider a stress *a priori* parameter adjustment, just accounting for stress conditions (Sect. 5.2.1), and a patient-specific optimization, exploiting the clinical MBF maps (Sect. 5.2.2).
- In Section 5.3 we perform an analysis of the computational model in different scenarios in order to understand their impact on the numerical results and corresponding computation of MBF maps. In particular, we compare the implicit and explicit formulations of the proposed splitting strategy (Sect. 5.3.1), we investigate the effect of

a change of venous pressure and drain coefficient on the pressure field (Sect. 5.3.2) and we analyze how changing the cardiac output influences the numerical results (Sect. 5.3.3).

- In Section 5.4 we assess the reliability of the model by comparing patient-specific MBF maps obtained from numerical results with the same maps obtained from clinical data. In particular, numerical MBF maps are computed both after the stress *a priori* parameter adjustment (Sect. 5.4.1) and after the patient-specific optimization (Sect. 5.4.2).
- in Section 5.5 we provide some final remarks on the coupled model for myocardial perfusion.

5.1. Myocardial blood flow maps

Our multi-physics coupled computational model for myocardial perfusion provides quantitative information regarding blood flow inside the cardiac micorvasculature by numerically solving a multi-compartment Darcy model inside the left ventricle. In particular, we can compute the numerical myocardial blood flow (MBF_{COMP}) as the amount of blood flow reaching the third compartment, related to the capillaries, where oxygen and nutrients exchange happens, namely:

$$\text{MBF}_{\text{COMP}} = \beta_{2,3} * (p_{M,2} - p_{M,3}) * 60[s/min] * 100[ml], \tag{5.1}$$

where the factors $60[s/min]$ and $100[ml]$ are used to express MBF_{COMP} in $[ml/min/100ml]$. Therefore, applying our computational model we have a 3D visualization of MBF_{COMP} inside the left ventricle, thanks to the 3D description of the myocardium.

In order to assess the validity of our model we want to compare the numerical results with some clinical data providing the distribution of MBF inside the left ventricle. This can be done by leveraging the stress myocardial computed tomography perfusion (stress-CTP), which is a CT examination used in clinical practice for the analysis of myocardial perfusion and for the detection of ischemic regions. Stress-CTP is performed under stress conditions, achieved with pharmacological agents administration, such as adenosine. For a detailed description of the stress-CTP acquisition please refer to [71]. A visualization of MBF inside the myocardium, called MBF_{CTP}, can be obtained from a post-processing of stress-CTP images (see Fig. 5.1a)

Such MBF_{CTP} images were processed in [70] using the open-source software ParaView

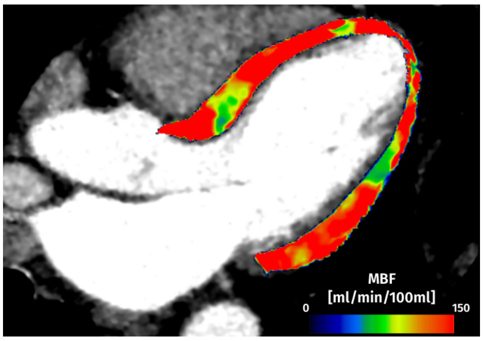

(a)

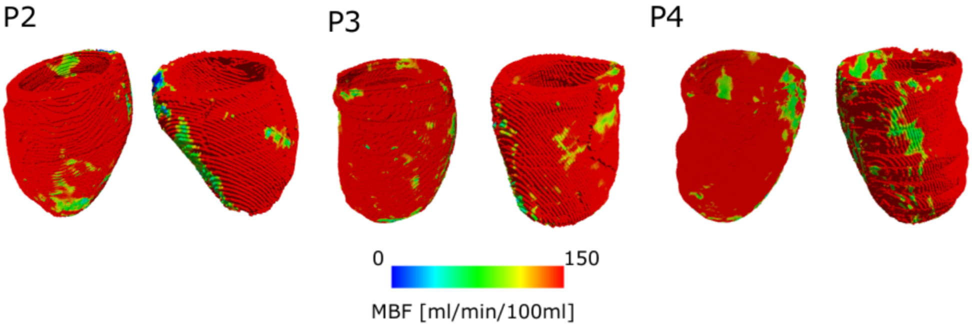

(b)

Figure 5.1: (a) $\mathrm{MBF}_{\mathrm{CTP}}$ computed from stress-CTP acquisition. (b) 3D reconstructions of $\mathrm{MBF}_{\mathrm{CTP}}$ for patients P2, P3, and P4. [71]

(`https://www.paraview.org/`) in order to obtain a 3D visualization of $\mathrm{MBF}_{\mathrm{CTP}}$ inside the myocardium for each patient in their study population. So that, the 3D visualizations of $\mathrm{MBF}_{\mathrm{CTP}}$ were already available for patients P2, P3, and P4 considered in this study (see Fig. 5.1b).

It is possible to compute the average in space of MBF inside the domain Ω_M both from numerical and clinical data as follows:

$$\mathrm{MBF}_*^{\mathrm{avg}} = \frac{1}{|\Omega_M|} \int_{\Omega_M} \mathrm{MBF}_*(\mathbf{x})\, d\mathbf{x}, \qquad * = \mathrm{CTP}, \mathrm{COMP}. \tag{5.2}$$

Moreover, we can define:

$$\mathrm{CBF}_{\mathrm{MBF}} = |\Omega_M| \mathrm{MBF}_{\mathrm{CTP}}^{\mathrm{avg}}, \tag{5.3}$$

which will be used to set a patient-specific flow rate inside the epicardial coronary arteries in the numerical simulations. In Table 5.1 we show the values of $\mathrm{MBF}_{\mathrm{CTP}}^{\mathrm{avg}}$ and $\mathrm{CBF}_{\mathrm{MBF}}$ computed for each patient P2-P3-P4.

	$\mathbf{MBF^{avg}_{CTP}}$ $(ml/min/100ml)$	$\mathbf{CBF_{MBF}}$ (ml/min)
P2	314.95	251.51
P3	246.75	230.77
P4	281.38	313.17

Table 5.1: Values of $\mathrm{MBF}^{\mathrm{avg}}_{\mathrm{CTP}}$ and $\mathrm{CBF}_{\mathrm{MBF}}$ for all three patients considered in this study

Finally, we can compute the average in space MBF inside each perfusion region Ω^j_M as:

$$\mathrm{MBF}^j_* = \frac{1}{|\Omega^j_M|}\int_{\Omega^j_M} \mathrm{MBF}_*(\mathbf{x})\, d\mathbf{x}, \qquad * = \mathrm{CTP}, \mathrm{COMP} \tag{5.4}$$

and use it in order to define a global perfusion map:

$$\overline{\mathrm{MBF}}_*(\mathbf{x}) = \sum_{j=1}^{N^j} \mathrm{MBF}^j_*\, \chi_{\Omega^j_M}(\mathbf{x}), \qquad * = \mathrm{CTP}, \mathrm{COMP}, \tag{5.5}$$

where $\chi_{\Omega^j_M}$ denotes the characteristic function of the perfusion region Ω^j_M.

The $\overline{\mathrm{MBF}}_{\mathrm{CTP}}(\mathbf{x})$ maps are shown in Figure 5.2 for each of the three considered patients.

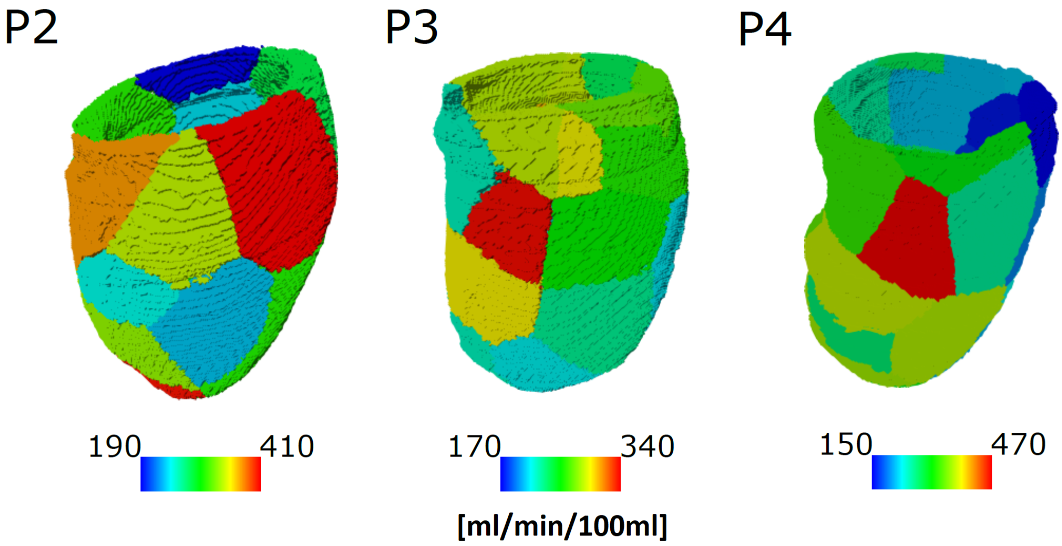

Figure 5.2: Representation of $\overline{\mathrm{MBF}}_{\mathrm{CTP}}(\mathbf{x})$ across the myocardium for patients P2, P3, and P4. [71]

In order to validate of our model we will compare in terms of the average $\mathrm{MBF}^{\mathrm{avg}}_*$ and the global map $\overline{\mathrm{MBF}}_*(\mathbf{x})$ (*=CTP,COMP) the numerical results with clinical data.

5.2. Model adjustment in stress conditions

The pharmacological induced stress conditions involved in the acquisition of stress-CTP have non negligible effects on the geometrical and functional features of the coronary circulation, such as:

- vasodilation of the epicardial coronary arteries: in Table 5.2 we report for each patient the radius increase of an epicardial coronary artery tract;
- vasodilation of the intramural vessels: the resistance of such vessels decreases about 10-12 fold during adenosine injection [115];
- vasodilation of the venous network: the coronary sinus radius before and after adenosine injection is also reported in Table 5.2;
- increase of heart rate (HR): the HR under stress condition is reported in Table 5.2 for each patient;
- increase of CBF and resulting MBF: the patient-specific values of MBF and CBF are reported in Table 5.1.

Id	Rest HR (bpm)	Stress HR (bpm)	Sampled coronary	Rest diameter [mm]	Stress diameter [mm]	Rest coronary sinus [mm]	Stress coronary sinus [mm]
P2	55	93	Distal RCA	2.6	3.2	3.6	7.6
P3	57	63	Distal RCA	2.5	3.0	8.6	9.0
P4	70	72	Distal RCA	2.5	2.9	5.6	8.2

Table 5.2: Effects of pharmacological induced stress conditions on each patient. RCA = right coronary artery. [71]

Therefore, for accurate numerical results in terms of MBF maps, we have to adjust our model in order to account for such effects. In [70] Di Gregorio, Vergara and colleagues analyzed the impact of each stress induced effect on the computational model. In particular they found that the vasodilation of the epicardial coronary arteries and the venous network causes only a decrease of the pressure field, while preserving the pressure gradient between different compartments, thus the MBF maps are not affected by these effects and they did not consider them. Moreover, they proposed an approach, based on an adjustment of the model parameters, in order to account for the other stress induced effects, which all have a non negligible impact on the MBF maps computation. Finally, they introduced a further optimization of the model parameters, exploiting the $\overline{\mathrm{MBF}}_{\mathrm{CTP}}(\mathbf{x})$ global maps introduced in Section 5.1.

Let us present here both parameter adjustment strategies proposed in [70]: one just accounting for the pharmacological induced stress conditions, called stress *a priori* parameter adjustment, and the other also exploiting $\overline{\mathrm{MBF}}_{\mathrm{CTP}}(\mathbf{x})$ maps obtained from clinical data, called patient-specific parameter optimization

5.2.1. Stress *a priori* parameters adjustment

The model parameters estimated in rest conditions according to the procedure presented in Section 4.2.3 have to be adjusted in order to account for the stress conditions induced by pharmacological agents administration, involved in the stress-CTP acquisition protocol. Moreover, some systematic adjustment to the parameters $\beta_{i,k}$ were enforced in [70].

In particular, the stress *a priori* parameters adjustment, proposed in [70] can be divided in several points:

- due to the vasodilation of intramural vessels, the resistance of the arterial vessels penetrating inside the myocardium decreases by about 10-fold [115]. Thus, the conductances $\beta_{1,2}$ and $\beta_{2,3}$ and the permeabilities of the first two compartments $\mathbf{K}_1$ and $\mathbf{K}_2$ were increased by 10-fold with respect to the parameters estimated in rest conditions;
- the values of $\beta_{1,2}$ and $\beta_{2,3}$ in each perfusion region were rescaled in an interval from $+40\%$ to -40% of the average value of $\beta_{1,2}$ and $\beta_{2,3}$, respectively, to avoid outlier values leading to unphysiological perfusion values in specific regions;
- the values of $\beta_{1,2}$ and $\beta_{2,3}$ of the perfusion regions of the septum were augmented. This was done to compensate the lack of resolution of cCTA images, which does not allow the reconstruction of the septal perforating arteries responsible for the septal perfusion.

Notice that the increase of HR and CBF in stress conditions does not have an impact on the model parameters, but only on the temporal flow rate profile imposed inside the epicardial coronary network. Thus, such increase will be taken into account when prescribing the boundary condition for the Navier-Stokes problem solved inside the aortic root and epicardial coronary arteries according to Algorithm 4.1.

5.2.2. Patient-specific parameter optimization

A further optimization of the parameters $\beta_{1,2}$ and $\beta_{2,3}$ was proposed in [70] exploiting the $\overline{\mathrm{MBF}}_{\mathrm{CTP}}(\mathbf{x})$ patient-specific global maps obtained from stress-CTP. In particular, they introduced an iterative strategy for the minimization, inside each perfusion region Ω_M^j, of the relative error between MBF obtained from stress-CTP ($\mathrm{MBF}_{\mathrm{CTP}}^j$) and MBF computed from numerical simulations ($\mathrm{MBF}_{\mathrm{COMP}}^j$). Depending on whether the computational model overestimate or underestimate MBF in a certain Ω_M^j, at each iteration the values of $\beta_{1,2}$ and $\beta_{2,3}$ in Ω_M^j are either increased or decreased by a factor proportional to the ratio between $\mathrm{MBF}_{\mathrm{CTP}}^j$ and $\mathrm{MBF}_{\mathrm{COMP}}^j$. The iterative algorithm stops when the relative error between $\mathrm{MBF}_{\mathrm{CTP}}^j$ and $\mathrm{MBF}_{\mathrm{COMP}}^j$ is below a certain tolerance in each perfusion region. For a detailed description of this optimization procedure please refer to [70].

5.3. Numerical results in different scenarios

As already mentioned in the introduction of this chapter, before validating our multi-physics computational model for myocardial perfusion with patient-specific clinical data we are interested in analyzing some numerical results obtained in different scenarios. For simplicity, we carry out such analysis only for patient P2, but the same considerations can be made also for patient P3 and P4. In Figure 5.3 we report the computational domains of patient P2 used in this analysis.

We aim at numerically solving the coupled mathematical model introduced in Problem 4.3 by following the iterative splitting strategy presented in Algorithm 4.1 inside the patient-specific computational domains depicted in Figure 5.3 for different choices of the model parameters. Let us report here the baseline values of the parameters: $\rho = 1.06\ [g/cm^3]$, $\mu = 0.035\ [dyne \cdot s/cm^2]$, $\gamma = 10^{-4}\ [1/Pa \cdot s]$, $\omega_{AC} = \omega_M = 1$, $\epsilon_{tol} = 10^{-5}$, $p_{veins} = 22.5\ [mmHg]$ [59], whereas the parameters α^j, $\beta_{i,k}$ and $\mathbf{K}_i$ are estimated in rest conditions following the procedure presented in Section 4.2.3 and adjusted to stress condition using both the *a priori* adjustment and the patient-specific optimization (see Section 5.2). Any deviation from these baseline values will be reported. Moreover, the Finite Element library $life^x$ (`https://lifex.gitlab.io/`) is used to perform all the simulations and each continuous sub-problem in Problem 4.3 is discretized following the strategies presented in Section 4.3. In particular, we considered a semi-implicit Backward Difference Formulation of order 1 for time discretization using $\Delta t = 5 \times 10^{-3}\ [s]$, P1/P1 Finite Elements with a SUPG-PSPG stabilization for the NS sub-problem and Q1 Finite Elements for the multi-compartment Darcy sub-problem in primal formulation.

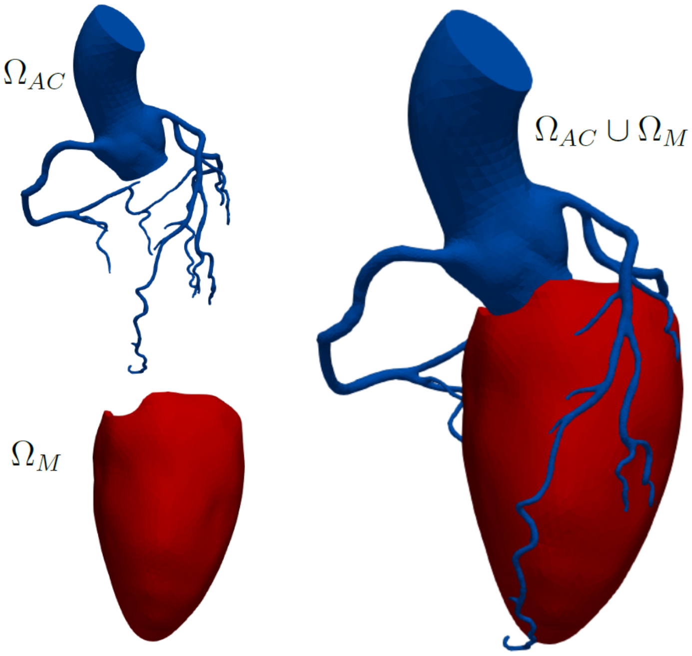

Figure 5.3: P2 patient-specific computational domains for aortic root and epicardial coronaries (Ω_{AC}) and left ventricle (Ω_M). *Coupled perfusion model*

The coupled problem only needs boundary conditions on the inlet and outlet cross-sections of the aortic root. Indeed, the coupling conditions are prescribed on the coronary outlet sections for the NS sub-problem (see Sect 4.2.1) and the null flux condition through the boundary $\partial\Omega_M$ is automatically imposed in the weak formulation of the multi-compartment Darcy (see Sect 4.1.2).

Analogously to what was done in Section 3.6, we prescribed a physiological flow rate on the aortic outlet boundary (see Fig. 5.4a) [106], whereas on the aortic inlet we assigned a flow rate computed as the sum of the flow rate on the aortic outlet and the expected flow rate inside the coronary circulation (see Fig. 5.4b) [107]. In order to account for stress conditions such profiles were scaled in such a way that the mean cardiac output during an heartbeat is ~ 15 $[L/min]$, three times the mean cardiac output in rest conditions, as suggested by [108, 116]. Moreover, notice that the expected flow rate in the coronaries is obtained from blood flow measurements inside the Left Anterior Descending (LAD) coronary branch [107] by scaling the profile to match a patient-specific CBF datum. In particular, the coronary flow rate profile was scaled in such a way that the peak value of CBF during early diastole coincides with the value of CBF_{MBF} reported in Table 5.1. Since in this study we aim at simulating cardiac perfusion only in the left ventricle, then we considered only the epicardial coronaries supplying blood to this chamber (see Sect. 2.3.1), so that it makes sense to impose in the coronary circulation a flow rate profile taken from a left coronary branch. Each profile was also scaled in time in order to match the patient-specific HR under stress conditions reported in Table 5.2.

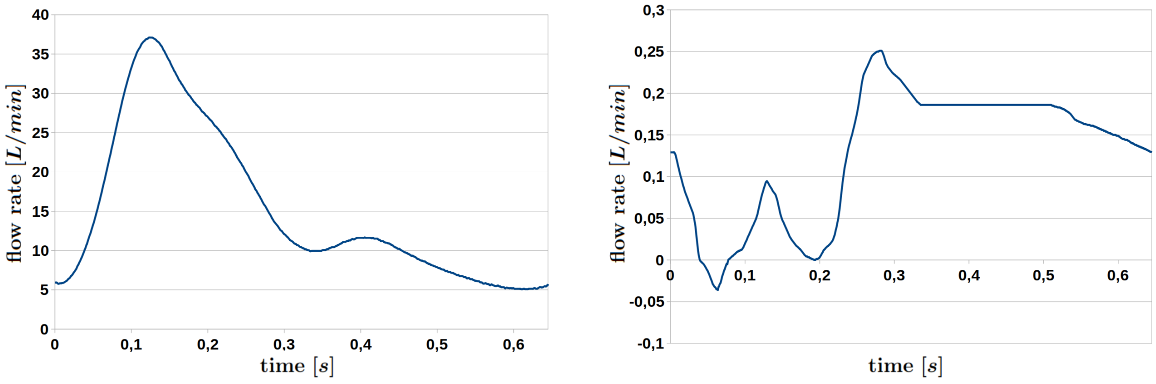

(a)

(b)

Figure 5.4: (a) Assigned flow rate on the aortic outlet section [106]. (b) Expected flow rate in coronary circulation [107]. The profile in the coronaries was scaled so that the peak value reached in early diastole is equal to CBF_{MBF} for patient P2, reported in Table 5.1. *Coupled perfusion model*

Let us specify that all the parameters of our model are static in time, thus the only source of time-dependency is represented by the time-varying flow rate inside the aortic root and the epicardial coronaries. In particular, each pressure field ($p_{M,1}$, $p_{M,2}$, $p_{M,3}$ and p_{AC}) depends on the constant venous pressure of 22.5 [$mmHg$], assigned as sink term for the last Darcy compartment, and the pressure gradients in the myocardium and the epicardial coronaries, which are proportional to CBF. For this reason each pressure fields will present a time profile similar to the one of the CBF, which is not physiological for pressure, specially during systole. Nonetheless, we aim at simulating cardiac perfusion during diastole, since 80 % of the total left CBF occurs in this period, thus we accept such inaccuracy. In order to get more physiologically consistent time profile for the pressure fields, myocardial contraction should be considered in future studies, either by introducing time-dependent parameters or by proposing a poro-elastic model for the myocardium.

5.3.1. Comparison between implicit and explicit splitting strategies

As a first analysis we compare the numerical results obtained using the implicit and explicit version of the iterative splitting strategy proposed in Algorithm 4.1. Remember that the explicit version consists in performing just one splitting iteration at each time step.

We aim at investigating:

- if the explicit version of Algorithm 4.1 is stable and accurate with respect to the implicit version in patient-specific geometries;
- the convergence properties of the implicit version of Algorithm 4.1.

In Figure 5.5 we report for different time instants the pressure distribution across the domain Ω_{AC} and the pressure of the first Darcy compartment inside Ω_M, obtained with both the explicit and implicit versions of Algorithm 4.1. The flow rate profiles inside the aorta and the coronary circulation are reported together with a red dot indicating the location of each time-instant on such profiles.

Notice that the absolute pressure values in Figure 5.5, although physically meaningful, are lower than the expected physiological values. Nonetheless, the model correctly predicts the temporal evolution of the pressure gradient inside both Ω_M and Ω_{AC}. Moreover, in this study numerical simulations are aimed at the prediction of blood flow distribution rather than pressure, thus such issues are considered of secondary importance.

Figure 5.5 shows that the solutions obtained following the two numerical strategies present significant differences inside the domain Ω_{AC} during systole, which become less relevant during diastole. Moreover, inside the domain Ω_M the two numerical solution are in excellent agreement at each time step.

This result is coherent with the enforced splitting strategy. Indeed, using the explicit version of Algorithm 4.1 we are imposing at each time-step t^{n+1} the following boundary condition in the Navier-Stokes sub-problem:

$$\begin{aligned}-p_{AC}^{n+1} + \mu(\nabla \mathbf{u}_{AC}^{n+1} + \nabla \mathbf{u}_{AC}^{n+1^T})\mathbf{n} \cdot \mathbf{n} = &- \frac{1}{|\Omega_M^j|} \int_{\Omega_M^j} p_{M,1}^n \, d\mathbf{x} \\ &- \frac{1}{\alpha^j} \int_{\Gamma^j} \mathbf{u}_{AC}^n \cdot \mathbf{n} \, d\gamma \qquad \text{on } \Gamma^j,\end{aligned} \tag{5.6}$$

which depends on the pressure in the first Darcy compartment ($p_{M,1}$) and the flux through the coronary outlets ($\int_{\Gamma^j} \mathbf{u}_{AC} \cdot \mathbf{n} \, d\gamma$) evaluated at t^n, thus introducing an error. As we have already mentioned, $p_{M,1}$ presents a temporal profile similar to the CBF profile (see Fig. 5.4b), thus the error is more significant during systole, when the variations between time-steps are bigger.

On the other hand, the Darcy solution in the first compartment depends on the flux through the coronary outlets, namely:

$$-\nabla \cdot (\mathbf{K}_1 \nabla p_{M,1}^{n+1}) = \sum_{j=1}^{N^j} \frac{\chi_{\Omega_M^j}}{|\Omega_M^j|} \int_{\Gamma^j} \mathbf{u}_{AC}^{n+1} \cdot \mathbf{n}\, d\gamma - \beta_{1,2}(p_{M,1}^{n+1} - p_{M,2}^{n+1}) \quad \text{in } \Omega_M, \tag{5.7}$$

where the NS velocity $\mathbf{u}_{AC}^{n+1}$ contains an error related to the explicit boundary condition (5.6). Thus, an error is introduced also in the computation of $p_{M,1}$, but it is less significant with respect to the error that would be introduced by an explicit formulation of (5.7) where $\mathbf{u}_{AC}$ is evaluated at t^n.

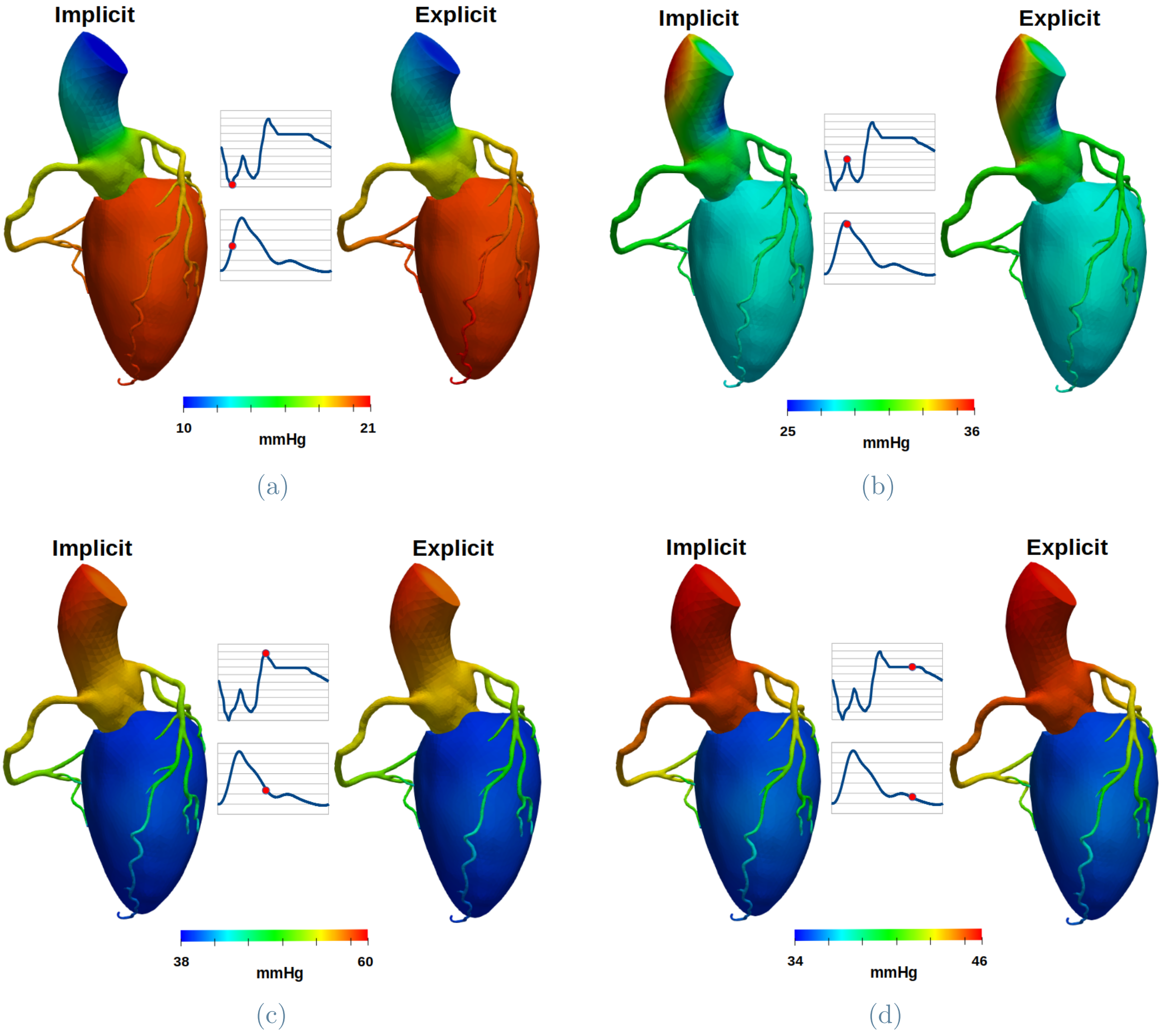

(a) (b) (c) (d)

Figure 5.5: Comparison between implicit and explicit NS pressure p_{AC} and first Darcy compartment pressure $p_{M,1}$ for different time instants: (a) $t = 0.06$ $[s]$, minimum CBF in systole; (b) $t = 0.14$ $[s]$, peak aortic flow rate in systole; (c) $t = 0.28$ $[s]$, peak CBF in early diastole (d) $t = 0.48$ $[s]$, mid-late diastole. *Coupled perfusion model: Implicit vs Explicit splitting*

We can compute the relative error of the explicit algorithm with respect to the implicit one in terms of L^2 norm of p_{AC} and $p_{M,1}$ in Ω_{AC} and Ω_M, respectively. The results are shown in Figure 5.6.

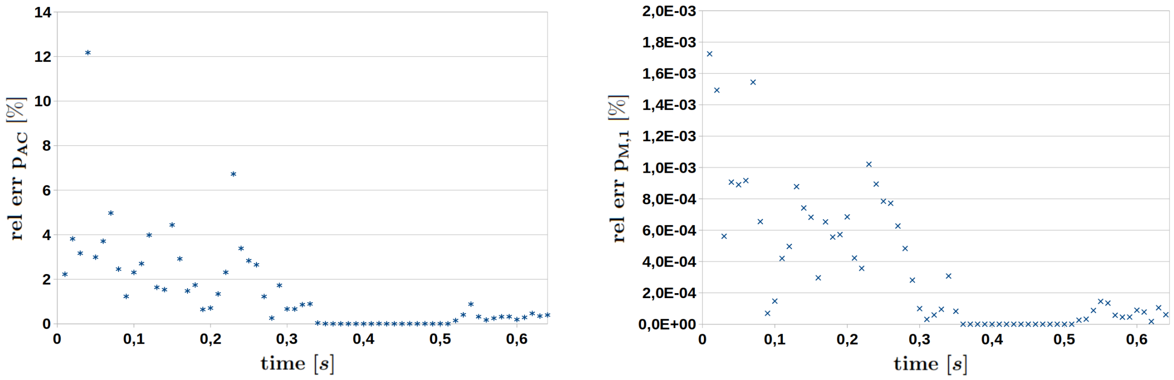

(a) (b)

Figure 5.6: Relative error of the explicit strategy with respect to the implicit one in terms of the L^2 norms of p_{AC} (Fig. 5.6a) and $p_{M,1}$ (Fig. 5.6b). *Coupled perfusion model: Implicit vs Explicit splitting*

Figure 5.6 shows that the relative error for p_{AC} is great during systole, it becomes almost zero once the plateau of the CBF signal is reached and it slightly increases again in late diastole, since CBF starts decreasing. In particular, the mean error during systole is about 3%, whereas during diastole the mean error is about 0.7%. Moreover, the relative error for $p_{M,1}$ shows a similar trend, but the error is much smaller (always smaller than 0.002%).

In Figure 5.7 we report for each time-step the number of iterations that the implicit algorithm needs in order to reach convergence. A clear trend cannot be identified from the chart, but the number of iterations is higher during the first part of the heartbeat, when large variations of CBF are experienced, in accordance to trend of the explicit algorithm discussed above. The average number of iterations during an heartbeat is ~ 3.39.

Therefore, the explicit version of Algorithm 4.1 is stable in real geometries and provides accurate results during diastole, particularly inside the myocardium (Ω_M), while decreasing the computational cost (1 vs 3.39 iterations). On the other hand, the implicit version should be preferred when one needs to have good accuracy also during systole inside aortic root and epicardial coronaries (Ω_{AC}).

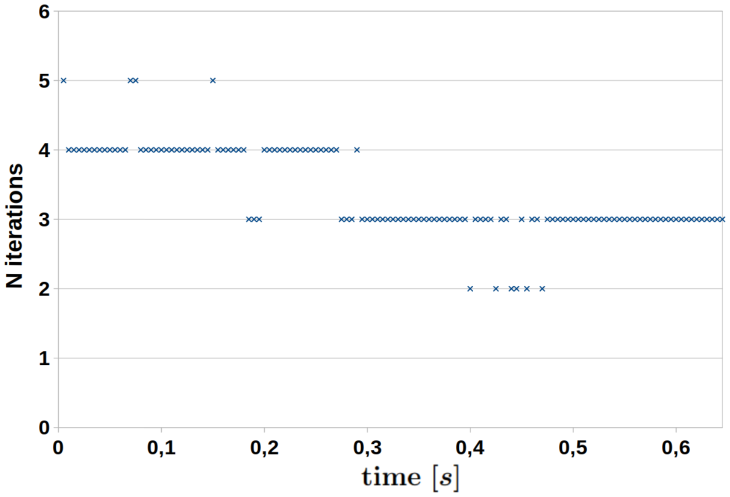

Figure 5.7: Number of iterations needed for the implicit algorithm in order to reach convergence. *Coupled perfusion model: Implicit vs Explicit splitting*

5.3.2. Analysis of parameters impacting the pressure fields

As already mentioned, the temporal profile of the pressure fields follow the CBF profile (Fig. 5.4b). Indeed, in our multi-physics model, inherited from [69], we are using constant parameters while not considering vessel compliance and myocardial contraction, thus the time variation of the pressure gradients inside the myocardium and epicardial coronary arteries only depend on the time variation of CBF. Since in [69] they aimed at producing accurate perfusion results during diastole (when 80% of left CBF occurs), then in first approximation they accepted this inaccurate description of the pressure waveform. Moreover, also the absolute pressure values during diastole are under estimated, but in order to get accurate perfusion results the model only needs to provide an accurate description of the pressure gradients between different myocardial compartments, according to the definition of $\mathrm{MBF}_{\mathrm{COMP}}$ in (5.1). Thus, also this under estimation was accepted in [69] since it does not compromise the perfusion results.

In order to get more physiologically consistent temporal profiles of the pressure fields, myocardial contraction should be considered in future studies. On the other hand, let us present here two strategies, based on a modification of the baseline parameters, aimed at increasing the absolute pressure values:

- decreasing by 10-fold the drain coefficient γ, thus using $\gamma = 10^{-5}$ $[1/Pa \cdot s]$;
- increasing the value of venous pressure p_{veins} by two times, thus using $p_{veins} = 45$ $[mmHg]$.

In Figure 5.8 we report the space averaged pressure fields inside the aortic root and each myocardial compartment together with the constant value of the venous pressure in three scenarios: considering the baseline values of the parameters and both strategies introduced above. Notice that the average pressure in the aortic root is computed as the mean value of the space averaged pressures on the aortic inlet and outlet sections.

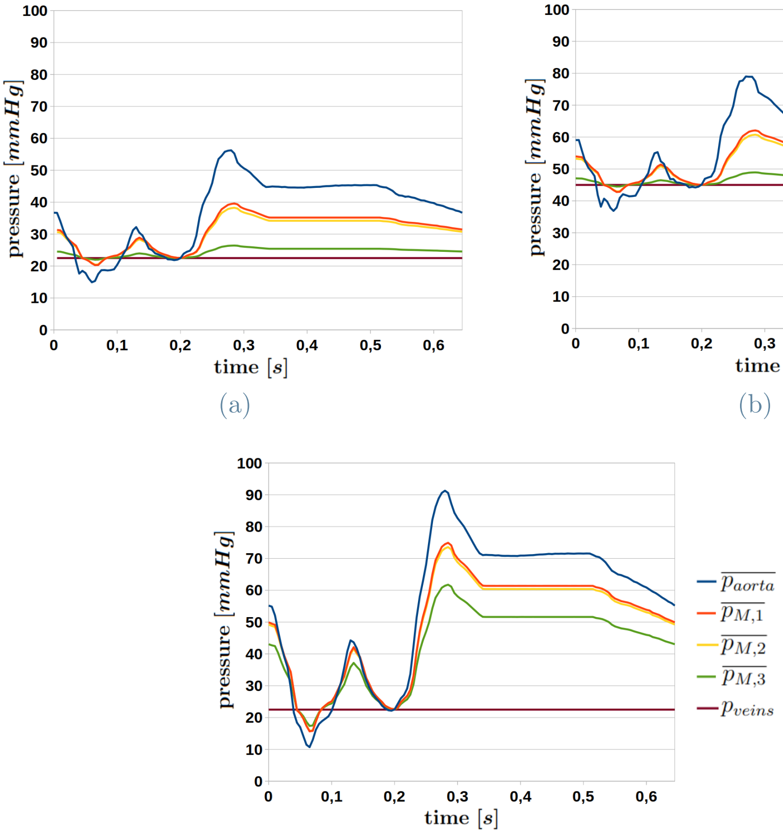

(a)

(b)

(c)

Figure 5.8: Average-in-space pressures inside aortic root and each Darcy compartment together with the venous pressure considering 3 different scenarios: (a) baseline parameters values; (b) $p_{veins} = 45$ $[mmHg]$; (c) $\gamma = 10^{-5}$ $[1/Pa \cdot s]$. All three charts have the same label, reported only in Fig. 5.8c. *Coupled perfusion model: Pressure analysis*

Figure 5.8 shows that the increase of the venous pressure acts as a rigid upward translation of the pressure fields, whereas decreasing the drain coefficient leads to a higher pressure gradient between the last Darcy compartment and the venous system. Following both strategies we end up with more physiologically consistent absolute pressure values inside the aortic root during diastole (about 70 $[mmHg]$). However, decreasing γ we get a great variability of the pressure field inside the last Darcy compartment, related to capillaries. Thus, an increase of p_{veins} has to be preferred, since it allows us to obtain more accurate absolute pressure value while keeping the pressure inside the capillaries almost constant during an heartbeat, as we expect.

It is important to highlight that the Darcy inter-compartment pressure gradients are not influenced by a change of either p_{veins} or γ. Thus, changing the values of such parameters does not have an impact on the computation of $\mathrm{MBF}_{\mathrm{COMP}}$, thanks to its definition in (5.1).

Remember that in order to get physiological pressure values during systole we should account for myocardial contraction, either by using time-dependent parameters for our model or by considering a poro-elastic modeling of the myocardium.

5.3.3. Cardiac output change: rest vs stress conditions

In this last analysis, we aim at showing that changing the flow rate inside the aortic root does not have an impact on the computation of the MBF maps, as long as the total flow entering the coronary circulation is the same.

In particular, we consider the baseline values of the parameters and we impose in the coronary circulation the flow rate profile shown in Figure 5.4b as the difference between the flow rate imposed on the aortic inlet and outlet sections, as explained in the introduction to this section. We compare the numerical solutions obtained in two scenarios:

- assigning on the aortic outlet the flow rate profile shown in Figure 5.4a, which guarantees a mean cardiac output (CO) of ~ 15 $[L/min]$ during an heartbeat (stress conditions);
- scaling the flow rate profile on the aortic outlet section (Fig. 5.4a) in order to guarantee a mean cardiac output of ~ 5 $[L/min]$ during an heartbeat (rest conditions).

Let us first analyze the impact that a change in aortic flow rate has on the pressure distribution across the computational domains. To this purpose, in Figure 5.9 we report p_{AC} together with $p_{M,1}$ in each scenario considering two different time-steps.

Figure 5.9a shows a time-instant during early systole. Since the flow rate inside the aortic root is increasing, then there is a positive pressure gradient between aortic inlet and outlet sections. Such pressure gradient is greater if we account for stress conditions (CO about 15 $[L/min]$) because the flow is experiencing a greater acceleration with respect to the rest conditions cardiac output (CO about 5 $[L/min]$). Moreover, notice that the pressure fields are almost equivalent inside the epicardial coronary arteries and myocardium, thus changing the aortic flow rate has an impact on the pressure distribution only inside the

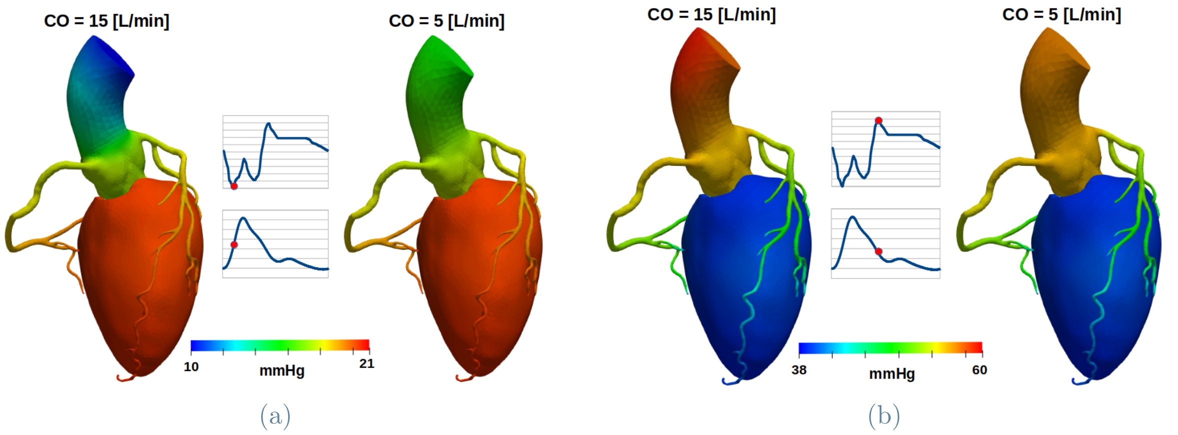

(a) (b)

Figure 5.9: Distribution of p_{AC} and $p_{M,1}$ considering a change in cardiac output, for different time-steps: (a) $t = 0.06$ $[s]$, minimum CBF in systole; (b) $t = 0.28$ $[s]$, peak CBF in early diastole. CO=cardiac output. *Coupled perfusion model: Change in cardiac output*

aorta. Analogous considerations can be made by analyzing Figure 5.9b, in this case the flow is decelerating, being an instant during diastole, thus the pressure gradient in the aortic root is negative.

In Figure 5.10 we show, for different time-steps, the computed MBF_{COMP} maps, together with the relative error between the two considered strategies, that is the relative error of the rest conditions cardiac output with respect to the stress conditions one.

Figure 5.10 shows that the MBF_{COMP} maps computed in both scenarios are in excellent agreement with each other for each time-step. In particular, the relative error is greater during systole, since the biggest variation in aortic flow rate are experienced during this period, and is smaller than 1.6% everywhere, for each considered time-step. Therefore, we conclude that the computation of MBF_{COMP} maps is not influenced by a change in aortic flow rate.

5.4. Consistency test on the numerical results: MBF maps

In this section we aim at validating our multi-physics computational model for myocardial perfusion by exploiting patient-specific clinical data, such as MBF_{CTP} obtained from stress-CTP images (see Section 5.1).

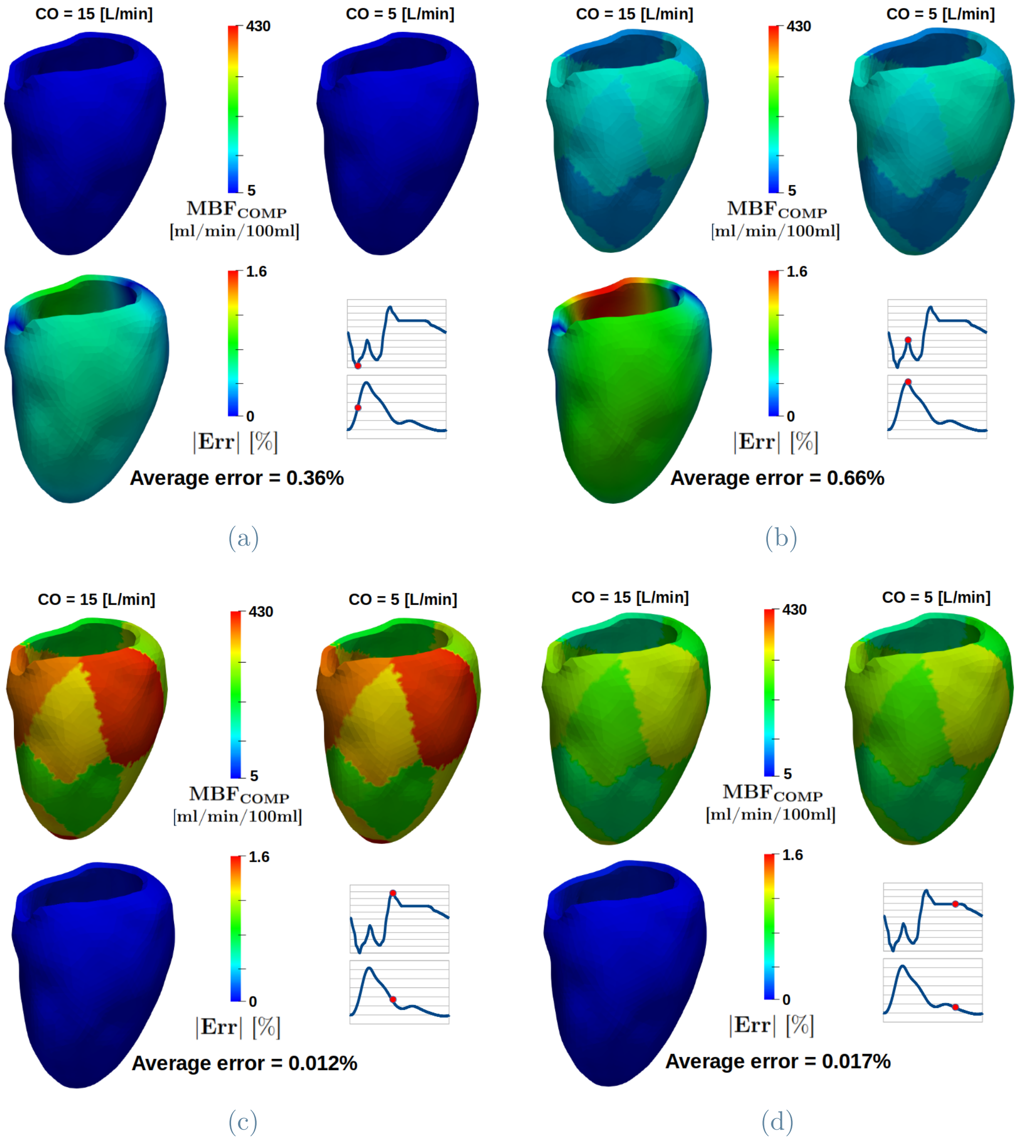

(a) (b) (c) (d)

Figure 5.10: Comparison between $\mathrm{MBF_{COMP}}$ with rest and stress cardiac output, together with distributed and average-in-space relative errors, for different time instants: (a) $t = 0.06$ $[s]$, minimum CBF in systole; (b) $t = 0.14$ $[s]$, peak aortic flow rate in systole; (c) $t = 0.28$ $[s]$, peak CBF in early diastole (d) $t = 0.48$ $[s]$, mid-late diastole. *Coupled perfusion model: Change in cardiac output*

In particular, we compare the numerical results with clinical data in terms of average perfusion MBF_*^{avg} and $\overline{\mathrm{MBF}}_*$ global maps (*=CTP, COMP), defined in Section 5.1. To this purpose, let us define the relative error in each perfusion region as:

$$Err^j = \frac{\mathrm{MBF}^j_{\mathrm{COMP}} - \mathrm{MBF}^j_{\mathrm{CTP}}}{\mathrm{MBF}^j_{\mathrm{CTP}}}, \tag{5.8}$$

the definitions of MBF_*^j (*=CTP, COMP) can be found in Section 5.1.

Exploiting the definition of Err^j we can introduce the global error map, namely:

$$|Err(\mathbf{x})| = \sum_{j=1}^{N^j} |Err^j| \chi_{\Omega_M^j}(\mathbf{x}), \tag{5.9}$$

where $\chi_{\Omega_M^j}$ denotes the characteristic function of the perfusion region Ω_M^j.

First, we present the results obtained after the stress *a priori* parameter adjustment, then we also consider the patient-specific optimization of the parameters $\beta_{i,k}$ (Section 5.2).

In all the numerical simulations we considered the solution of Problem 4.3 by following the implicit iterative splitting strategy presented in Algorithm 4.1. The baseline values of the model parameters, presented in Section 5.3, are adopted. Moreover, the Finite Element library $life^x$ (`https://lifex.gitlab.io/`) is used to perform the simulations and each continuous sub-problem in Problem 4.3 is discretized following the strategies presented in Section 4.3. In particular, we considered a semi-implicit Backward Difference Formulation of order 1 for time discretization using $\Delta t = 5 \times 10^{-3}$ $[s]$, P1/P1 Finite Elements with a SUPG-PSPG stabilization for the NS sub-problem and Q1 Finite Elements for the multi-compartment Darcy sub-problem in primal formulation.

We prescribed on the aortic inlet and outlet sections equivalent boundary conditions to the ones introduced in Section 5.3. In particular, using a Dirichlet condition on the aortic inlet and a defective flow rate condition on the aortic outlet, we guarantee that the mean cardiac output is about 15 $[L/min]$, in order to account for stress conditions, and that the total flow rate entering the coronary circulation presents the temporal profile shown in Figure 5.4b for patient P2, where the peak value of CBF in a heartbeat coincides with the patient-specific CBF_{MBF} data reported in Table 5.1. Each temporal profile was scaled in time in order to match the patient-specific HR (Table 5.2).

Since the patient-specific CBF_{MBF} is reached at the peak of the CBF profile, then we compare the numerical results with clinical data at the time-step of the peak.

5.4.1. Computation of MBF maps after stress *a priori* parameter adjustment

Let us present here the results obtained after the stress *a priori* parameter adjustment. Notice that, in this case, we are only exploiting the clinical MBF_{CTP} maps in order to impose a flow rate inside the coronary circulation that matches the patient-specific

$\mathrm{CBF}_{\mathrm{MBF}}$ (Table 5.1) at the peak value. In future studies patient-specific CBF can be obtained by measuring the coronary flow at rest (e.g. by a EchoColorDoppler) and by adjusting its value in order to account for stress conditions, thus avoiding the need of stress-CTP acquisition.

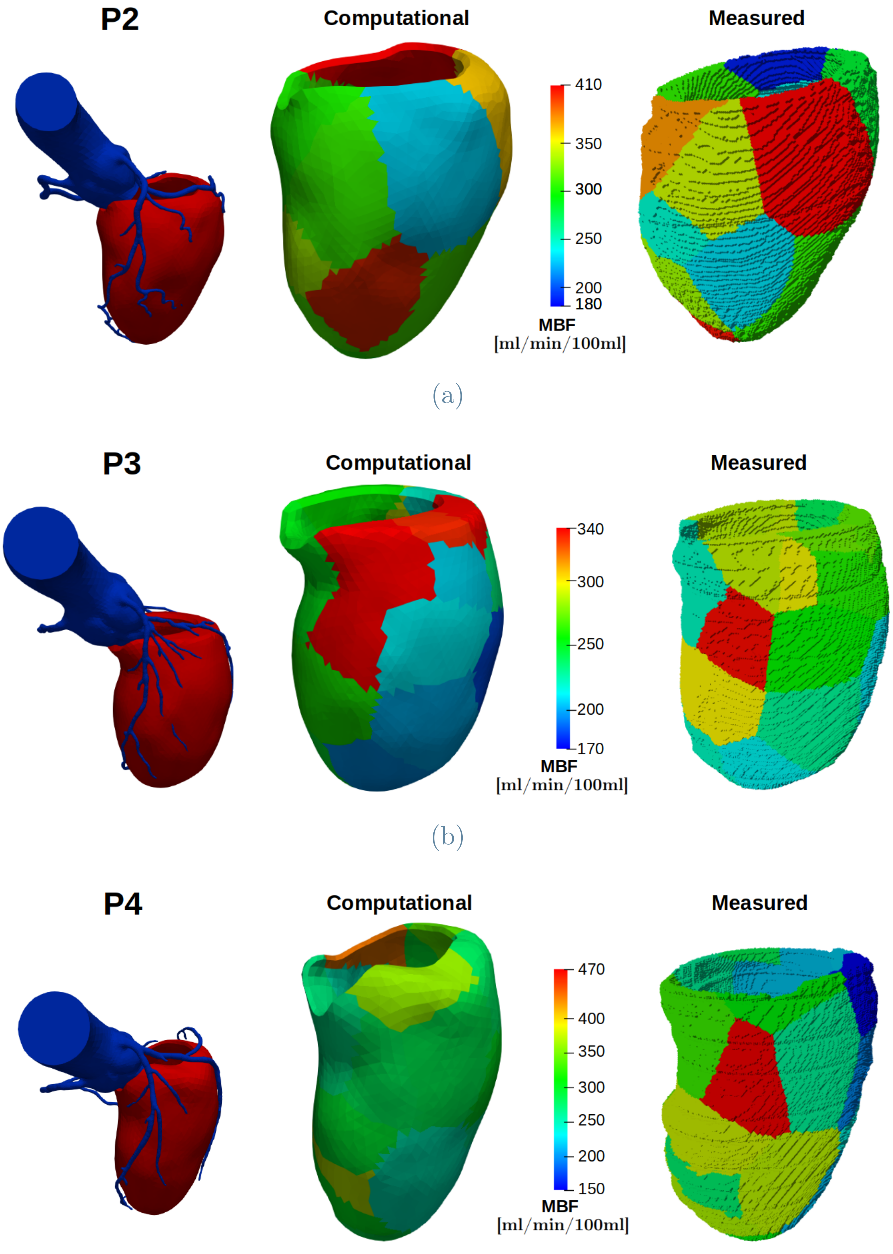

(a)

(b)

(c)

Figure 5.11: $\overline{\mathrm{MBF}}_{COMP}$ and $\overline{\mathrm{MBF}}_{CTP}$ for each considered patient after stress *a priori* parameter adjustment. *Coupled perfusion model: MBF maps*

In Figure 5.11 $\overline{\mathrm{MBF}}_{COMP}$ and $\overline{\mathrm{MBF}}_{CTP}$ are shown for each considered patient. Although presenting MBF values in the same range, $\overline{\text{MBF}}_{COMP}$ and $\overline{\text{MBF}}_{CTP}$ differ in terms of MBF distribution, suggesting that an appropriate estimation of the parameters $\beta_{i,k}$ is needed in order to obtain an accurate MBF pattern.

In Figure 5.12 we report the relative error global maps defined in (5.9). The relative error locally reaches values greater than 90% for patient P2 and P4, whereas for patient P3 the error is smaller, but the model still does not provide accurate perfusion results.

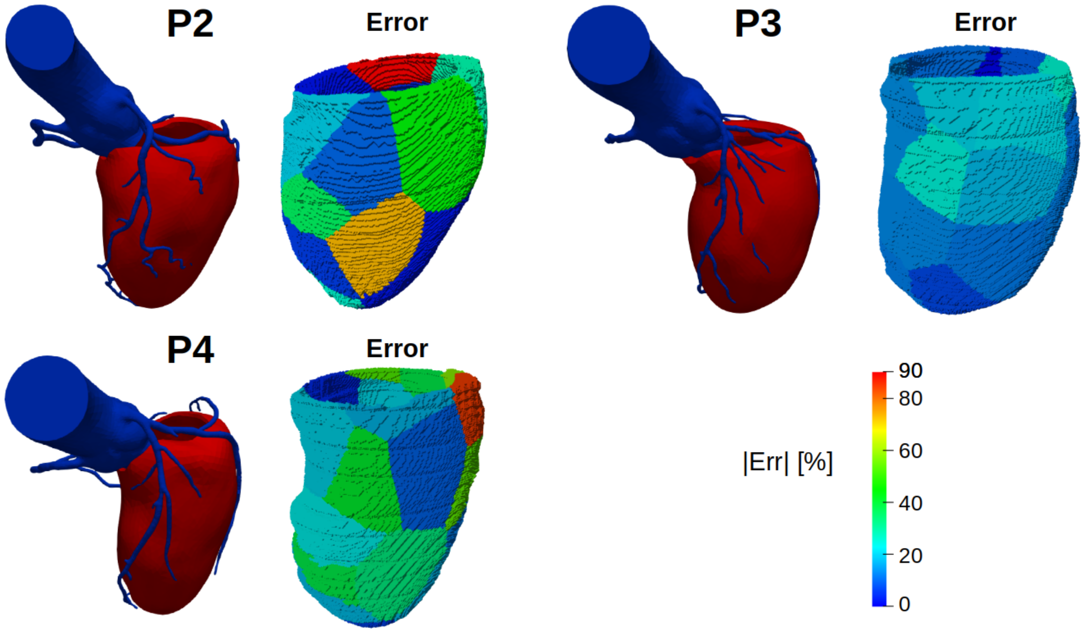

Figure 5.12: $|Err(\mathbf{x})|$ for each patient after stress *a priori* parameter adjustment. *Coupled perfusion model: MBF maps*

Moreover, we can compute the average MBF in the myocardium from numerical results and compare it with the the average MBF obtained from MBF_{CTP}. We report the results for each patient in Table 5.3 together with the average-in-space of the relative error $|Err(\mathbf{x})|$ and its standard deviation between perfusion regions. Both the average relative error and the standard deviation were computed using as weight the volume of the corresponding perfusion region. The table shows an excellent agreement in terms of average MBF between the numerical results and the clinical data. On the other hand, the average relative errors are always greater than 12% and the standard deviations show a great variability between perfusion regions, particularly for patient P2 and P4, as we expected from Figure 5.12.

We conclude that the stress *a priori* parameter adjustment, which includes the use of a patient-specific CBF peak value, is enough to get accurate results in terms of average perfusion, which can give a first indication on whether a patient experiences perfusion

Id	$\mathrm{MBF}^{avg}_{\mathrm{CTP}}$ $[ml/min/100ml]$	$\mathrm{MBF}^{avg}_{\mathrm{COMP}}$ $[ml/min/100ml]$	a priori $\lvert Err\rvert_{avg}$ [%]
P2	314.95	314.00	22.03 ± 30.34
P3	246.75	246.15	12.31 ± 5.22
P4	281.38	280.74	29.38 ± 23.50

Table 5.3: Average MBF in the myocardium from both numerical and clinical data together with the average-in-space of the relative error $|Err(\mathbf{x})|$ after *a priori* parameter adjustment.

defects. Nonetheless, in order to match the spatial distribution of MBF inside the left ventricle we need appropriate estimates of the parameters $\beta_{i,k}$, which regulate the MBF pattern. Therefore, different strategies for the model parameter estimation procedure presented in Section 4.2.3 should be investigated in future studies in order to get accurate perfusion results without relying on stress-CTP images, so that the predictive nature of the computational model can be exploited. As an example, the surrogate intramural network generated for the estimation of the parameters can be refined by leveraging anatomical human data or exploiting machine learning techniques.

5.4.2. Computation of MBF maps after patient-specific optimization

Finally, let us present the results obtained after the patient-specific optimization of the parameters $\beta_{i,k}$. Remember that to perform such optimization we exploit the global map $\overline{\mathrm{MBF}}_{CTP}$, which comes from stress-CTP images. This is not ideal, since we would like to obtain accurate perfusion results only relying on non-invasive techniques in order to propose our computational model as an alternative to the stress protocol. Nonetheless, we use the results after patient-specific optimization in order to show that our computational model is able to provide accurate perfusion results as long as the parameters are appropriately estimated.

We can perform an analogous analysis to the one presented for the *a priori* adjustment. In particular, in Figure 5.13 we report $\overline{\mathrm{MBF}}_{COMP}$ and $\overline{\mathrm{MBF}}_{CTP}$ after patient-specific parameter optimization for each considered patient. The figure shows, for every patient, an excellent agreement between the two global maps in terms of MBF spatial distribution in the left ventricle, suggesting that a proper estimation of the parameters $\beta_{i,k}$ is necessary to obtain locally accurate perfusion results.

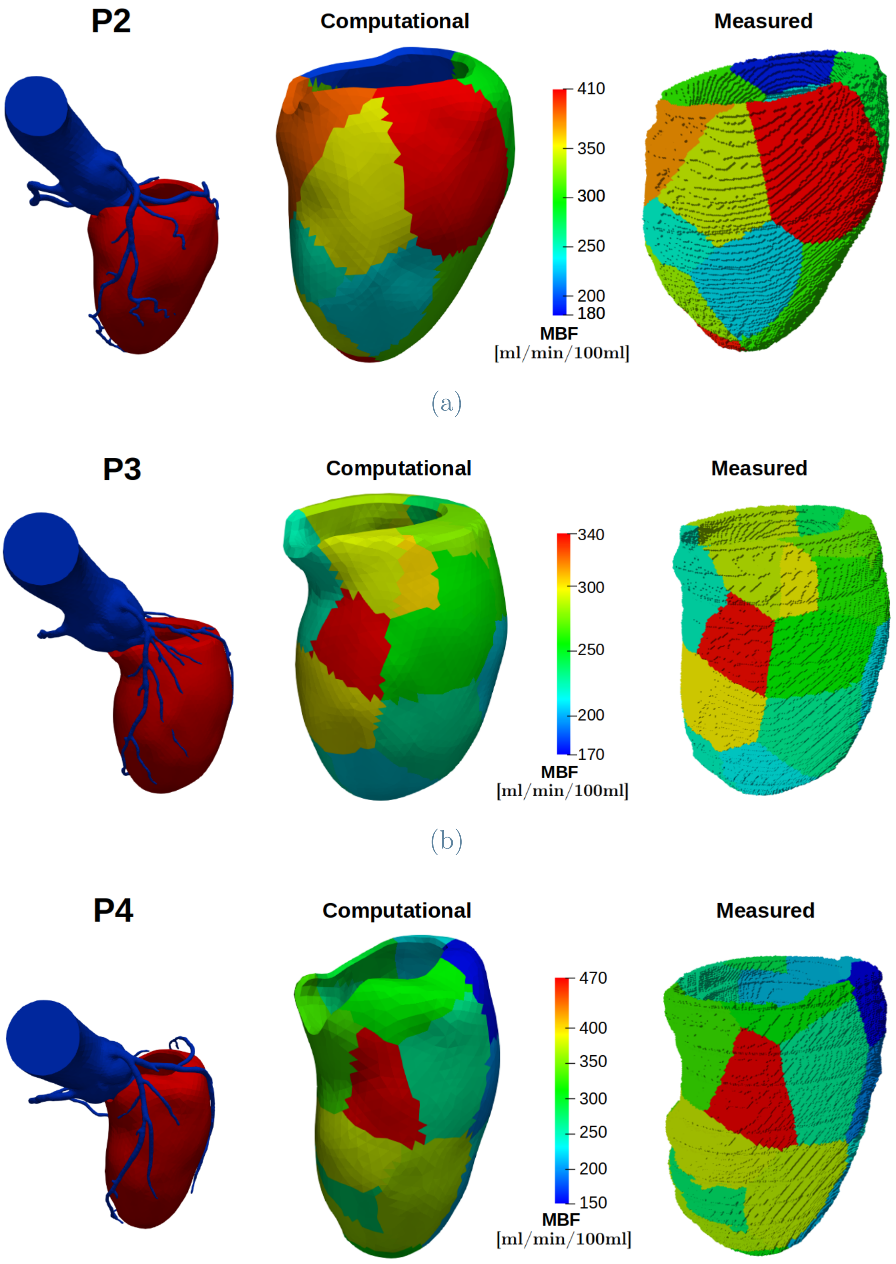

(a)

(b)

(c)

Figure 5.13: $\overline{\text{MBF}}_{COMP}$ and $\overline{\text{MBF}}_{CTP}$ for each considered patient after patient-specific parameter optimization. *Coupled perfusion model: MBF maps*

The relative error maps $|Err|$, defined in (5.9), are shown for each patient in Figure 5.14. The relative errors greatly decrease after the patient-specific optimization, being locally smaller than 5% for every patient.

Again, we report in Table 5.4 the average MBF in the myocardium computed both from numerical results and clinical data together with the average-in-space of the relative error

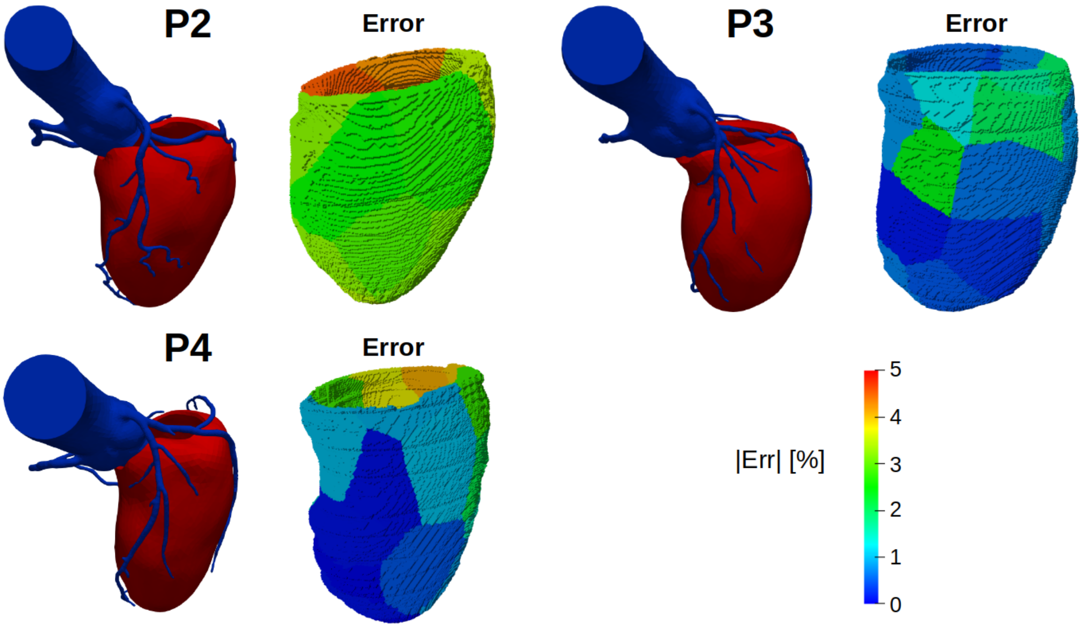

Figure 5.14: $|Err(\mathbf{x})|$ for each patient after patient-specific parameter optimization. *Coupled perfusion model: MBF maps*

$|Err(\mathbf{x})|$. There is still an excellent agreement between the average perfusion values, as in the case of the *a priori* adjustment. Moreover, the average error is always smaller than 4% and the variability between different perfusion is significantly smaller than in the previous case.

Id	$\text{MBF}^{avg}_{\text{CTP}}$ $[ml/min/100ml]$	$\text{MBF}^{avg}_{\text{COMP}}$ $[ml/min/100ml]$	patient-specific $|Err|_{avg}$ [%]
P2	314.95	313.89	3.47 ± 0.66
P3	246.75	246.15	0.77 ± 0.54
P4	281.38	280.63	1.51 ± 1.17

Table 5.4: Average MBF in the myocardium from both numerical and clinical data together with the average-in-space of the relative error $|Err(\mathbf{x})|$ after patient-specific parameter optimization.

We conclude that the patient-specific parameter optimization greatly improves the performance of the computational model regarding the computation of MBF maps under stress conditions. In particular, this is a demonstration that our model is able to provide accurate perfusion results as long as an appropriated estimation of the parameters is performed. Notice that, as already mentioned, proposing a new procedure for the estimation of the model parameters in rest conditions, either by modifying the generation of the surrogate intramural network or by applying different strategies to extract fluid dynamics information on the intramural network, is of utmost importance for future studies. So that one could obtain accurate perfusion results only relying on non-invasive techniques such as cCTA and EchoColorDoppler.

5.5. Final Remarks

Novelty of this work:

- This is the first occurrence of a computational model for myocardial perfusion, providing a complete 3D description of blood dynamics from the aortic root to the cardiac tissue, applied and calibrated using patient-specific clinical data.

Take home messages:

- the explicit version of the splitting strategy proposed in [69] is stable and overall accurate in patient-specific geometries. The implicit version should be preferred when one needs great accuracy inside aortic root and epicardial coronary arteries during systole;
- the coupled model is able to describe physiological features of myocardial perfusion, such as the loss of pulsatility in the microvasculature, retrograde flow and appropriate pressure gradients, with the only limitations on the magnitude and waveform of the pressure fields. The accuracy of the pressure waveform can be improved by accounting for myocardial contraction, either empirically by using time-dependent model parameters or by considering a poro-elastic modelling approach for the myocardium. Whereas, more accurate absolute pressure values can be achieved with a new calibration of the parameters, as shown in Section 5.3.2 in the case of γ and p_{veins};
- the coupled model for myocardial perfusion is able to provide accurate perfusion results in terms of MBF maps as long as an appropriate estimation of the model parameters is performed. In particular, a correct estimation of the patient-specific CBF allows us to obtain accurate results in terms of average MBF inside the myocardium, whereas an appropriate estimation of the parameters $\beta_{i,k}$ is necessary to obtain locally accurate perfusion results;
- concerning MBF maps, the accuracy of the numerical results can be improved by proposing a new strategy for the generation of the surrogate intramural network, either by including anatomical data in the generation process or by exploiting machine

learning techniques;

- the inclusion of the aortic root inside the coupled model for myocardial perfusion leads to an automatic estimation of flow partition between left and right coronary arterial trees, which was empirically estimated in [70] exploiting the volumes of each perfusion region. We think that this feature can provide a systematic improvement in pathological conditions since flow partition should be affected by the presence of a stenosis, thus an empirical estimation of fluid partition based only on the volumes of the perfusion regions would be inaccurate.

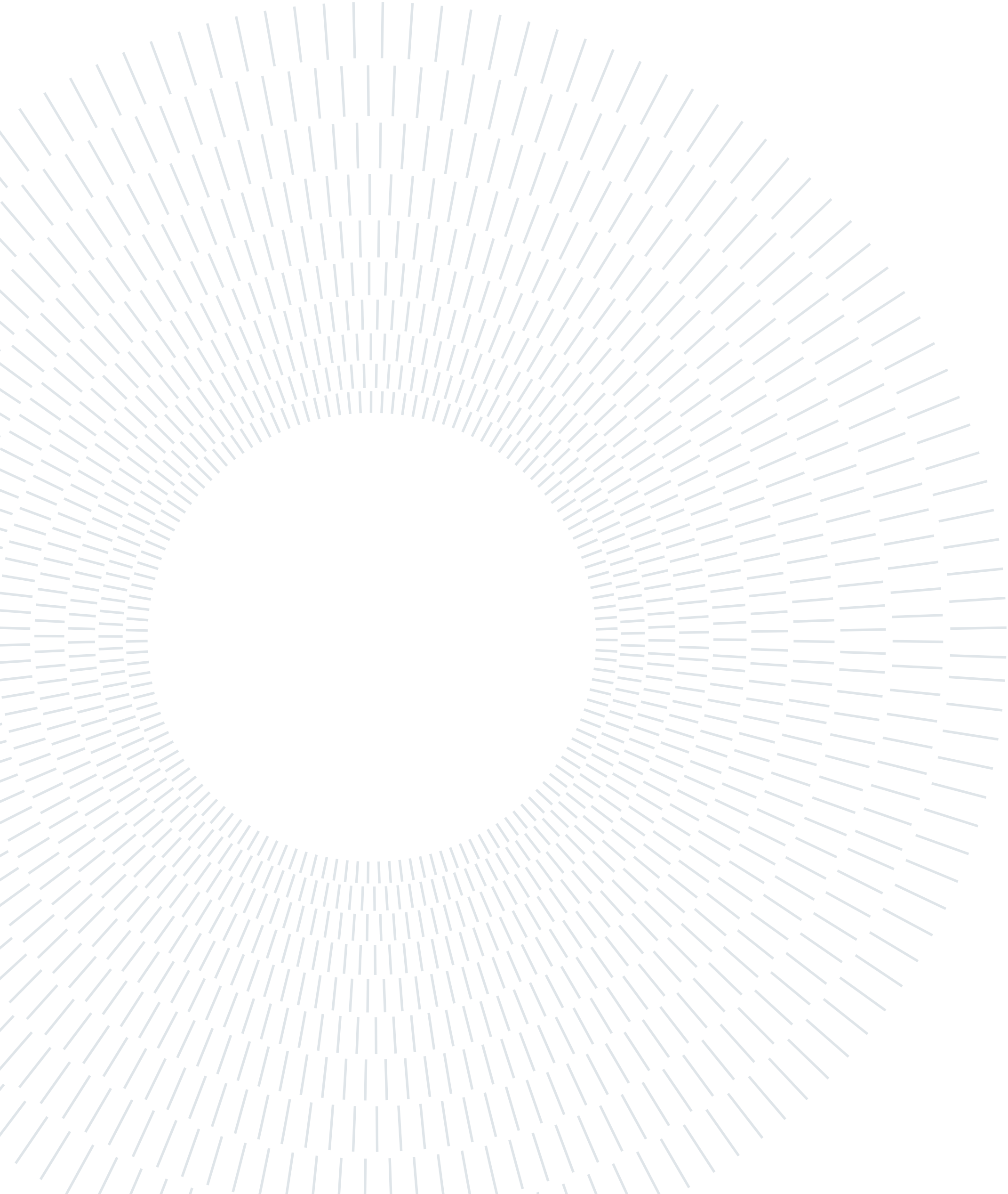

6 | Conclusions

The aim of this thesis project was to increase the upstream capabilities of an existing computational model for myocardial perfusion [69] by including the aortic root inside the computational domain where the model is numerically solved and to assess the reliability of the new modeling framework using patient-specific clinical data. In particular, we investigated the performance of the model regarding the prediction of patient-specific myocardial blood flow (MBF) maps under induced stress conditions for three healthy patients.

To the best of our knowledge, for the first time in literature a computational model, providing a complete three-dimensional description of blood dynamics from the aortic root to the cardiac microvasculature, is applied in patient-specific geometries and calibrated with clinical data.

Let us summarize the main contributions of this work:

1. We proposed practical and flexible strategies for the generation of a computational mesh on the reconstructed anatomical geometries of aortic root and epicardial coronary arteries, using the open-source software VMTK [77, 94]. The generated mesh provides an accurate description of the geometrical features of the coronary circulation, accounting for its different length scales, while guaranteeing an affordable computational cost for running numerical simulation inside the mesh.

2. We introduced a computational model for hemodynamics inside the aortic root and epicardial coronary arteries based on the 3D formulation of the Navier-Stokes (NS) equations. In particular, due to the chaotic spatial velocity distribution inside the ascending aorta, a defective flow rate condition is prescribed on the outlet of the aortic root, whereas classical Dirichlet and Neumann conditions are imposed on the aortic inlet and coronary outlet boundaries, respectively.

3. We implemented the Lagrange multipliers method for the prescription of defective flow rate boundary conditions in a Navier-Stokes problem [97, 98] on the Finite Element Library $life^x$ (`https://lifex.gitlab.io/`), following a parallel computing

approach. The implemented method can be used to perform any fluid dynamics numerical simulation in a generic computational mesh, thus it is not bound to myocardial perfusion or the aortic root. Moreover, we addressed the numerical approximation and the numerical solvers for the augmented NS formulation related to the application of the Lagrange multipliers method.

4. We performed hemodynamics numerical simulations inside a patient-specific aortic root and epicardial coronary arteries as a standalone problem. In particular, we demonstrated that the computational model reported at point 2. is able to provide physiologically consistent numerical results both in terms of pressure and flow distributions. Moreover, the model was applied to study the impact that the Neumann conditions, prescribed on the coronary outlet sections, have on flow partition between left and right coronary networks.

5. We extended the computational coupled model for myocardial perfusion proposed in [69] by numerically solving 3D Navier-Stokes equations inside aortic root and epicardial coronary arteries. The coupling conditions between the NS and the multi-compartment Darcy sub-problems are inherited from [69], whereas suitable boundary conditions had to be formulated for the NS sub-problem on the aortic inlet and outlet boundaries.

6. We applied the computational model for cardiac perfusion reported at point 5. in three patient-specific geometries, the clinical data were provided by Monzino Cardiology Centre in Milan. In particular, we demonstrated that an explicit splitting strategy for solving the monolithic coupled problem is stable and accurate in real geometries. Moreover, we studied different scenarios to understand their impact on the numerical results.

7. We investigated the reliability and the accuracy of the computational multi-physics model in reproducing patient-specific MBF maps starting from coronary computed tomography angiography (cCTA) images.

Thanks to the inclusion of the aorta, the mathematical and numerical model for hemodynamics inside aortic root and epicardial coronary arteries can provide meaningful insights on coronary blood flow (CBF). Indeed, the model can be applied in different patient-specific geometries in order to understand the impact of the geometrical features on the blood flow distribution inside the coronary circulation, specially in case of coronary artery diseases (CAD). Moreover, 3D blood dynamics simulations can be exploited to quantify the pressure losses in presence of a stenosis and to compute wall shear stresses, which is a key indicator for the development of atherosclerotic plaques. Finally, the inclusion of the aorta allows us to consider aortic valve dynamics in order to evaluate their impact on CBF.

Concerning the multi-physics computational coupled model for myocardial perfusion, numerical simulations provide meaningful perfusion results in pharmacologically induced stress conditions. The model is able to describe physiological features of myocardial perfusion, such as the loss of pulsatility in the microvasculature, retrograde flow and appropriate pressure gradients, with the only limitations on the magnitude and waveform of the pressure fields. Indeed, pressure in the proximal vessels and pressure jumps between compartments are slightly underestimated, possibly due to the assumptions of a rigid domain. More physiological results in terms of pressure fields could be achieved by accounting for myocardial contraction, either empirically by introducing time-dependent model parameters or by considering a poro-elastic modeling of the myocardium.

Regarding the computation of MBF maps, the results of the new computational model, which includes the aortic root, are in line with the results obtained in [70] using the model proposed in [69], which only considers the epicardial coronary arteries, thus demonstrating that the aortic root was included correctly inside the model.

Indeed, both in [70] and in this work, after the *a priori* parameter adjustment, the model is able to provide overall good level of agreement with respect to clinical maps, specially in terms of average perfusion, even if there are localized regions were the numerical estimation is not very accurate. The in-space averaged relative errors of $\overline{\mathrm{MBF}}_{\mathrm{COMP}}$ with respect to $\overline{\mathrm{MBF}}_{\mathrm{CTP}}$ are smaller than 30% for each considered patient. Nonetheless, the local relative errors can be largely greater than the average value, as suggested by the big standard deviations, thus the accuracy of this *a priori* strategy is limited. In order to improve the performance of the computational model after the *a priori* adjustment, the estimation of the model parameters in rest conditions should be modified. This estimation strictly depends on the surrogate intramural network, thus a proper generation of such network, for example based on machine learning techniques, could greatly improve the numerical perfusion results in terms of MBF distribution.

Moreover, after the patient-specific optimization of the parameters the numerical results are in excellent agreement with clinical data. Indeed, in this case the averaged in space relative errors between the numerical and clinical maps are always smaller than 4% and the variability of the errors in the perfusion regions is drastically decreased. Therefore, we can conclude that our model is able to provide accurate perfusion results as long as an appropriate characterization of the myocardium is performed.

The inclusion of the aorta does not result in significant improvements in terms of patient-specific MBF maps computation. Indeed, regarding the MBF maps, the most significant difference introduced by our model is that the fluid partition between left and right coronary arteries is not empirically set by the user (exploiting the volume of each perfusion region), but it is automatically estimated by the model. Since we are considering only the coronary arteries perfusing the left ventricle, then such difference does not have a relevant impact on MBF maps computation. Nonetheless, we think that the inclusion of the aorta could represent a systematic improvement, particularly in pathological cases, where an empirical *a priori* estimation of fluid partition can be inaccurate due to the presence of stenosis.

Moreover, this project represents a first step toward the coupling of myocardial perfusion with ventricular dynamics, such as ventricular electro-mechanics and ventricular ejection. For this reason, this study moves in the direction of a more comprehensive description of the myocardial perfusion process by exploring the model upstream. Additionally, also a downstream extension of the model can be considered in future studies in order to achieve a circular coupling of myocardial perfusion: going from electro-mechanics in the ventricle, to ventricular ejection, to myocardial perfusion, to oxygen exchange in the cardiac capillaries and back to electro-mechanics. Such circular coupled model could be exploited in order to study the impact of perfusion defects on oxygen supply and subsequent propagation of the electrical signal and contraction of the heart muscle, which regulate the cardiac function.

Bibliography

[1] D. U. Silverthorn. *Human physiology: an integrated approach*, volume 34. 2016.

[2] A. M. Quarteroni, A. Manzoni, and C. Vergara. The cardiovascular system: Mathematical modeling, numerical algorithms, clinical applications. Technical Report 38, MOX, 2016.

[3] F. Baldissera and C. A. Porro. *Fisiologia e Biofisica medica*. Poletto, 2009.

[4] W. F. Boron and E. L. Boulpaep. *Medical Physiology: A Cellular and Molecular Approach*. Elsevier Health Science, 2012.

[5] A. G. Goodwill et al. Regulation of coronary blood flow. *Comprehensive physiology*, 7(2):321–382, 2017.

[6] H. Gray, S. Standring, and N. R. Borley. *Gray's anatomy: the anatomical basis of clinical practice*. Churchill Livingstone/Elsevier, 2008.

[7] J. T. Hansen. *Netter's Anatomy Flash Cards - 4th Edition*. Elsevier Health Sciences, 2014.

[8] J. Lee and N. P. Smith. The multi-scale modeling of coronary blood flow. *Annals of Biomedical Engineering*, 40(11):2399–2413, 2012.

[9] Cleveland Clinic. Coronary artery disease. `https://my.clevelandclinic.org/health/diseases/16898-coronary-artery-disease`.

[10] J. A. E. Spaan et al. Visualisation of intramural coronary vasculature by an imaging cryomicrotome suggests compartmentalisation of myocardial perfusion areas. *Medical and Biological Engineering and Computing*, 43(4):431–435, 2005.

[11] E. M. Okun, S. M. Factor, and E. S. Kirk. End-capillary loops in the heart: an explanation for discrete myocardial infarctions without border zones. *Science*, 206(4418):565–567, 1979.

[12] K. E. Barrett et al. Circulation through special regions. In *Ganong's Review of Medical Physiology, 26e*. McGraw-Hill Education, New York, NY, 2019.

[13] A. M. Quarteroni, R. Sacco, and F. Saleri. *Numerical Mathematics*, volume 37. Springer, 2010.

[14] R. M. Lancellotti et al. Large eddy simulations for blood dynamics in realistic stenotic carotids. *International Journal for Numerical Methods in Biomedical Engineering*, 33(11), 2017. e2868.

[15] C. Vergara et al. Large eddy simulations of blood dynamics in abdominal aortic aneurysms. *Medical Engineering & Physics*, 47:38–46, 2017.

[16] M. Domanin et al. Image-based displacements analysis and computational blood dynamics after endovascular aneurysm repair. *Annals of Vascular Surgery*, 69:400–412, 2020.

[17] A. M. Quarteroni et al. Integrated heart—coupling multiscale and multiphysics models for the simulation of the cardiac function. *Computer Methods in Applied Mechanics and Engineering*, 314:345–407, 2017.

[18] J. Lee et al. Multi-physics computational modeling in cheart. *SIAM Journal on Scientific Computing*, 38(3), 2016. C150-C178.

[19] J. Lee et al. Multiscale modelling of cardiac perfusion. In *Modeling the Heart and the Circulatory System*, pages 51–96. Springer International Publishing, 2015.

[20] J. R. Alves et al. Simulation of the perfusion of contrast agent used in cardiac magnetic resonance: A step toward non-invasive cardiac perfusion quantification. *Frontiers in Physiology*, 10, 2019.

[21] D. Chapelle et al. A poroelastic model valid in large strains with applications to perfusion in cardiac modeling. *Computational Mechanics*, 46(1):91–101, 2010.

[22] R. Namani et al. Effects of myocardial function and systemic circulation on regional coronary perfusion. *Journal of Applied Physiology*, 128(5):1106–1122, 2020.

[23] C. A. Taylor, T. A. Fonte, and J. K. Min. Computational fluid dynamics applied to cardiac computed tomography for noninvasive quantification of fractional flow reserve: Scientific basis. *Journal of the American College of Cardiology*, 61(22):2233–2241, 2013.

[24] A. Quarteroni et al. *Mathematical Modelling of the Human Cardiovascular System: Data, Numerical Approximation, Clinical Applications*. Cambridge University Press, 2019.

[25] S. Qin et al. Efficient parallel simulation of hemodynamics in patient-specific ab-

dominal aorta with aneurysm. *Computers in Biology and Medicine*, 136:104652, 2021.

[26] N. R. Pillalamarri et al. Patient-specific computational analysis of hemodynamics in adult pulmonary hypertension. *Annals of Biomedical Engineering*, 49(12):3465–3480, 2021.

[27] S. Sankaran et al. Patient-specific multiscale modeling of blood flow for coronary artery bypass graft surgery. *Annals of Biomedical Engineering*, 40(10):2228–2242, 2012.

[28] A. Coccarelli, A. Prakash, and P. Nithiarasu. A novel porous media-based approach to outflow boundary resistances of 1d arterial blood flow models. *Biomechanics and Modeling in Mechanobiology*, 18(4):939–951, 2019.

[29] J. Kremheller et al. An approach for vascular tumor growth based on a hybrid embedded/homogenized treatment of the vasculature within a multiphase porous medium model. *International Journal for Numerical Methods in Biomedical Engineering*, 35(11):e3253, 2019.

[30] G. S. Kassab, J. Berkley, and Y. C. Fung. Analysis of pig's coronary arterial blood flow with detailed anatomical data. *Annals of Biomedical Engineering*, 25(1):204–217, 1997.

[31] N. Mittal et al. Analysis of blood flow in the entire coronary arterial tree. *American Journal of Physiology. Heart and circulatory physiology*, 289(1), 2005. H439-H446.

[32] Y. Huo and G. S. Kassab. Intraspecific scaling laws of vascular trees. *Journal of the Royal Society, Interface*, 9(66):190–200, 2012.

[33] D. Zinemanas, R. Beyar, and S. Sideman. Effects of myocardial contraction on coronary blood flow: an integrated model. *Annals of Biomedical Engineering*, 22(6):638–652, 1994.

[34] P. H. Bovendeerd et al. Dependence of intramyocardial pressure and coronary flow on ventricular loading and contractility: a model study. *Annals of Biomedical Engineering*, 34(12):1833–1845, 2006.

[35] H. J. Kim et al. Patient-specific modeling of blood flow and pressure in human coronary arteries. *Annals of Biomedical Engineering*, 38(10):3195–3209, 2010.

[36] C. J. Arthurs et al. A mathematical model of coronary blood flow control: simula-

tion of patient-specific three-dimensional hemodynamics during exercise. *American Journal of Physiology. Heart and circulatory physiology*, 310(9), 2016. H1242-H1258.

[37] X. Ge et al. A multi-scale model of the coronary circulation applied to investigate transmural myocardial flow. *International Journal for Numerical Methods in Biomedical Engineering*, 34(10), 2018. e3123.

[38] B. Mao et al. Lumped parameter model based surgical planning for cabg. *Medicine in Novel Technology and Devices*, 2:100014, 2019.

[39] R. Pietrabissa et al. A lumped parameter model to evaluate the fluid dynamics of different coronary bypasses. *Medical Engineering & Physics*, 18(6):477–484, 1996.

[40] J. Jacobs, D. Algranati, and Y. Lanir. Lumped flow modeling in dynamically loaded coronary vessels. *Journal of Biomedical Engineering*, 130(5), 2008.

[41] J. P. Mynard and J. J. Smolich. One-dimensional haemodynamic modeling and wave dynamics in the entire adult circulation. *Annals of Biomedical Engineering*, 43(6):1443–1460, 2015.

[42] R. Namani, G. S. Kassab, and Y. Lanir. Integrative model of coronary flow in anatomically based vasculature under myogenic, shear, and metabolic regulation. *Journal of General Physiology*, 150(1):145–168, 2018.

[43] Z. Duanmu. A patient-specific lumped-parameter model of coronary circulation. *Scientific Reports*, 8, 2018. 874.

[44] N. P. Smith, A. J. Pullan, and P. J. Hunter. An anatomically based model of transient coronary blood flow in the heart. *SIAM Journal on Applied Mathematics*, 62(3):990–1018, 2001.

[45] I. E. Vignon and C. A. Taylor. Outflow boundary conditions for one-dimensional finite element modeling of blood flow and pressure waves in arteries. *Wave Motion*, 39(4):361–374, 2004.

[46] J. P. Mynard and P. Nithiarasu. A 1d arterial blood flow model incorporating ventricular pressure, aortic valve and regional coronary flow using the locally conservative galerkin (lcg) method. *Communications in Numerical Methods in Engineering*, 24(5):367–417, 2008.

[47] J. P. Mynard and J. J. Smolich. Influence of anatomical dominance and hypertension on coronary conduit arterial and microcirculatory flow patterns: a multiscale

modeling study. *American Journal of Physiology. Heart and circulatory physiology*, 311(1), 2016. H11-H23.

[48] J. Lee et al. In silico coronary wave intensity analysis: application of an integrated one-dimensional and poromechanical model of cardiac perfusion. *Biomechanics and Modeling in Mechanobiology*, 15(6):1535–1555, 2016.

[49] I. Sazonov and P. Nithiarasu. A novel, fft-based one-dimensional blood flow solution method for arterial network. *Biomechanics and Modeling in Mechanobiology*, 18(5):1311–1334, 2019.

[50] L. Vera et al. A 1d computer model of the arterial circulation in horses: An important resource for studying global interactions between heart and vessels under normal and pathological conditions. *PLoS One*, 14(8), 2019. Ed. by Markus M. Bachschmid, e0221425.

[51] S. J. Sherwin and H. M. Blackburn. Three-dimensional instabilities and transition of steady and pulsatile axisymmetric stenotic flows. *Journal of Fluid Mechanics*, 533:297–327, 2005.

[52] J. B. Park et al. Computational fluid dynamic measures of wall shear stress are related to coronary lesion characteristics. *Heart*, 102(20):1655–1661, 2016.

[53] R. Torii et al. Mr image-based geometric and hemodynamic investigation of the right coronary artery with dynamic vessel motion. *Annals of Biomedical Engineering*, 38(8):2606–2620, 2010.

[54] E. Kung et al. In vitro validation of patient-specific hemodynamic simulations in coronary aneurysms caused by kawasaki disease. *Cardiovascular Engineering and Technology*, 5(2):189–201, 2014.

[55] J. Murphy and F. Boyle. Predicting neointimal hyperplasia in stented arteries using time-dependant computational fluid dynamics: a review. *Computers in Biology and Medicine*, 40(4):408–418, 2010.

[56] C. Chiastra et al. Computational fluid dynamic simulations of image-based stented coronary bifurcation models. *Journal of the Royal Society, Interface*, 10(84), 2013. 20130193.

[57] J. M. Huyghe and D. H. Van Campen. Finite deformation theory of hierarchically arranged porous solids—I. Balance of mass and momentum. *International Journal of Engineering Science*, 33(13):1861–1871, 1995.

[58] M. D. Sinclair et al. Measurement and modeling of coronary blood flow. *WIREs Systems Biology and Medicine*, 7(6):335–356, 2015.

[59] C. Michler et al. A computationally efficient framework for the simulation of cardiac perfusion using a multi-compartment darcy porous-media flow model. *International Journal for Numerical Methods in Biomedical Engineering*, 29(2):217–232, 2013.

[60] A. N. Cookson et al. A novel porous mechanical framework for modelling the interaction between coronary perfusion and myocardial mechanics. *Journal of Biomechanics*, 45(5):850–855, 2012.

[61] W.J. Vankan et al. Finite element analysis of blood flow through biological tissue. *International Journal of Engineering Science*, 35(4):375–385, 1997.

[62] E. R. Hyde et al. Multi-scale parameterisation of a myocardial perfusion model using whole-organ arterial networks. *Annals of Biomedical Engineering*, 42(4):797–811, 2014.

[63] J. M. Huyghe and D. H. Van Campen. Finite deformation theory of hierarchically arranged porous solids—ii. constitutive behaviour. *International Journal of Engineering Science*, 33(13):1873–1886, 1995.

[64] L. Papamanolis et al. Myocardial perfusion simulation for coronary artery disease: A coupled patient-specific multiscale model. *Annals of Biomedical Engineering*, 49(5):1432–1447, 2021.

[65] J. P. Mynard, D. J. Penny, and J. J. Smolich. Scalability and in vivo validation of a multiscale numerical model of the left coronary circulation. *American Journal of Physiology. Heart and circulatory physiology*, 306(4), 2014. H517-H528.

[66] A. van der Horst et al. Towards patient-specific modeling of coronary hemodynamics in healthy and diseased state. *Computational and Mathematical Methods in Medicine*, pages 1–15, 2013.

[67] D. Sengupta et al. Image-based modeling of hemodynamics in coronary artery aneurysms caused by kawasaki disease. *Biomechanics and Modeling in Mechanobiology*, 11(6):915–932, 2012.

[68] M. Esmaily Moghadam et al. A modular numerical method for implicit 0d/3d coupling in cardiovascular finite element simulations. *Journal of Computational Physics*, 244:63–79, 2013.

[69] S. Di Gregorio et al. A computational model applied to myocardial perfusion in the

human heart: From large coronaries to microvasculature. *Journal of Computational Physics*, 424:109836, 2021.

[70] S. Di Gregorio and C. Vergara et al. Prediction of myocardial blood flow under stress conditions by means of a computational model. *European Journal of Nuclear Medicine and Molecular Imaging*, 49(6):1894–1905, 2022.

[71] S. Di Gregorio. *A multi-physics mathematical and numerical model for the simulation of myocardial perfusion.* PhD thesis, Politecnico di Milano, 2021.

[72] C. Magliaro et al. A manual segmentation tool for three-dimensional neuron datasets. *Frontiers in Neuroinformatics*, 11(36), 2017.

[73] Y. Kano et al. Automatic contour segmentation of cervical cancer using artificial intelligence. *Journal of Radiation Research*, 62(5):934–944, 2021.

[74] R. M. Romarowski et al. Patient-specific cfd modelling in the thoracic aorta with pc-mri–based boundary conditions: A least-square three-element windkessel approach. *International Journal for Numerical Methods in Biomedical Engineering*, 34(11), 2018. e3134.

[75] G. Mistelbauer et al. Semi-automatic vessel detection for challenging cases of peripheral arterial disease. *Computers in Biology and Medicine*, 133:104344, 2021.

[76] E. Jafargholi Rangraz et al. Multi-modal image analysis for semi-automatic segmentation of the total liver and liver arterial perfusion territories for radioembolization. *EJNMMI Research*, 9(1):19, 2019.

[77] L. Antiga et al. An image-based modeling framework for patient-specific computational hemodynamics. *Medical & Biological Engineering & Computing*, 46(11):1097–1112, 2008.

[78] N. Otsu. A threshold selection method from gray-level histograms. *IEEE Transactions on Systems, Man, and Cybernetics*, 9(1):62–66, 1979.

[79] B. Otsu and M. Yazdi. A new optimized thresholding method using ant colony algorithm for mr brain image segmentation. *Journal of Digital Imaging*, 32(1):162–174, 2019.

[80] M. van Eijnatten et al. Ct image segmentation methods for bone used in medical additive manufacturing. *Medical Engineering & Physics*, 51:6–16, 2018.

[81] J. A. Sethian. *Level set methods and fast marching methods: evolving interfaces in*

computational geometry, fluid mechanics, computer vision, and materials science, volume 3. Cambridge university press, 1999.

[82] J. A. Sethian. Fast marching methods. *SIAM Review*, 41(2):199–235, 1999.

[83] M. Savic et al. Lung nodule segmentation with a region-based fast marching method. *Sensors*, 21(5), 2021.

[84] D. Jia and X. Zhuang. Directional fast-marching and multi-model strategy to extract coronary artery centerlines. *Computers in Biology and Medicine*, 108:67–77, 2019.

[85] M. Piccinelli et al. A framework for geometric analysis of vascular structures: Application to cerebral aneurysms. *IEEE Transactions on Medical Imaging*, 28(8):1141–1155, 2009.

[86] A. Klepaczko et al. Simulation of mr angiography imaging for validation of cerebral arteries segmentation algorithms. *Computer Methods and Programs in Biomedicine*, 137:293–309, 2016.

[87] X. Jiang, R. Zhang, and S. Nie. Image segmentation based on level set method. *Physics Procedia*, 33:840–845, 2012.

[88] L. Luo et al. Carotid artery segmentation using level set method with double adaptive threshold (datls) on tof-mra images. *Magnetic Resonance Imaging*, 63:123–130, 2019.

[89] Y. Zhao et al. A level set method for multiple sclerosis lesion segmentation. *Magnetic Resonance Imaging*, 49:94–100, 2018.

[90] X. Shi and C. Li. Anatomical knowledge based level set segmentation of cardiac ventricles from mri. *Magnetic Resonance Imaging*, 86:135–148, 2022.

[91] P. Pavone, M. Fioranelli, and D. A. Dowe. *CT Evaluation of Coronary Artery Disease*. Springer, 2009.

[92] G. M. Pelagi. Numerical modeling for the estimation of stress-ct maps of myocardial blood flow. Master's thesis, Politecnico di Milano, 12 2020.

[93] German Cancer Reasearch Division of Medical Image Computing. "Medical Imaging Interaction Toolkit", 2015. `http://www.mitk.org/wiki/MITK`.

[94] M. Fedele and A. Quarteroni. Polygonal surface processing and mesh generation tools for the numerical simulation of the cardiac function. *International Journal for Numerical Methods in Biomedical Engineering*, 37(4):e3435, 2021.

[95] A. F. Frangi et al. Multiscale vessel enhancement filtering. In *Medical Image Computing and Computer-Assisted Intervention — MICCAI'98*, pages 130–137. Springer Berlin Heidelberg, 1998.

[96] Kitware. "paraview", 2002. `https://www.paraview.org/`.

[97] L. Formaggia et al. Numerical treatment of defective boundary conditions for the Navier–Stokes equations. *SIAM Journal on Numerical Analysis*, 40(1):376–401, 2002.

[98] A. Veneziani and C. Vergara. Flow rate defective boundary conditions in haemodynamics simulations. *International Journal for Numerical Methods in Fluids*, 47:803–816, 2005.

[99] A. Quarteroni. *Numerical Models for Differential Problems.* Springer Cham, 2017.

[100] T.E. Tezduyar. Stabilized finite element formulations for incompressible flow computations. volume 28 of *Advances in Applied Mechanics*, pages 1–44. Elsevier, 1991.

[101] L. Tobiska and G. Lube. A modified streamline diffusion method for solving the stationary Navier-Stokes equation. *Numerische Matematik*, 59:13–29, 1991.

[102] D. Forti and L. Dedè. Semi-implicit bdf time discretization of the navier–stokes equations with vms-les modeling in a high performance computing framework. *Computers & Fluids*, 117:168–182, 2015.

[103] S. Deparis, G. Grandperrin, and A. Quarteroni. Parallel preconditioners for the unsteady navier–stokes equations and applications to hemodynamics simulations. *Computers & Fluids*, 92:253–273, 2014.

[104] P. C. Africa et al. lifex - heart module: a high-performance simulator for the cardiac function. Technical Report 04, MOX, 2022.

[105] D. Arndt et al. The deal.ii library, version 9.2. *Journal of Numerical Mathematics*, 28(3):131–146, 2020.

[106] E. Faggiano et al. Helical flows and asymmetry of blood jet in dilated ascending aorta with normally functioning bicuspid valve. *Biomechanics and Modeling in Mechanobiology*, 12:801–813, 2013.

[107] K. Perktold et al. Validated computation of physiologic flow in a realistic coronary artery branch. *Journal of Biomechanics*, 31(3):217–228, 1997.

[108] J. King and D. R. Lowery. Physiology, cardiac output, 2021. `https://www.ncbi.nlm.nih.gov/books/NBK470455/`.

[109] A. Deussen et al. Mechanisms of metabolic coronary flow regulation. *Journal of Molecular and Cellular Cardiology*, 52(4):794–801, 2012.

[110] I. T. Gabe et al. Measurement of instantaneous blood flow velocity and pressure in conscious man with a catheter-tip velocity probe. *Circulation*, 40(5):603–614, 1969.

[111] A. Quarteroni and A. Valli. *Domain Decomposition Methods for Partial Differential Equations*. Numerical Mathematics and Scie. Clarendon Press, 1999.

[112] C.Y. Wang and J.B. Bassingthwaighte. Area-filling distributive network model. *Mathematical and Computer Modelling*, 13(10):27–33, 1990.

[113] M.H. Tawhai, A.J. Pullan, and P.J Hunter. Generation of an anatomically based three-dimensional model of the conducting airways. *Annals of Biomedical Engineering*, 28(7):793–802, 2000.

[114] W. Schreiner et al. Optimized arterial trees supplying hollow organs. *Medical Engineering & Physics*, 28(5):416–429, 2006.

[115] C. Zhang et al. Chapter 12 - regulation of coronary microvascular resistance in health and disease. In *Microcirculation*, pages 521–549. Academic Press, second edition edition, 2008.

[116] H.K. Hammond. Exercise and the cardiovascular system. In *Reference Module in Biomedical Sciences*. Elsevier, 2014.

List of Figures

1.1 Representation of the human heart [1]. 3
1.2 Aortic pressure, ventricular pressure, atrial pressure and ventricular volume during the cardiac cycle [2]. 4
1.3 Coronary circulation. 6
1.4 Aortic pressure and CBF for LCA and RCA [12]. 7
1.5 Multi-compartment porous media modeling. 13
1.6 Patient-specific computational and clinical MBF maps from [70]. 16

2.1 Example of Thresholding segmentation technique. 21
2.2 Fast marching segmentation technique. 22
2.3 Colliding Fronts segmentation technique. 24
2.4 Schematic illustration of the Level set method. 25
2.5 Different views of a single slice cCTA. 28
2.6 Left ventricle reconstructed in [70]. 29
2.7 Epicardial coronary network reconstructed in [70]. 30
2.8 Level set segmentation process. 31
2.9 Extraction of the zero-level surface after Level set segmentation. 32
2.10 Aortic root structure after clipping via Paraview. 34
2.11 Definition of *EdgeLengthSmooth* on the aortic root surface. 34
2.12 Superficial meshes for the aortic root with different levels of refinement. . . 35
2.13 Array *DistanceToCenterlines*, defined on the reconstruction of the epicardial coronary artery tree. 35
2.14 Connection of the structures and superficial mesh on the connected structure. 36
2.15 Array *GlobalH*, defined on the connected structure. 37
2.16 Superficial meshes for the connected geometry with different levels of refinement. 39
2.17 Results of the mesh generation process considering four patients. 40

3.1 Reconstructed computational domain for aortic root and entire epicardial coronary arterial tree. 43

3.2 Cylindrical computational domain. 54
3.3 Comparison between numerical and assigned flow rate on the inlet boundary of the cylinder. 55
3.4 Numerical results in the cylindrical domain at t=1s. 56
3.5 Numerical results in the cylindrical domain at t=10s. 57
3.6 Patient-specific geometry of aortic root and epicardial coronary arteries where computational hemodynamics are simulated. 58
3.7 Temporal profiles used to prescribe boundary conditions. 60
3.8 Numerical hemodynamics results inside a patient-specific anatomical geometry. 61
3.9 Numerical pressure and velocity streamlines across the domain for different time instants. 63
3.10 Numerical pressure gradients for different time instants. 64
3.11 Flow rates in left and right coronary branches considering two scenarios. . 66

4.1 Schematic overview of the 3-compartment porous medium in a piece of myocardium. 70
4.2 Perfusion regions and surrogate intramural network for one patient. 79

5.1 MBF from stress-CTP 87
5.2 Representation of $\overline{\text{MBF}}_{\text{CTP}}(\mathbf{x})$ across the myocardium for patients P2, P3, and P4. [71] 88
5.3 P2 patient-specific computational domains for aortic root, epicardial coronaries and left ventricle. 92
5.4 Temporal profiles needed to assign boundary conditions in the perfusion model. 93
5.5 Comparison between implicit and explicit NS pressure and first Darcy compartment pressure for different time instants. 95
5.6 Relative error of the explicit strategy with respect to the implicit one. . . . 96
5.7 Number of iterations needed for the implicit algorithm in order to reach convergence. 97
5.8 Average-in-space pressures inside aortic root and each Darcy compartment together with the venous pressure considering 3 different scenarios. 98
5.9 Distribution of NS and first Darcy compartment pressure fields for different time-steps. 100
5.10 Comparison between computational MBF maps considering rest and stress cardiac output. 101

5.11 Computational and clinical MBF maps after stress *a priori* parameter adjustment. . . . 103
5.12 Relative error maps after stress *a priori* parameter adjustment. . . . 104
5.13 Computational and clinical MBF maps after patient-specific parameter optimization 106
5.14 Relative error maps after patient-specific parameter optimization. . . . 107

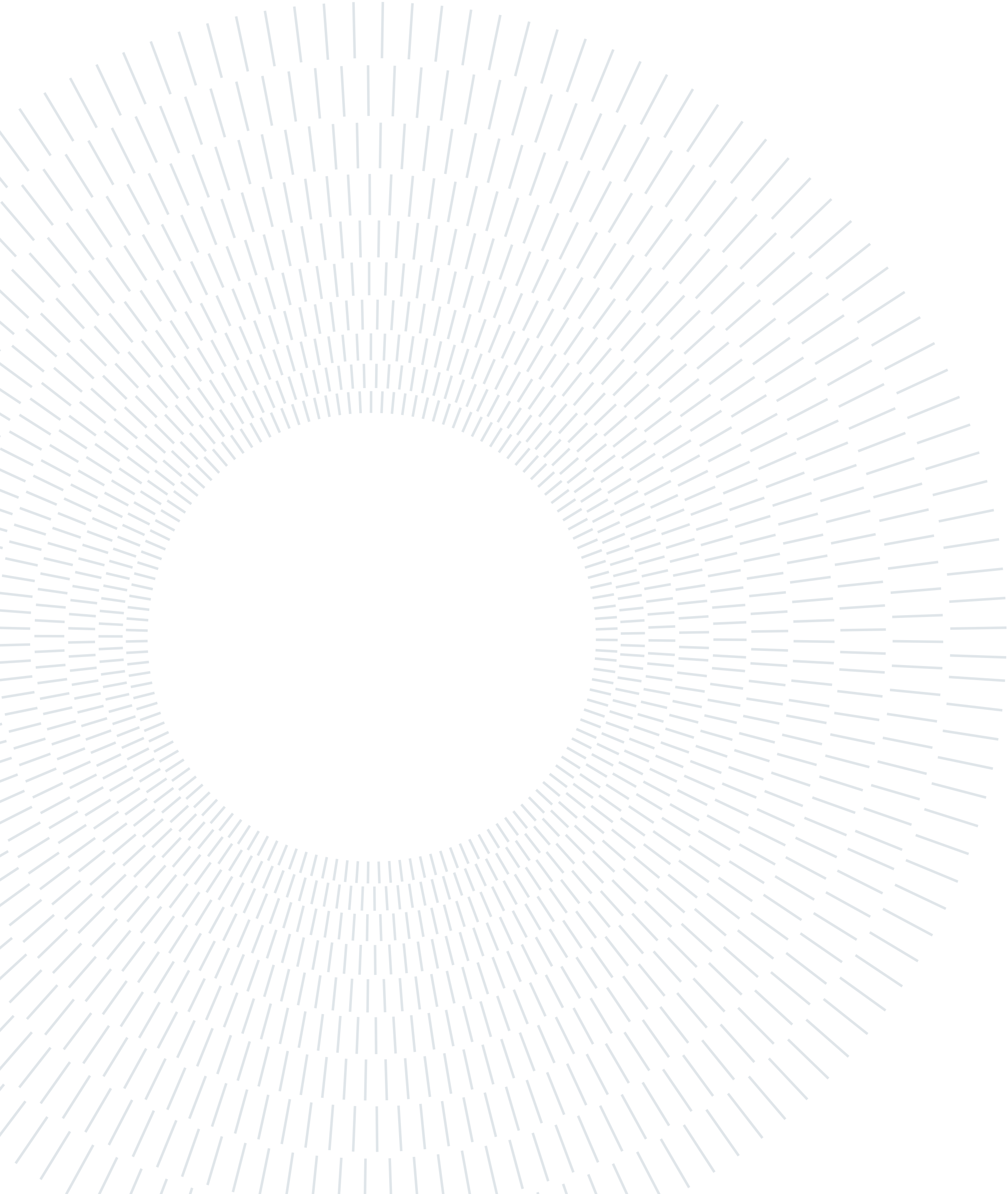

List of Tables

5.1 Values of $\mathrm{MBF}_{\mathrm{CTP}}^{\mathrm{avg}}$ and $\mathrm{CBF}_{\mathrm{MBF}}$ for all three patients considered in this study 88
5.2 Effects of pharmacological induced stress conditions on each patient. 89
5.3 Average MBF and relative error between computational and clinical MBF maps after *a priori* parameter adjustment. 105
5.4 Average MBF and relative error between computational and clinical MBF maps after patient-specific parameter optimization. 107

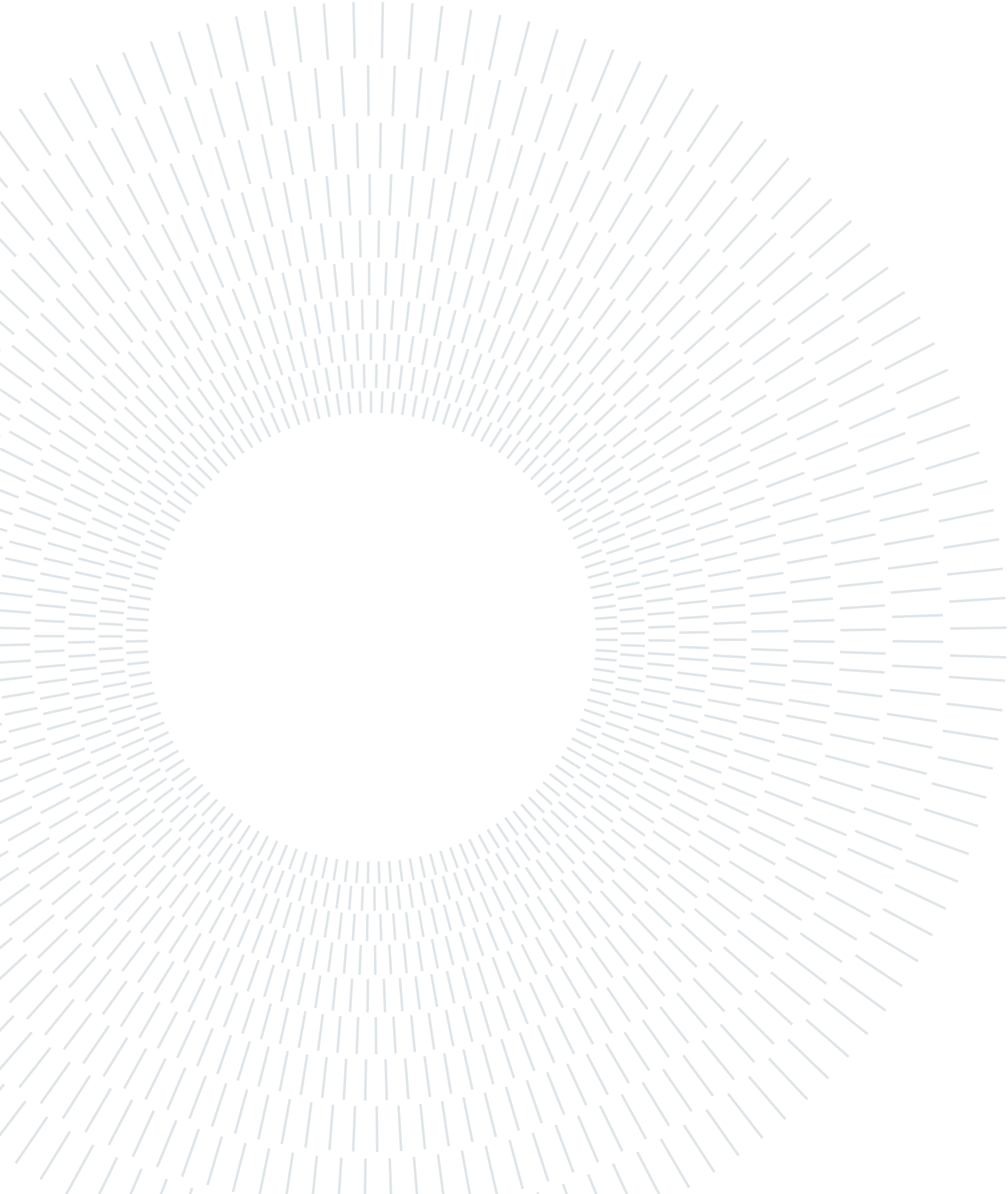

List of Abbreviations

CAD: Coronary artery disease

CBF: Coronary blood flow

cCTA: Coronary computed tomography angiography

CFD: Computational fluid dynamics.

CT: Computed tomography

HR: heart rate

LCA: Left coronary artery

MBF: Myocardial blood flow

$\mathbf{MBF_{avg}}$: Average-in-space myocardial blood flow

$\mathbf{MBF_{COMP}}$: Myocardial blood flow computed by the computational model

$\mathbf{MBF_{CTP}}$: Myocardial blood flow measured by stress myocardial computed tomography perfusion

NS: Navier-Stokes

RCA: Right coronary artery

stress-CTP: stress myocardial computed tomography perfusion

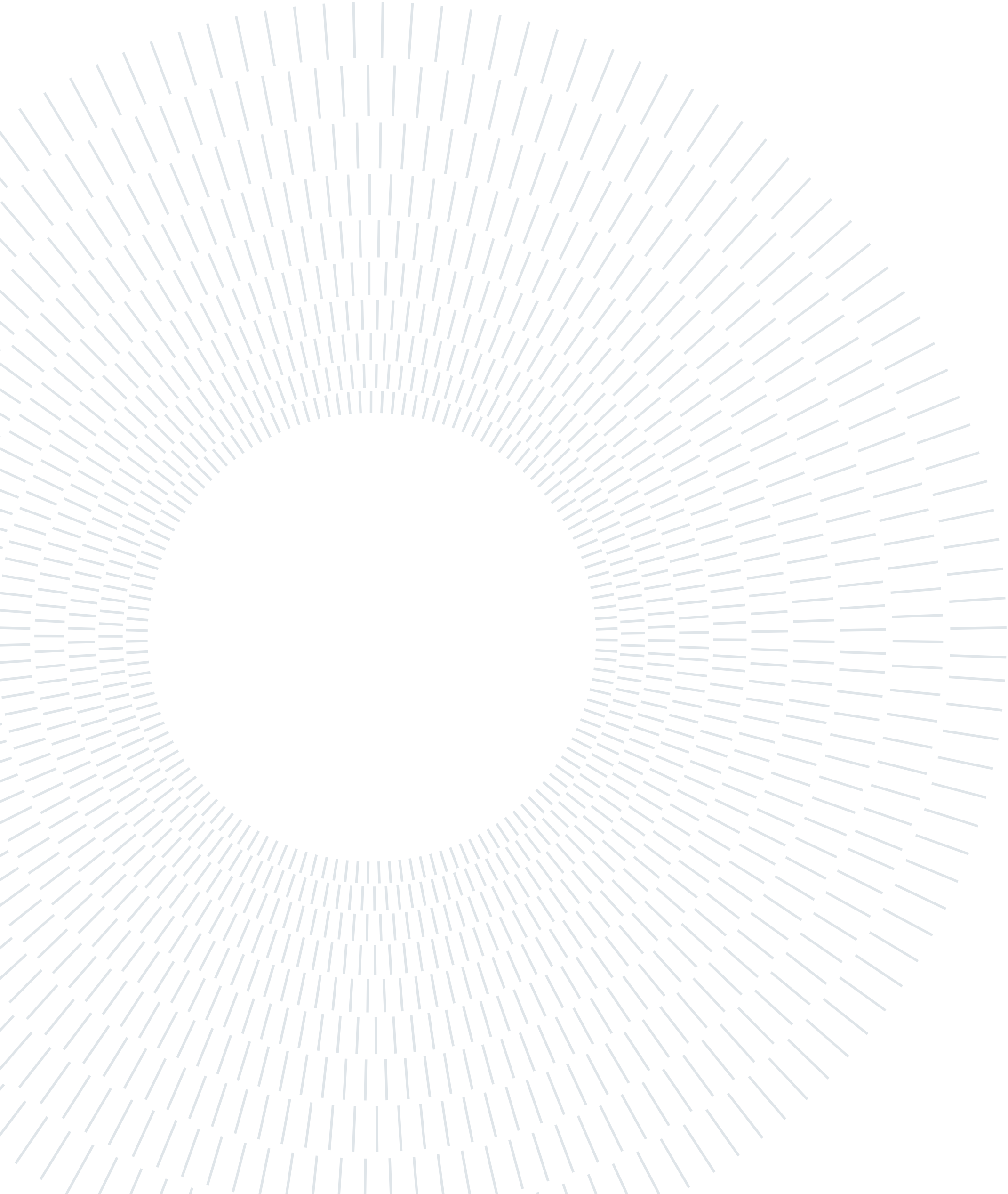

Ringraziamenti

Vorrei ringraziare alcune persone senza le quali questa tesi non sarebbe stata possibile.

Ringrazio chi ha collaborato con me a questo progetto, in particolare:
Christian Vergara per avermi supportato e sopportato nelle attività pratiche e soprattutto nella stesura della tesi.
Marco Fedele per gli innumerevoli consigli e il continuo supporto tecnico offertomi.
Giovanni Montino Pelagi e Pasquale Africa per essersi sempre resi disponibili quando ce n'è stato bisogno.

Ringrazio la mia famiglia stretta, mia mamma, mio papà e i miei fratelli, per essermi sempre stati vicino ed avermi aiutato a superare i momenti di nervosismo e perplessità. La mia famiglia allargata, nonni, zii e cugini, che ha sempre rappresentato per me un nido sicuro. Particolari menzioni vanno a mia nonna Annamaria per essere il centro di questa grande famiglia, ai miei zii Livia e Giorgio per avermi ospitato in casa loro e trattato come un figlio, a Lillo ed Ale per le serata passate al quarto piano e alla zia Stefi per averle rese possibili accogliendomi sempre.

Ringrazio i ragazzi di Non Ljubjana per essere stati la mia valvola di sfogo e avermi accompagnato in ogni avventura, Ciccio che, anche se ormai distante, sento sempre vicino a me e Simone che mi ha insegnato molto e riesce sempre a strapparmi un sorriso.

Vorrei dedicare questa tesi a mio nonno Roi, che ha sempre rappresentato una grande fonte di ispirazione e avrebbe molto apprezzato vedere un suo nipote diventare Ingegnere come lui. Grazie Nonno.